TRIBHUVAN UNIVERSITY

INSTITUTE OF ENGINEERING

PULCHOWK CAMPUS

**B-16-BAS-2018/2023**

**NUMERICAL STUDY OF HYPERSONIC FLUID-STRUCTURE INTERACTION ON A CANTILEVERED PLATE WITH SHOCK IMPINGEMENT**

by

Nishchal Poudel (075AER025)

Sambhav Sahani (075AER036)

Subarna Pudasaini (075AER043)

A PROJECT REPORT

SUBMITTED TO THE DEPARTMENT OF MECHANICAL AND AEROSPACE ENGINEERING IN PARTIAL FULFILLMENT OF THE REQUIREMENTS FOR THE DEGREE OF BACHELOR OF AEROSPACE ENGINEERING

DEPARTMENT OF MECHANICAL AND AEROSPACE ENGINEERING

LALITPUR, NEPAL

MARCH 2023

# COPYRIGHT

TRIBHUVAN UNIVERSITY
INSTITUTE OF ENGINEERING
PULCHOWK CAMPUS
DEPARTMENT OF MECHANICAL AND AEROSPACE ENGINEERING
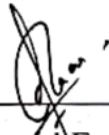
The undersigned certify that they have read, and recommended to the Institute of Engineering for acceptance, a project report entitled "NUMERICAL STUDY OF HYPERSONIC FLUID-STRUCTURE INTERACTION ON A CANTILEVERED PLATE WITH SHOCK IMPINGEMENT" submitted by Nishchal Poudel, Sambhav Sahani and Subarna Pudasaini in partial fulfillment of the requirements for the degree of Bachelor of Aerospace Engineering.
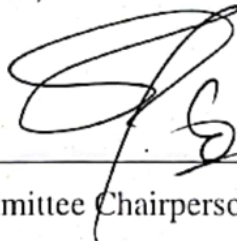
Supervisor, Sudip Bhattarai (Ph. D.)

Assistant Professor

Department of Mechanical and Aerospace Engineering

Supervisor, Kamal Darlami

Assistant Professor

Department of Mechanical and Aerospace Engineering

External Examiner, Bikalpa Bomjan Gurung

Consultant, Flight Operations Engineering

3Green, UAE

Committee Chairperson, Dr. Surya Prasad Adhikari

Head, Associate Professor

Department of Mechanical and Aerospace Engineering

Date: 17th March, 2023

iii

# ABSTRACT

Aeroelastic vibration of compliant wing panels and control surfaces is a major design concern in hypersonic vehicles. Impingement of shock waves of varying intensity also adds to the aeroelastic effect and vibration. UNSW Canberra's Hypersonic Multibody Aeroelastic eXperiment (HyMAX) serves as a benchmark test case for Fluid-Structure Interaction (FSI) in hypersonic flows. This study carries out a numerical study of the HyMAX experimental setup at a flow deflection angle of $10°$ using both low-fidelity modeling (LFM) and high-fidelity modeling (HFM) approaches. In the LFM approach, an analytical SE-based Piston Theory and a CFD-Enriched Piston Theory were used. And, a two-way partitioned approach using OpenFOAM, Calculix, and PreCICE was used for the HFM. The cantilevered plate deformed around the first mode. Peak pressure variation and the trailing edge displacement history showed similar nature indicating that the FSI phenomenon was dominated mostly by the local pressure changes over the plate. The peak pressure approximations results of both the LFM and the HFM highlighted the quasi-steady nature of the problem. The peak pressure value predicted by the viscous CFD is around 4% (300 Pa) more when compared to the inviscid CFD result and the maximum trailing edge deflection (3.96 mm) predicted by the viscous FSI is about 4 % higher than the value predicted by the inviscid FSI (3.80 mm), which can be attributed to Shock-Wave Boundary Layer Interaction (SWBLI) phenomenon, leading edge shock wave, and other viscous effects. The Shock-Expansion based Piston Theory (PT) predicted the maximum trailing edge displacement with about 8 % error in HyFoil_HH (with no shock impingements) but with about 14 % error in HyMAx (with shock impingement). In the case of the shock-impingement, CFD Enriched PT was found to make a better prediction with only about an 6.82% error with respect to the viscous FSI result. The computation time required for a flow duration of 200 ms for CFD Enriched PT was very short only about 4 hours as compared to about 24 hours for the inviscid FSI and 480 hours for viscous FSI. Hence, CFD Enriched PT can be an effective tool for preliminary aeroelastic analysis.

***Keywords:*** *hypersonic, fluid-structure interaction, aeroelasticity, shock impingement, shock-wave boundary layer interaction*

# ACKNOWLEDGEMENT

# TABLE OF CONTENTS

# LIST OF FIGURES

# LIST OF TABLES

# ABBREVIATIONS

| | |
|---|---|
| 2D | Two Dimensional |
| 3D | Three Dimensional |
| AFRL | Air Force Research Laboratory |
| AOA | Angle of Attack |
| ARMA | Auto Regressive Moving Average |
| CFD | Computational Fluid Dynamics |
| CSD | Computational Structural Dynamics |
| CTD | Computational Thermal Dynamics |
| DARPA | Defence Advanced Research Projects Administration |
| DSTO | Defence Science And Technology Organization |
| FEA | Finite Element Analysis |
| FEM | Finite Element Method |
| FFT | Fast Fourier Transform |
| FSI | Fluid-Structure Interaction |
| FTSI | Fluid-Thermal-Structural Interaction |
| FVM | Finite Volume Method |
| GCI | Grid Convergence Index |
| HFM | High Fidelity Method |
| HyMAX | Hypersonic Multibody Aeroelastic eXperiment |
| LES | Large Eddy Simulation |
| LFM | Low Fidelity Method |
| NASP | National Aerospace Plane |
| NI | Newtonian Impact |
| NS | Navier-Stokes |
| OpenFOAM | Open-source Field Operation and Manipulation |
| PT | Piston Theory |
| PreCICE | Precise Code Interaction Coupling Environment |
| RANS | Reynolds-Averaged Navier Stokes |
| RLV | Reusable Launch Vehicle |
| ROMs | Reduced Order Models |
| SE | Shock-Expansion |
| SWBLI | Shock-Wave Boundary Layer Interaction |
| UNSW | University of New South Wales |

# SYMBOLS

| | |
|---|---|
| $p$ | Pressure |
| $\gamma$ | Gas Constant |
| $M$ | Mach Number |
| $\theta$ | Local Deflection Angle |
| $\rho$ | Density of Air |
| $e$ | Specific Energy |
| $u$ | Velocity |
| $\tau$ | Shear Stress |
| $T$ | Static Temperature |
| $k$ | Conductivity |
| $\mu$ | Viscosity Coefficient |
| $C_p$ | Specific Heat Capacity at Constant Pressure |
| $C_v$ | Specific Heat Capacity at Constant Volume |
| $R$ | Specific Gas Constant |
| $Pr$ | Prandtl Number |
| $w$ | Plate Deflection |
| $D$ | Flexural Rigidity |
| $E$ | Youngs's Modulus |
| $I$ | Moment of Inertia |
| $\mu_m$ | Mass Per Unit Length |
| $h$ | Thickness of Plate |
| $x$ | Position along the x-axis (length of the plate) |
| $L$ | Length of the Plate |
| $l$ | Length of an Element |
| $\delta$ | Vertical Deflection |
| $\sigma$ | Stress |
| $B$ | Body Force |
| $M$ | Elemental Mass Matrix |
| $K$ | Elemental Stiffness Matrix |
| $\bar{D}$ | Elemental Damping Matrix |
| $\alpha, \beta$ | Rayleigh Damping Coefficients |
| $\zeta_1, \zeta_2$ | Damping Ratios |
| $\lambda$ | Diffusivity Parameter |

## Subscripts

| | |
|---|---|
| $\infty$ | Freestream |
| 1 | After Incident Shock Wave |
| 2 | After Reflected Shock Wave |
| $loc$ | Local |
| $pk$ | Peak |

# CHAPTER ONE: INTRODUCTION

## 1.1   Background

Fluid-Structure Interaction (FSI) is a class of problems describing the coupling of the governing laws of fluid and structural dynamics. The flow behavior is determined by the structure's shape and motion, and the structure's motion and deformation are determined by the fluid mechanics forces acting on it [1].

FSI plays an essential role in engineering applications, influencing the decisions that go into the design of systems of current relevance. As a result, fully predictive FSI methods that aid in the resolution of these challenges are in high demand in industry, research laboratories, medical areas, space exploration, and a variety of other settings. Some examples include fluttering of wings, falling of a leaf, blood flow and arterial dynamics, parachute dynamics, deflection in wind-turbine blades, shock impingement in hypersonic vehicles, etc [1].

Low-weight criterion is an important design consideration in hypersonic vehicles and hence FSI occurs in the compliant wing panels and control surfaces used. Furthermore, shock waves of varying intensity are formed and get impinged on different locations like the fuselage, the cowl, and within the scramjet flowpath's intake during maneuvers or changes in flight conditions [2].
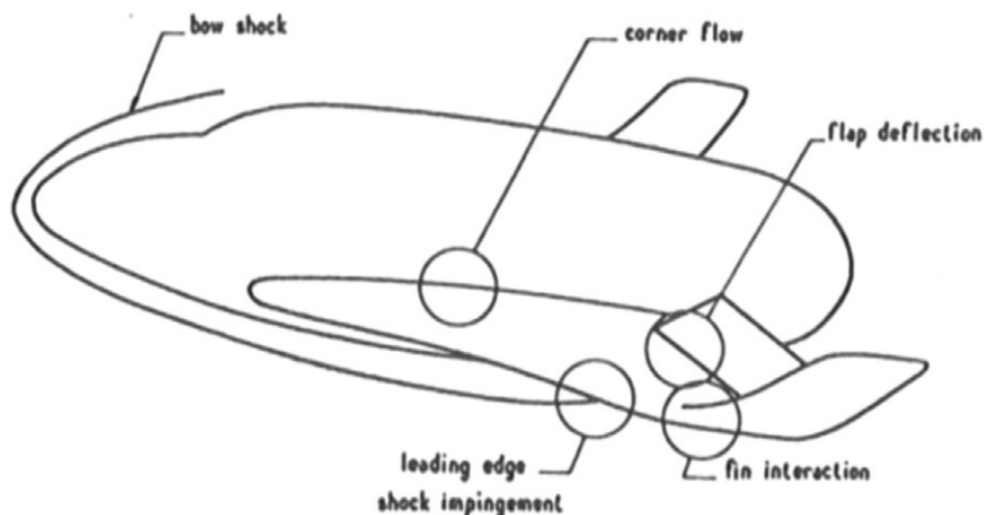


Figure 1.1: Example of Shock Impingement on Wing
[2]

The shock waves may also get affected by the aero-elasticity effect in the compliant skin and wing panels. This may result in Shock-Wave Boundary Layer Interaction (SWBLI). In case of high thermal loads, the panels will exhibit aero-thermo-elastic behavior which is an even more complex phenomenon involving fluid-structure interaction [3].

Thus, the study of FSI is essential in hypersonic vehicle design or any other hypersonic flow applications.

## 1.2   Problem Statement

Analytical solutions to the FSI problems are almost impossible to obtain and laboratory tests are limited in scope. Thus, numerical simulations are required to examine the underlying physics involved in the complicated interaction between fluids and solids. But, high-fidelity numerical simulations may get computationally very expensive and low-fidelity simulations may not provide the required accuracy.

Therefore, computational methods, which are robust, efficient, and accurate, need to be developed.

The University of New South Wales (UNSW) Canberra's Hypersonic Multibody Aeroelastic eXperiment (HyMAX) serves as a benchmark test case for FSI in hypersonic flow (AePW3 — High Speed Working Group). Researchers are required to simulate this flow and compare the findings with experimental measurements to validate the method.

## 1.3 Objectives

### 1.3.1 Main Objective

The main objective of this project is to carry out a numerical study of hypersonic fluid-structure interaction on a cantilevered plate with shock impingement.

### 1.3.2 Specific Objectives

- To model the problem (HyMAX) using high-fidelity and low-fidelity methods.

- To investigate the phenomenon of SWBLI due to impinging shock waves in hypersonic flows and its aeroelastic effects.

- To evaluate the performance of low-fidelity models by comparing the results with that of high-fidelity models.

## 1.4 Application

Works similar to this can be used as a supplement to the experiments for the following kinds of applications:

- To predict control authority of flaps in hypersonic vehicles.

- To predict time-dependent loads on hypersonic vehicle surfaces and hence select appropriate materials to be used.

- To study the effect of aeroelasticity on the performance of hypersonic intake ramps.

## 1.5  Features

The major features of this work are:

- Comparison of various low-fidelity and high-fidelity modeling approaches.

- Two-way hypersonic FSI with shock impingement.

- Largely based on open-source software.

## 1.6  Feasibility Analysis

### 1.6.1  Economic Feasibilty

From the budget analysis, it has been found that this kind of numerical study can cost about Rs. 54,000, an extensive amount of which is for renting computational resources. However, if a one-time investment is done in buying a good workstation computer, many studies of this kind can be carried out at a very reasonable cost.

### 1.6.2  Technical Feasibility

With the work being completely numerical, sound technical knowledge regarding the software aspects and some knowledge about the hardware aspects (for setting up the computers) is required.

### 1.6.3  Operational Feasibility

Given that there is a continuous supply of power, a good internet connection, and a well-managed computation room, the operation would not be a problem.

## 1.7   System Requirements

### 1.7.1   Software Requirements

The following software packages/programming languages were used for the completion of this work:

- OpenFOAM: Used for Computational Fluid Dynamics (CFD).

- CalculiX: Used for Computational Structural Dynamics (CSD).

- PreCICE: Used for coupling CFD and CSD.

- ParaView: Used for post-processing.

- PrePoMAX: Used for solid mesh generation for Calculix.

- FreeCAD: Used for solid model generation for Calculix.

- Matlab: Used for low-fidelity model program development.

- Python: Used for post-processing.

- Microsoft Excel: Used for data handling.

### 1.7.2   Hardware Requirements

A computer with the following specifications was used:

- 16 cores CPU

- 32 GB RAM

- 128 GB SSD

- 1 TB Harddisk

# CHAPTER TWO: LITERATURE REVIEW

## 2.1 Literature Review

### 2.1.1 Hypersonic FSI

Hypersonic FSI is a relatively recent field of research with a significant amount of literature starting from the late 1900s and early 2000s. The need of developing reusable hypersonic vehicles has motivated the resurgence of interest in this area [4]. Hypersonic vehicles and intakes are designed to operate in the limited range of Angle of Attack (AOA) and Mach number. Aeroelastic and aerothermoelastic effects in hypersonic vehicles induce off-design conditions during the flight which can cause loss of performance and even loss of the vehicle in some extreme cases [5]. Thus, FSI and FTSI analysis are essential in the vehicle design process to study and analyze these off-design characteristics and their effects.

Due to the strong non-linearity and multidisciplinary nature of FSI problems, comprehensive study of such problems has remained a challenge [6]. In [7], the author emphasized that using the conventional approach of testing using aeroelastically scaled wind tunnel models, as in subsonic and supersonic flows, is not feasible in the hypersonic regime and thus increasing the importance of aeroelastic simulations. As the analytical solutions are almost impossible to obtain and laboratory experiments are not always feasible, numerical simulation is a must for the study of the complex interaction between fluids and solids [8].

### 2.1.2 Shock-Wave Boundary Layer Interaction

Shock-Wave Boundary Layer Interaction has been the focus of numerous studies for several decades as understanding SWBLI and its effects is crucial for hypersonic vehicle design. One such effect is the localized aerodynamic heating which increases with increasing Mach number that can be extremely severe [9]: one such example was seen on one of the final flights of the X-15 hypersonic vehicle in the 1960s[10]. Another serious problem in high-speed flights is the intake unstart. This problem was encountered in the Boeing X-51 scramjet during a powered flight test in 2011, also resulting in the loss of the vehicle[11]. SWBLI, being one of the contributing factors for engine un-

start, must be studied and analyzed during supersonic and hypersonic intake and engine design [12].

External shock impingement into the body and flow through a compression ramp are the two most common cases used to study SWBLI in literature. [13] experimentally studied hypersonic shock-wave boundary layer interaction in hypersonic flow at freestream Mach numbers from 6.5 to 13, with Reynolds number ranging from $1\times10^7$ to $1\times10^8$, at the wall to freestream stagnation temperature from 0.1 to 0.4. The separated region was induced in two ways: through external oblique shockwave impingement and through compression surface. The separation region length was found to increase with increasing Reynolds number and wall-to-freestream stagnation temperature and decreasing freestream Mach number.

In [14], the author investigated the SWBLI phenomenon on a rigid flat plate experimentally. When the oblique shock wave impinged on the boundary layer, the boundary layer separated upstream of the impingement location. However, the separated boundary layer is reattached again to the surface downstream of the flow. Due to the streamlined curvature at the separation and reattachment point, instability of the boundary layer occurred because of the formation of Görtler vortices, called the Görtler boundary layer instability. This instability caused the transition of the boundary layer. The transition took place within the separation region and thus boundary layer can be considered turbulent close to the reattachment point. The amplitude of the Görtler-like vortices was influenced by the motion of the plate. The downward plate deflection resulted in a larger streamlined radius at the reattachment point reducing the Gortler-like vortices amplitude. However, the spanwise wavelength appeared to be unaffected.

### 2.1.3   Low Fidelity Modeling

Low Fidelity Method (LFM), High Fidelity Method (HFM), and Reduced Order Models (ROMs) are the modeling approaches commonly used in the literature to model individual domains followed by coupling mechanisms [15].

Due to the impracticality of wind-tunnel tests of aero-elastically and aero-thermo-elastically scaled models and high computational complexity and cost of time-accurate unsteady CFD analysis, various approximate unsteady aerodynamic theories which assume inviscid flow and neglect real gas effects like Piston Theory (PT), Van Dyke's second-order theory, Newtonian Impact (NI) theory, and unsteady Shock-Expansion (SE) theory are

implemented for preliminary design and sensitivity analysis of hypersonic configurations. Moreover, the quasi-steady nature of hypersonic flowfields (wake effects can be neglected, as the disturbances cannot propagate upstream) has motivated the use of various hybrid approaches which combine the steady-state CFD analysis with the unsteady aerodynamic models like the piston theory [16].

### 2.1.3.1 Unsteady Aerodynamics Modeling

In [16], the authors examined the performance of various classical hypersonic unsteady aerodynamic theories: PT, Van Dyke's second-order theory, NI theory, and unsteady SE theory, and several other alternatives: two different viscous approximations based on effective shapes and a hybrid steady-state CFD-piston theory approach, for the aeroelastic analysis in a thin double-wedge airfoil in hypersonic flow with freestream Mach number between 5.0 and 35 by comparing the flutter boundaries with the unsteady CFD solutions. The results indicated that the theories yielded good predictions with the exception of first-order PT and NI theory. Van Dyke's second-order theory, second-order PT, unsteady SE theory, and a hybrid steady-state Navier–Stokes/piston theory method produced flutter boundaries within an average difference of 6% and a maximum difference of 12%, relative to unsteady Navier–Stokes predictions for hypersonic similarity values up to 1.0. The authors concluded that the thickness effects(a second-order effect) strongly influence the dynamic aeroelastic stability, as the local piston theory showed a good correlation in contrast to the high error of the first-order piston theory; the impact of viscosity on the flutter boundaries of a thin section is negligible, as a good correlation was seen between the predictions of the inviscid theories and the unsteady Navier-Stokes solutions; the non-linearities in hypersonic flow are primarily due to steady-state effects, as the hybrid steady-state CFD-piston theory approach demonstrated a good accuracy.

In [17], the peak pressure evolution was predicted with the first-order and the third-order CFD-enriched piston theory and compared against the results of the CFD and the experiment (involving a shock impinging on a compliant cantilevered plate at Mach 5.8). The results given by the first-order and the third-order formulation were found to be almost the same and predicted a trend similar to the CFD and the experiment. The maximum difference between the piston theory and the CFD and the experiment was approximately 10% and 15% respectively. Moreover, the authors concluded that since the peak pressure generally depends on the plate deformation history and is not only the function of instantaneous deformations, the problem cannot be considered completely quasi-steady. However, the transient effects are minor.

### 2.1.3.2  Structure Modeling

In recent works [14, 17] involving the impingement of a shock on a cantilevered plate, the plate was modelled as a cantilevered beam using the Euler-Bernoulli beam model by assuming sections always normal to the beam axis (with the thickness-to-length ratio on the order of $10^{-3}$). In [14], the mass matrix M and the stiffness matrix K were modified with the Timoshenko shear stress correction and Rayleigh (two-mode) damping model was used.

## 2.1.4  High Fidelity Modeling

High-fidelity modelling of hypersonic FSI poses a significant challenge not just because of computational cost. First of all, the FSI coupling should fulfil the requirement of accuracy and stability as the solution marches in time. Fluid governing equations are in the Eulerian frame of reference while structure governing equations are in the Lagrangian frame of reference which creates the complexity in accommodating them together. Techniques like the ALE approach [18], the corotational approach [19], and the space-time formulation [20] have been developed and used to tackle this complexity.

FSI simulations are found to be done in two different ways: monolithic and partitioned approaches. The governing equations of both fluid and structure are combined using a consistent scheme and solved with marching in time in the monolithic FSI coupling [21]. On contrary, two separate Computational Fluid Dynamics (CFD) and Computational Structural Dynamics (CSD) solvers are used to solve respective fluid and structure parts in the partitioned FSI coupling [22]. In [21], the author compared partitioned and monolithic approaches for numerical simulation of FSI in terms of computational cost, stability, and accuracy using a One Dimensional Model Problem of a piston interacting with a fluid. They found with a higher computational cost per unit time step, the monolithic approach provided better stability and accuracy. However, it is difficult to incorporate state-of-the-art improvements in the field of CFD and CSD in the monolithic approach. The partitioned approach has the advantage of modularity and thus can incorporate state-of-the-art improvements making it more popular in use [15].

In [23], it is mentioned that generally two main approaches are employed in Fluid-Thermal-Structural Interaction (FTSI) simulations: the strong (or tight) coupling technique, which solves the resulting coupled non-linear equations from the CFD, CSD, Computational Thermal Dynamics (CTD), along with the interface conditions in a sin-

gle step, and the loose coupling technique, which is an iterative approach of solving CFD, CTD, and CSD in the order until convergence. Depending on the treatment of mesh, FSI solution procedures can be of two types: confirming mesh approach and non-confirming mesh approach. The recent development in FSI methods is the use of Immersed Methods [8]. The original IBM required incompressible conditions [24], however, the introduction of penalty or sharp-interface IBMs solves this problem [25].

### 2.1.5 Previous Works

As mentioned earlier, significant research in hypersonic FSI can be found starting from the late 1900s and early 2000s. However, the potential problems of hypersonic aeroelasticity were already well identified during the 1950s and 1960s [26]. Early research in this period was focused more on rotary-wing aeroelasticity, the limit cycle dynamics, and flutter control of rotorcraft blades in the transonic regime [27]. The modern era of hypersonic flight research is considered to be started in the mid-1980s with the National Aerospace Plane (NASP) program, aimed at developing a single-stage-to-orbit reusable launch vehicle (RLV) that used conventional runways for takeoff [28]. Since then programs like the NASA Hyper-X experimental vehicle program [29], the University of Queensland HyShot program [30], the NASA Fundamental Aeronautics Hypersonics Project [31], the joint U.S. Defense Advanced Research Projects Administration (DARPA)/USAF Force Application and Launch from Continental United States (FALCON) program [32], the X-51 Single Engine Demonstrator [33], the joint USAF Research Laboratory (AFRL)/Australian Defence Science and Technology Organisation Hypersonic International Flight Research Experimentation project [34] continued the research based on the same theme realizing air-breathing propulsion is the way to move forward. These programs largely motivated the research in hypersonic aeroelasticity and aerothermoelasticity.

Flight vehicle designs from the above-mentioned flight research programs have been used for numerical studies. In [35], the authors did a set of aeroelastic stability analyses of the X-43 plane and concluded that discretizing both the structure and the fluids using a common finite element procedure ensures an accurate interaction between the two. The CPU time of about 225 hours was required on a 1 GHz PC for a flutter solution at Mach 1 Using Auto Regressive Moving Average (ARMA) model. Similar follow-up study was done later by [36] in the same X-43 vehicle using four methodologies: the direct time marching, the ARMA method, and two hybrid CFD-piston simulations and compared. Likewise, [7] did an aeroelastic simulation of a generic hypersonic

lifting-body vehicle by coupling high-fidelity CFD and FEM solvers. Both Euler and Navier Stokes solution methods were used in CFD. The difference between inviscid and viscous results in the 3D generic hypersonic vehicle was found to be significantly less compared to the differences in double wedge airfoil, which was attributed to the three-dimensional relief effect.

Recent literature is mainly focused on analytical, experimental, and computational predictions of FSI on the scramjet inlet as well as wings and control surfaces. All three approaches: experimental, analytical, and computational are being used and the focus is to get agreement between them. [37] suggests that the relatively high cost of flight tests necessitates the careful design, testing, and simulation of the experiments before flight. Secondary or tertiary experiments can be adapted from fundamental unit cases tested on the ground and will provide validation and scaling comparisons. Approximate methods like piston theory and shock expansion theories have been used for the preliminary design of the experiments [17, 38, 39].

In [38], the authors experimentally investigated the effect of FSI on the control authority of a trailing-edge flap through the hypersonic ground test of the rigid flap and compliant flap (of 1 mm thickness) at discrete angles of inclination and made a comparison with analytical and numerical predictions. In [17], the authors modeled the intake as a 2D cantilevered bronze plate and used Reynolds-Averaged Navier–Stokes (RANS) simulation results to enrich the low-fidelity model of 2-way aeroelastic interaction. Approximately 8% loss of pressure recovery occurred due to deformation from pressure loading while an additional 4% was from deformation induced by thermal degradation of the material. Also, the authors stated that using a laminar or a RANS solver is more advantageous than using the Large Eddy Simulation (LES) due to the high computational requirements of FSI simulations. However, there is a trade-off of accuracy and computation time.

High-fidelity numerical simulations have become much more common and accessible now with advancements in the computational field, however, experiments are limited to validate the results. Efforts have been made at UNSW to produce fundamental FSI experiments using a shock generator and an oscillating plate [14, 17, 40, 41]. Fundamental hypersonic FSI experiments like HyMAX [42] and HyFoil [39] are essential to further understand the underlying physics of FSI and to enhance the fidelity of the numerical simulation.

## 2.2 Research Gap

There is a research gap on how to reach an agreement between test and analysis in hypersonic FSI problems. Research is required on what needs to be measured in future experiments to get better agreement between test and analysis as well as how the numerical analysis should be carried out to get good agreement with experimental results. Our project focuses on the latter research gap.

# CHAPTER THREE: THEORY

## 3.1   Hypersonic Flows

As a rule of thumb, a flow is considered to be hypersonic when the Mach number of the flow is greater than 5. However, a hypersonic flow can be best defined as the flow regime where the flow phenomena like thin shock layer, entropy layer or vorticity interaction, viscous interaction, and high-temperature effects become more important as the Mach number is increased [9].

## 3.2   Shock-Wave Boundary Layer Interaction (SWBLI)

Since both the shock wave and the boundary layer are found in every supersonic flow, their interaction occurs frequently and is called the Shock-Wave Boundary Layer Interaction (SWBLI). The SWBLI has a major effect on the pressure, shear stress, and heat transfer distributions along the wall. In hypersonic speeds, the local heat transfer rate at the reattachment point can peak to an order of magnitude larger than at neighboring locations.

When an incident shock wave impinges on a boundary layer, a severe adverse pressure gradient is imposed on the boundary layer. This causes the boundary layer to separate. The separation takes place ahead of the theoretical inviscid impingement point of the incident shock wave because the high pressure behind the shock feeds upstream through the subsonic portion of the boundary layer. The separated boundary layer deflects the external flow into itself, thus inducing a second shock wave, called an induced separation shock wave. The separated boundary layer subsequently turns back toward the plate, reattaching to the surface at some downstream location. Hence, a third shock wave is formed as the flow is deflecting onto itself, called the reattachment shock. Between the separation and reattachment shocks, where the boundary layer is turning back toward the surface, the flow is turned away from itself, generating expansion waves. The separation and the reattachment shocks merge further away from the plate to form the conventional reflected shock wave that is expected in an inviscid flow. [43]
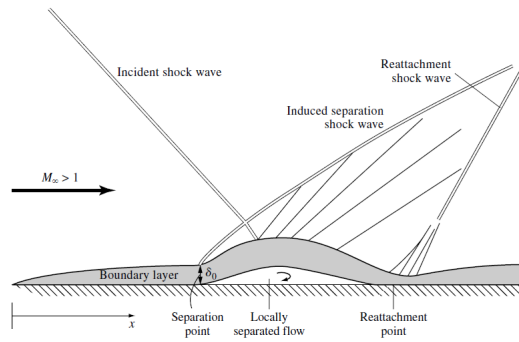
Figure 3.1: Schematic of SWBLI
[43]

The effects of SWBLI on pressure distribution and shear stress for a Mach 3 turbulent flow over a plate ($x_0$, the theoretical inviscid flow impingement point for the incident shock wave) are shown in the graphs below:
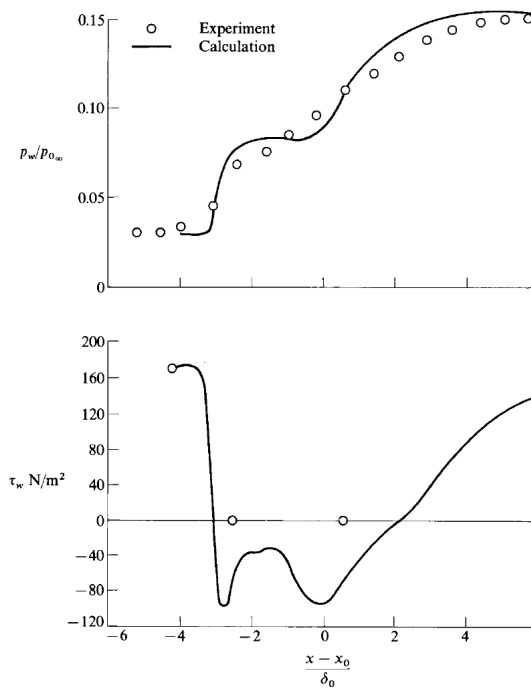


Figure 3.2: Effects of SWBLI on Pressure Distribution and Shear Stress (Turbulent Flow)

[43]

## 3.3   Shock-Expansion Theory

In the Shock-Expansion theory, the inviscid flow properties (Mach number and pressure) on a surface are obtained using the theories of the shock wave and the expansion

wave [43].

### 3.3.1 Isentropic Flow Relations

The isentropic flow relations used in this work are enlisted below:

$$\frac{T_o}{T} = \left(1 + \frac{\gamma - 1}{2} M^2\right) \tag{3.1}$$

$$\frac{p_o}{p} = \left(1 + \frac{\gamma - 1}{2} M^2\right)^{\frac{\gamma}{\gamma - 1}} \tag{3.2}$$

### 3.3.2 Oblique Shock Wave Relations

The oblique shock relations (Reference: Figure 3.3) used in this work are enlisted below:
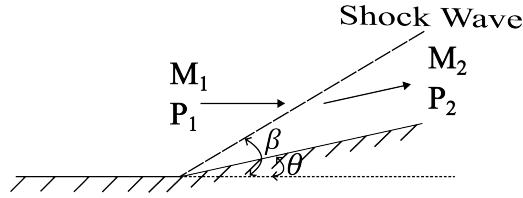


Figure 3.3: Oblique Shock Wave

$$\tan \theta = 2 \cot \beta \frac{M_1^2 \sin^2 \beta - 1}{M_1^2 (\gamma + \cos 2\beta) + 2} \tag{3.3}$$

$$M_{n,1} = M_1 \sin \beta \tag{3.4}$$

$$M_{n,2}^2 = \frac{1 + [(\gamma - 1)/2] M_{n,1}^2}{\gamma M_{n,1}^2 - (\gamma - 1)/2} \tag{3.5}$$

$$M_2 = \frac{M_{n,2}}{\sin(\beta - \theta)} \tag{3.6}$$

$$\frac{p_2}{p_1} = 1 + \frac{2\gamma}{\gamma + 1} (M_{n,1}^2 - 1) \tag{3.7}$$

### 3.3.3 Expansion Wave Relations

The expansion wave relations (Reference: Figure 3.4) used in this work are enlisted below:
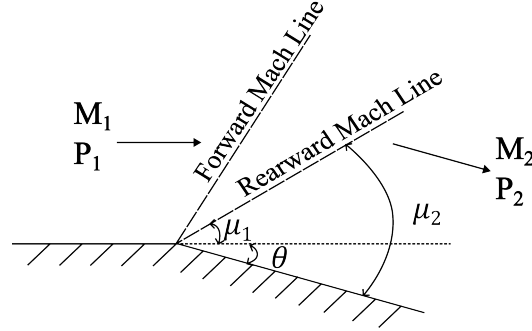


Figure 3.4: Expansion Wave

$$v(M) = \sqrt{\frac{\gamma + 1}{\gamma - 1}} tan^{-1} \sqrt{\frac{\gamma - 1}{\gamma + 1}(M^2 - 1)} - tan^{-1}\sqrt{M^2 - 1} \qquad (3.8)$$

$$\theta = v(M_2) - v(M_1) \qquad (3.9)$$

$$p_{O1} = p_{O2} \qquad (3.10)$$

## 3.4 Piston Theory

The piston theory is a method used for calculating the aerodynamic loads on a body by relating the local pressure generated by the body's motion to the local normal component of fluid velocity such that the relation between the quantities is similar to that at the face of a piston moving in a one-dimensional channel. It is generally applied for large flight Mach numbers or high reduced frequencies of unsteady motion whenever the surface is nearly plane and the surface's inclination to the direction of the free stream is not too sharp [44]. It has been used for wide-ranging applications, like the modeling of hypersonic vehicle dynamics [45], supersonic flutter analysis [46], supersonic/hypersonic aircraft optimization [47].

It was first used by Lighthill in [48]. The author noted that a plane slab of fluid initially perpendicular to the flow remains perpendicular in its own plane under the laws of 1D unsteady motion because the disturbances perpendicular to the flow are large compared to the disturbances parallel to the flow (since at high Mach numbers the shock and

16

expansion wave angles are very small and the velocity components parallel to the shock and expansion waves remain unchanged). Since then various extensions and corrections have been made to the classical piston theory [46, 49, 50, 51].

### 3.4.1 Classical Piston Theory

The local pressure is approximated using freestream flow quantities (pressure and Mach number).

Second Order:
$$p(x,t) = p_\infty \left(1 + \frac{\gamma - 1}{2} M_\infty \theta(t)\right)^{\frac{2\gamma}{\gamma-1}} \tag{3.11}$$

Third Order:
$$p(x,t) = p_\infty \left(1 + \gamma M_\infty \theta(t) + \gamma \frac{\gamma - 1}{4} (M_\infty \theta(t))^2 + \gamma \frac{\gamma - 1}{4} (M_\infty \theta(t))^3\right) \tag{3.12}$$

### 3.4.2 Local Piston Theory

When the flow is three-dimensional and/or Mach number and surface inclinations are high, the local pressure is approximated using the local flow quantities as:

Second Order:
$$p(x,t) = p_{loc} \left(1 + \frac{\gamma - 1}{2} M_{loc} \theta(t)\right)^{\frac{2\gamma}{\gamma-1}} \tag{3.13}$$

Third Order:
$$p(x,t) = p_{loc} \left(1 + \gamma M_{loc} \theta(t) + \gamma \frac{\gamma - 1}{4} (M_{loc} \theta(t))^2 + \gamma \frac{\gamma - 1}{4} (M_{loc} \theta(t))^3\right) \tag{3.14}$$

### 3.4.3 CFD-Enriched Piston Theory

The local flow quantities to be used in the local piston theory formulation can be extracted from the steady-state CFD results to improve the approximations. This approach is called CFD-Enriched Piston Theory.

## 3.5 Governing Equations

### 3.5.1 Fluid

The Navier-Stokes (NS) equations (in the index form) are:

$$\frac{\partial \rho}{\partial t} + \frac{\partial \rho u_i}{\partial x_i} = 0 \tag{3.15}$$

$$\frac{D\rho u_i}{Dt} = -\frac{\partial p}{\partial x_i} + \frac{\partial \tau_{ij}}{\partial x_i} \tag{3.16}$$

$$\frac{D\rho e}{Dt} = -p\frac{\partial u_i}{\partial x_i} + \tau_{ij}\frac{\partial u_j}{\partial x_j} + \frac{\partial}{\partial x_i}\left(k\frac{\partial T}{\partial x_i}\right) \tag{3.17}$$

$$\tau_{ij} = \mu\left(\frac{\partial u_i}{\partial x_j} + \frac{\partial u_i}{\partial x_i} - \frac{2}{3}\frac{\partial u_k}{\partial x_k}\delta_{ij}\right) \tag{3.18}$$

$$\frac{D}{Dt} = \frac{\partial}{\partial t} + u_i\frac{\partial}{\partial x_j} \tag{3.19}$$

$$i = 1, 2$$
$$j = 1, 2$$
$$k = 1, 2 \tag{3.20}$$
$$\delta_{ij} = \begin{cases} 1 & i = j \\ 0 & i \neq j \end{cases}$$

Assuming the gas to be calorically perfect (for low freestream enthalpy, chemical aspects can be neglected):

$$\gamma = \frac{C_p}{C_v}$$
$$C_p - C_v = R \tag{3.21}$$
$$e = C_vT + \frac{u_iu_j}{2}$$
$$p = \rho RT \tag{3.22}$$

where $\gamma = 1.4$ and $R = 287.05\ Jkg^{-1}K^{-1}$. And, the viscosity $\mu$ is calculated using the Sutherland relation :

$$\frac{\mu}{\mu_{ref}} = \left(\frac{T}{T_{ref}}\right)^{3/2}\frac{T_{ref} + S}{T + S} \tag{3.23}$$

where $\mu_{ref} = 1.789e5\ kgm^{-1}s^{-1}$, $T_{ref} = 288\ K$, and $S = 110\ K$. The thermal conductivity is defined as:

$$k = \frac{\mu C_p}{Pr} \tag{3.24}$$

18

The equations of the local piston theory used for approximating the unsteady aerodynamic pressure in low-fidelity models are:

Second Order:

$$p(x,t) = p_{loc}\left(1 + \frac{\gamma - 1}{2} M_{loc}\theta(t)\right)^{\frac{2\gamma}{\gamma-1}} \tag{3.25}$$

Third Order:

$$p(x,t) = p_{loc}\left(1 + \gamma M_{loc}\theta(t) + \gamma\frac{\gamma - 1}{4}(M_{loc}\theta(t))^2 + \gamma\frac{\gamma - 1}{4}(M_{loc}\theta(t))^3\right) \tag{3.26}$$

### 3.5.2  Structure

The general form of the equations of motion for a deformable body [52] are:

$$\frac{\partial \sigma_{xx}}{\partial x} + \frac{\partial \sigma_{yx}}{\partial y} + \frac{\partial \sigma_{zx}}{\partial z} + B_x = 0 \tag{3.27}$$

$$\frac{\partial \sigma_{xy}}{\partial x} + \frac{\partial \sigma_{yx}}{\partial y} + \frac{\partial \sigma_{zx}}{\partial z} + B_y = 0 \tag{3.28}$$

$$\frac{\partial \sigma_{xz}}{\partial x} + \frac{\partial \sigma_{yz}}{\partial y} + \frac{\partial \sigma_{zz}}{\partial z} + B_z = 0 \tag{3.29}$$

The Euler-Bernoulli beam model equation used in the 2D modeling of the plate for the low-fidelity methods is:

$$D\frac{\partial^4 w}{\partial x^4} = p(x,t) - \mu_m\frac{\partial^2 w}{\partial t^2} \tag{3.30}$$

where $D = EI/(1 - \nu^2)$ is the flexural rigidity, $\mu_m$ is the mass per unit length and $p$ is the net aerodynamic pressure acting on the structural element.

For a single beam element, the Finite Element Method (FEM) equation can be written as:

$$M\ddot{w} + \bar{D}\dot{w} + Kw = f \tag{3.31}$$

with,

$$M = \frac{\rho h l}{420} \begin{bmatrix} 156 & 22l & 54 & -13l \\ 22l & 4l^2 & 13l & -3l^2 \\ 54 & 13l & 156 & -22l \\ -13l & -3l^2 & -22l & 4l^2 \end{bmatrix} \tag{3.32}$$

$$K = \frac{D}{l^3} \begin{bmatrix} 12 & 6l & -12 & 6l \\ 6l & 4l^2 & -6l & 2l^2 \\ -12 & -6l & 12 & -6l \\ 6l & -2l^2 & -6l & 4l^2 \end{bmatrix} \tag{3.33}$$

$$f = \frac{l}{2} p(x,t) \begin{bmatrix} 1 \\ l/6 \\ 1 \\ -1/6 \end{bmatrix} \tag{3.34}$$

$$\bar{D} = \alpha M + \beta K \tag{3.35}$$

where, $f$ is the aerodynamic load, $\bar{D}$ is the damping matrix. $M$ is the mass matrix and $K$ is the stiffness matrix.

The stiffness damping coefficients $\alpha$ and $\beta$ (for Rayleigh damping) are obtained given the first two natural frequencies and the damping ratios:

$$\alpha = 2\omega_1\omega_2 \frac{\zeta_1\omega_2 - \zeta_2\omega_1}{\omega_2^2 - \omega_1^2} \tag{3.36}$$

$$\beta = 2\frac{\zeta_2\omega_2 - \zeta_1\omega_1}{\omega_2^2 - \omega_1^2} \tag{3.37}$$

with,

$$\zeta_1 = \zeta_2 = \zeta \tag{3.38}$$

### 3.5.3 FSI Interface

The interface region is paramount in FSI problems as this region separates both the fluid and structure domains. Also, the data transfer between fluid and solid solutions takes place through this region. For this, two sets of coupling conditions are specified: kinematic and dynamic coupling conditions [1].
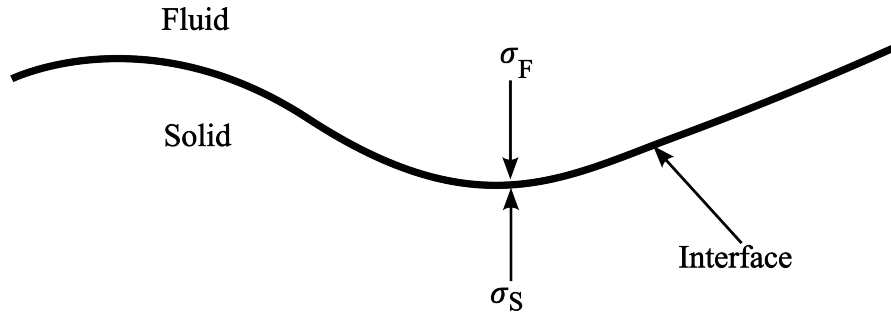
Figure 3.5: Fluid-Solid Interface in FSI

The kinematic coupling condition ensures that the fluid and structure have the same velocity as well as displacement at the interface.

$$x_F = w_S \tag{3.39}$$

$$v_F = \frac{\partial w_S}{\partial t} \tag{3.40}$$

Similarly, the dynamic coupling condition ensures the stress or force balance between the fluid and structure.

$$\sigma_F \cdot n_F = -\sigma_S \cdot n_S \tag{3.41}$$

## 3.6  FSI Coupling

### 3.6.1  Monolithic and Partitioned Approach

The governing equations of fluid, structure, and interface coupling conditions are solved simultaneously within a single set of discretized equations in the monolithic approach. Thus, a single specialized FSI solver is required for this approach. The FSI solution of the monolithic approach is considered to be exact with the error only coming from the numerical scheme used in the discretization. However, developing a monolithic approach from scratch is cumbersome for coding.
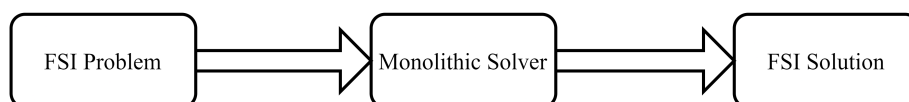


Figure 3.6: Schematic of Monolithic FSI Approach

The partitioned approach uses separate solvers for fluid and structure and a coupling application is used to solve for the interface coupling conditions and data transfer between fluid and structure. Existing robust and accurate solvers available can be used in this approach and additional coding may be done for the coupling part. Since the data transfer between fluid and structure is done only after a discrete coupling time, this approach gives errors compared to the monolithic solution. The partitioned approach can be further classified as explicit or implicit based on the number of times two separate solvers are solved or the number of times interface data is exchanged in a single coupling timestep.
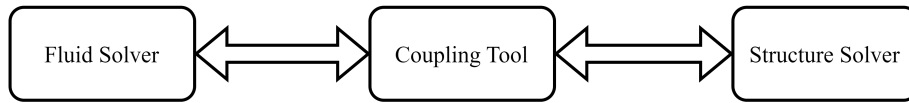


Figure 3.7: Schematic of Partitioned FSI Approach

### 3.6.2 Explicit Coupling

In the explicit coupling algorithm, the fluid and structure solvers are solved for a fixed number of iterations ( mostly a single iteration) and thus proper kinematic and dynamic balance may not be reached. Thus, explicit coupling might be unstable in cases with strong interactions where larger structure displacement occurs in a single timestep.

Explicit coupling can again be serial or parallel explicit coupling based on the order of execution. In serial explicit coupling, one solver executes its timestep first from $t_n$ to $t_{n+1}$. The second solver then executes its timestep after taking the solved boundary output from the first solver as its input. If $x_1$ and $x_2$ denote the input variables of the solver $S_1$ and $S_2$, then the solution step in serial explicit coupling is given by;

$$x_2^{(n+1)} = S_1^{(n)}(x_1^{(n)}) \tag{3.42}$$

$$x_1^{(n+1)} = S_2^{(n)}(x_2^{(n+1)}) \tag{3.43}$$
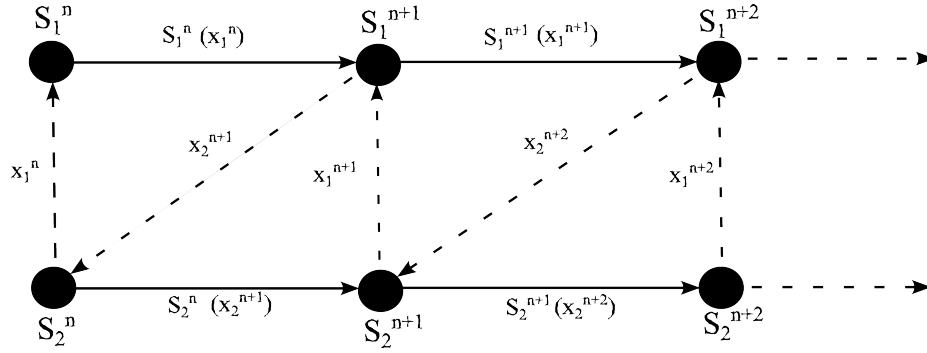
Figure 3.8: Schematic of Serial Coupling

In the parallel explicit coupling, both the solvers are executed simultaneously taking the input of the previous timestep in both the solvers.

$$x_2^{(n+1)} = S_1^{(n)}(x_1^{(n)}) \tag{3.44}$$

$$x_1^{(n+1)} = S_2^{(n)}(x_2^{(n)}) \tag{3.45}$$
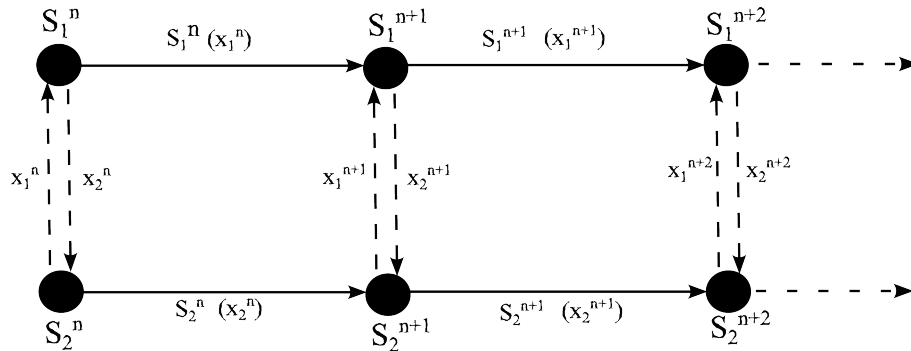


Figure 3.9: Schematic of Parallel Coupling

### 3.6.3 Implicit Coupling

In the implicit coupling algorithm, the fluid and structure solvers are solved iteratively for many sub-iterations with the exchange of dynamic and kinematic interface data in every sub-iterations until convergence. Thus, the implicit solution approaches to the accuracy of a monolithic approach with strict convergence criteria, however, it becomes computationally expensive.

Like explicit coupling, the implicit coupling can also be classified as serial and parallel.

The fixed point iteration equations for the serial implicit scheme are as follows;

$$x_2^{(n+1),i+1} = S_1^{(n)}(x_1^{(n+1),i})$$ (3.46)

$$x_1^{(n+1),i+1} = S_2^{(n)}(x_2^{(n+1),i+1})$$ (3.47)

Similarly, the equations for parallel implicit coupling scheme are written as;

$$x_2^{(n+1),i+1} = S_1^{(n)}(x_1^{(n+1),i})$$ (3.48)

$$x_1^{(n+1),i+1} = S_2^{(n)}(x_2^{(n+1),i})$$ (3.49)

Implicit coupling requires high computation costs as the number of sub-iterations increases with strict convergence criteria. For faster convergence, techniques like under-relaxation and sophisticated quasi-Newton solvers are found to be used [53].

# CHAPTER FOUR: METHODOLOGY

The flowchart of the methodology used during this work is shown in figure 4.1. Two approaches were used for aeroelastic predictions in this study: Low-fidelity Modelling (LFM) and High-fidelity Modelling (HFM).
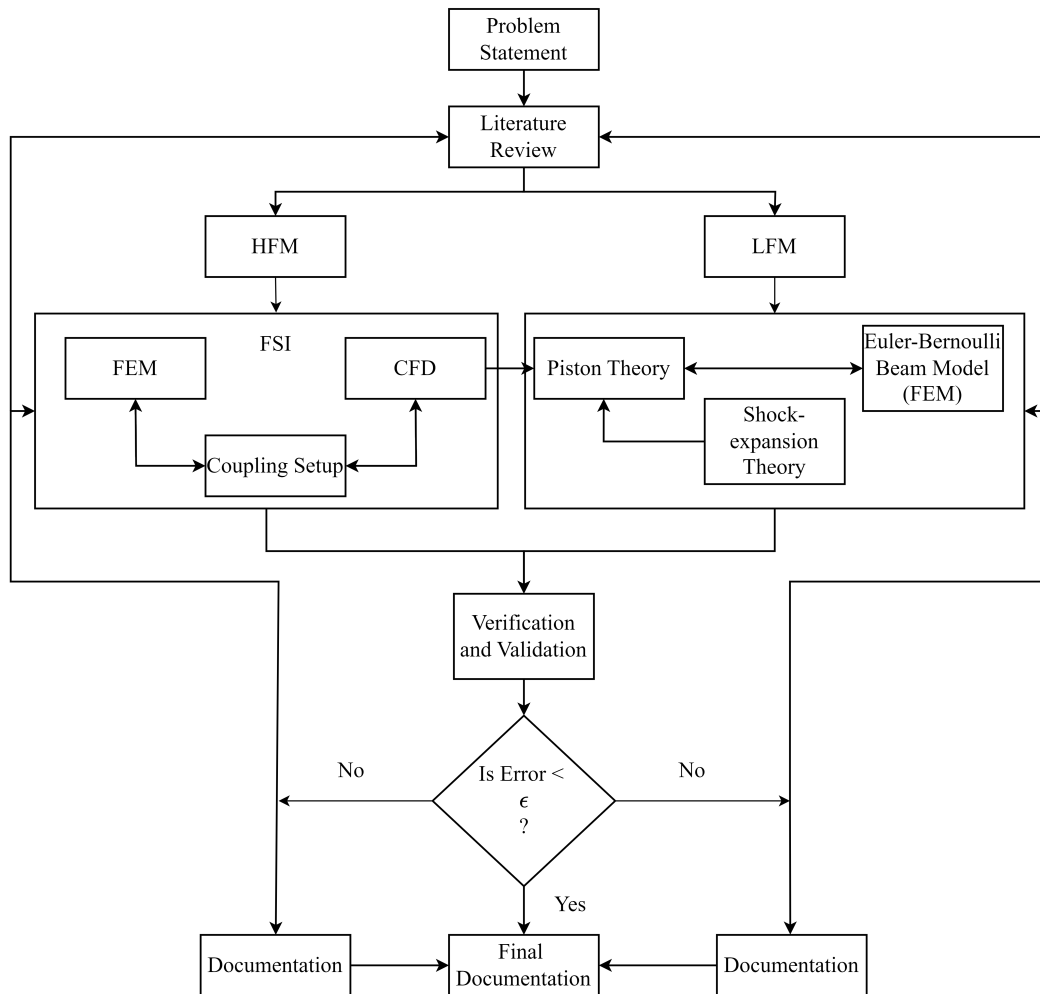
Figure 4.1: Methodology Flowchart

In LFM, the plate was modeled as a 2D cantilevered plate using the Euler-Bernoulli beam model and used both the analytical and the CFD-enriched local piston theory for unsteady pressure approximations. The initial flow conditions for the analytical and the CFD-enriched piston theory were obtained using the Shock-Expansion theory and the steady-state CFD solutions respectively.

In HFM, the fluid setup in OpenFOAM and the solid setup in CalculiuX were coupled using a coupling setup in PreCICE.

Verification and validation are important steps in any numerical simulation. [54] and [55] describe verification as "solving the equations right" and validation as "solving the right equations". In [56], the distinction is made between the two in terms of conceptual modeling errors and numerical modeling errors, validation addressing conceptual modeling errors and verification addressing numerical errors.

Verification can further be divided into code verification and calculation verification [57]. Code verification for high-fidelity modeling is outside the domain of our study, and calculation verification is achieved through the means of the Grid Convergence Study.

## 4.1 Geometry

Figure 4.2 shows the schematic of the geometry used in the HyMAX experiment (with a=130mm, b=80mm, and h=2mm). It consists of a wedge-shaped shock generator that is used to impinge a shock wave on the flat plate. The shock generator can be pivoted about the pivot point (shown in the sub-figure of Figure 4.2) to change the flow deflection angle such that the strength of the impinging shock can be varied. The shock generator can either be fixed at a particular flow deflection angle or made to oscillate freely about the pivot point. The flat plate, upon which the effect of the impinging shock is studied, is fixed/clamped at one of its ends with the help of the hammerhead. This configuration of the flat plate is commonly referred to as the Clamped-Free-Free-Free configuration in these kinds of experiments. The naming convention is based on the boundary condition at each edge of the flat plate. This is one of the possible 21 different types of structural boundary conditions that can be used to describe the clamping at each edge of the flat plate [58].

For the current study, the shock generator was fixed so that the flow deflection angle ($\theta$) becomes $10°$ as can be seen in Figure 4.3.
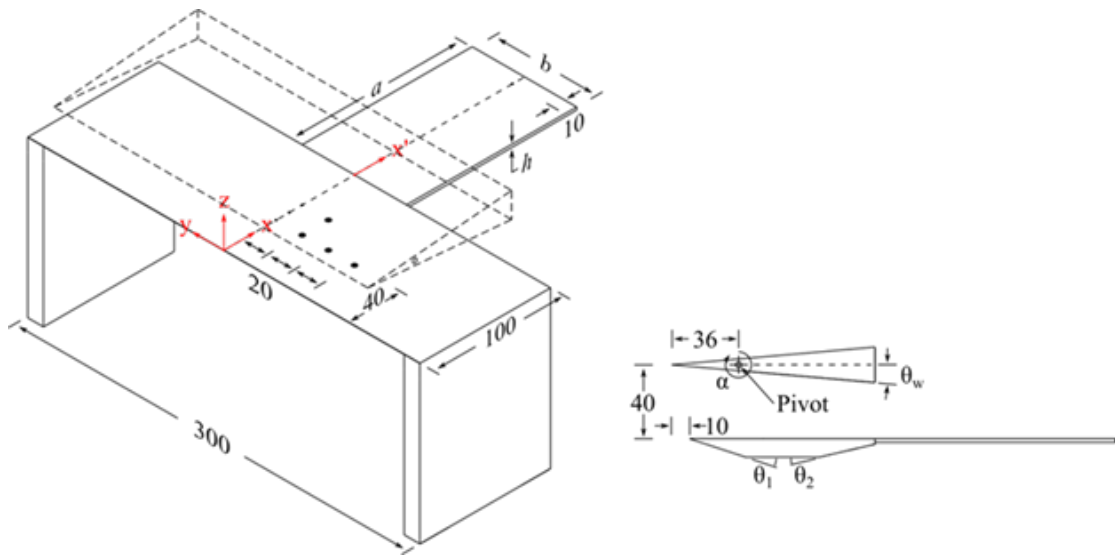
Figure 4.2: Geometry (Schematic)
[42]
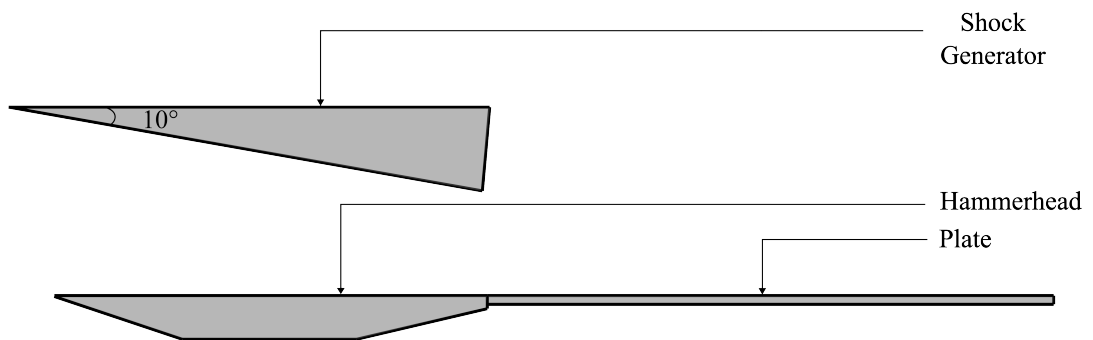


Figure 4.3: Geometrical Model Used in CFD

## 4.2 Low Fidelity Modeling
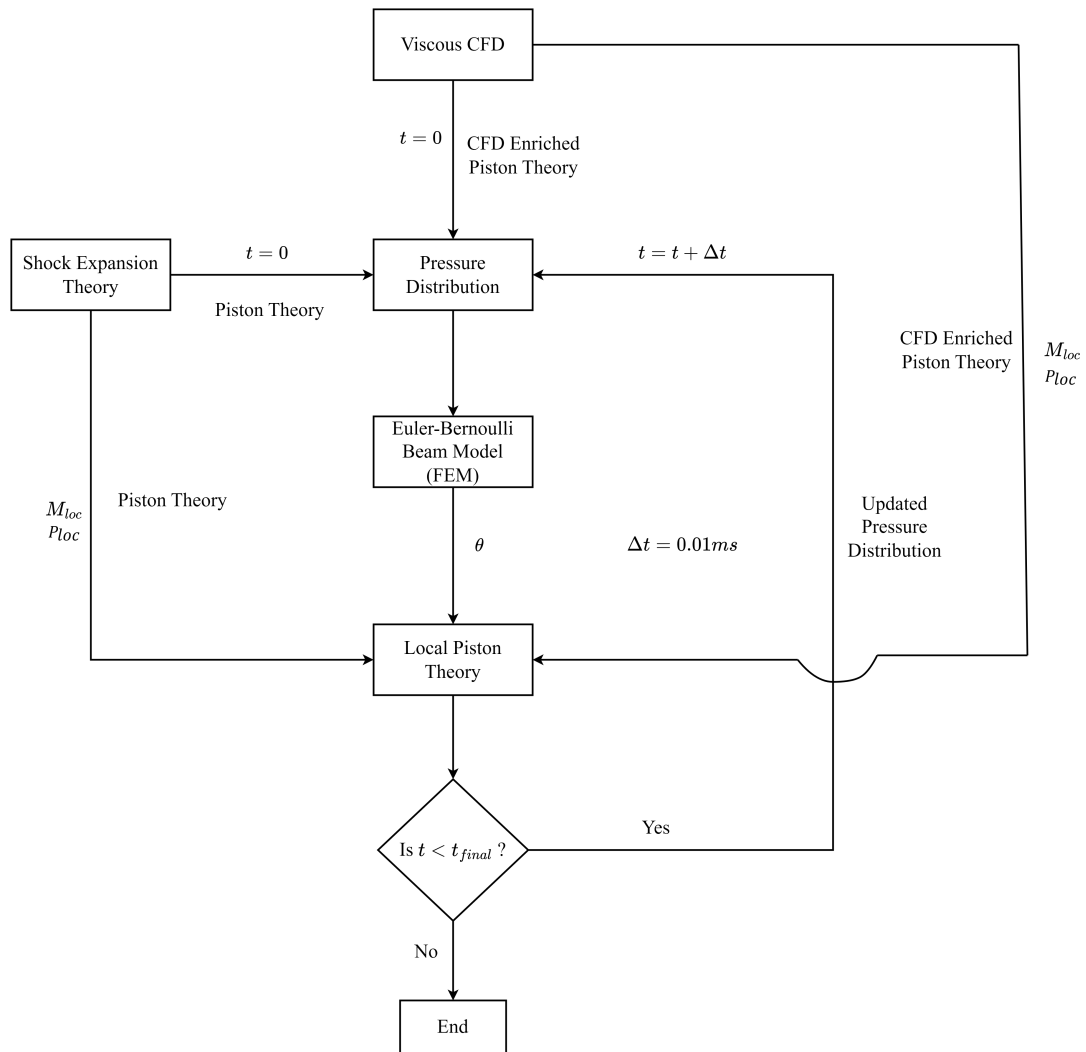


Figure 4.4: LFM Methodology

## 4.2.1 Aerodynamic Pressure Model

The time-dependent aerodynamic pressure acting on the top of the plate was computed using the local PT and the pressure under the plate was assumed to be constant and equal to the freestream pressure.

The initial pressure distribution (at t = 0) on the top and the bottom of the plate was obtained by using the following two methods:

### 4.2.1.1 Shock-Expansion Theory

The Shock-Expansion theory was used to calculate the required flow quantities (Mach number and pressure), considering the flow to be inviscid as shown in Figure 4.5.
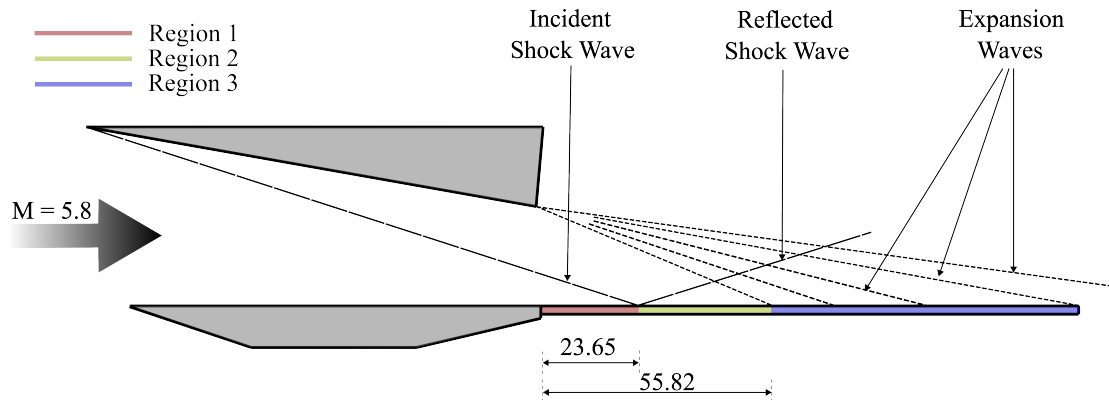


Figure 4.5: Schematic of Analytic Inviscid Flow

At the top of the plate:

Region 1 (Freestream)
$p = p_\infty = 755$ Pa
$M = M_\infty = 5.80$

Region 2 (After passing through the incident and the reflected shock waves)
$p = p_2 = 7412.45$ Pa
$M = M_2 = 3.67$

Region 3 (Shock-expansion interaction region)
The pressure and the Mach number distributions were approximated by considering the interaction of the expansion fan and the reflected shock wave, by dividing the expansion fan into a number of expansion waves.

At the bottom of the plate (Regions 1, 2, and 3):
$p = p_\infty = 755$ Pa
$M = M_\infty = 5.80$

Figure 4.6 compares the pressure distribution over the plate obtained using shock-expansion theory with the steady state inviscid CFD simulation. It can be observed that shock-expansion theory, which assumes inviscid flow, was able to capture the pressure profile accurately when compared against inviscid CFD results.
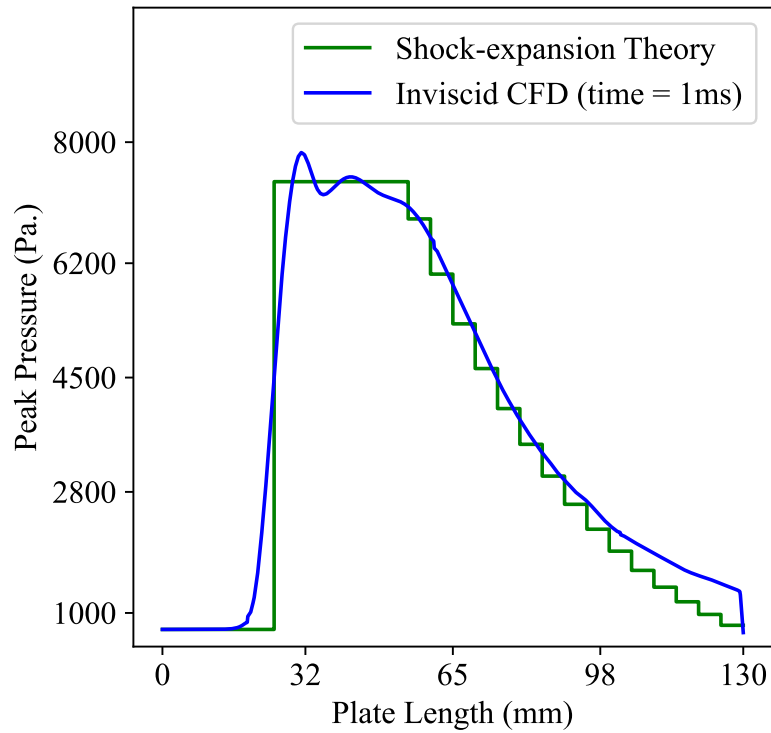
Figure 4.6: Initial Pressure Distribution over the Plate

#### 4.2.1.2 Steady-State CFD Analysis

The pressure distribution over the plate from Viscous CFD is given as input to the PT model. The model calculates the nodal pressure by searching for the nearest point in the given input profile. Also, to calculate the local Mach number, Equation 3.2 is used.

### 4.2.2 Structure Model

Using the Euler-Bernoulli beam model, the plate was modeled as a 2D cantilevered beam as shown in Figure 4.7.
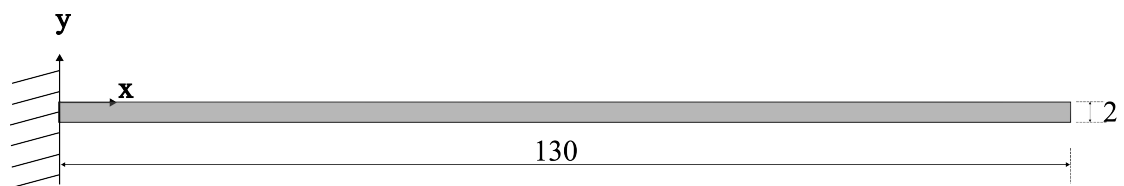


Figure 4.7: Low-fidelity Structural Model (2D Cantilevered Beam)

The equation of motion were solved using the FEM : $M\ddot{w} + \bar{D}\dot{w} + Kw = f$ where $M$, $\bar{D}$, $K$, and $f$ are mass matrix, damping matrix, stiffness matrix, and load vector respectively, defined in Equations 3.32 - 3.35.

Rayleigh (two-modes) damping model was used because the first two modes give the main contribution in terms of effective mass.

#### 4.2.2.1 Modal Analysis

Modal analysis is required to obtain the first two modes of vibration of the plate in order to calculate rayleigh damping coefficients. The first three mode shapes of the one-dimensional cantilevered plate, modeled for the piston theory application, are shown in Figure 4.8.
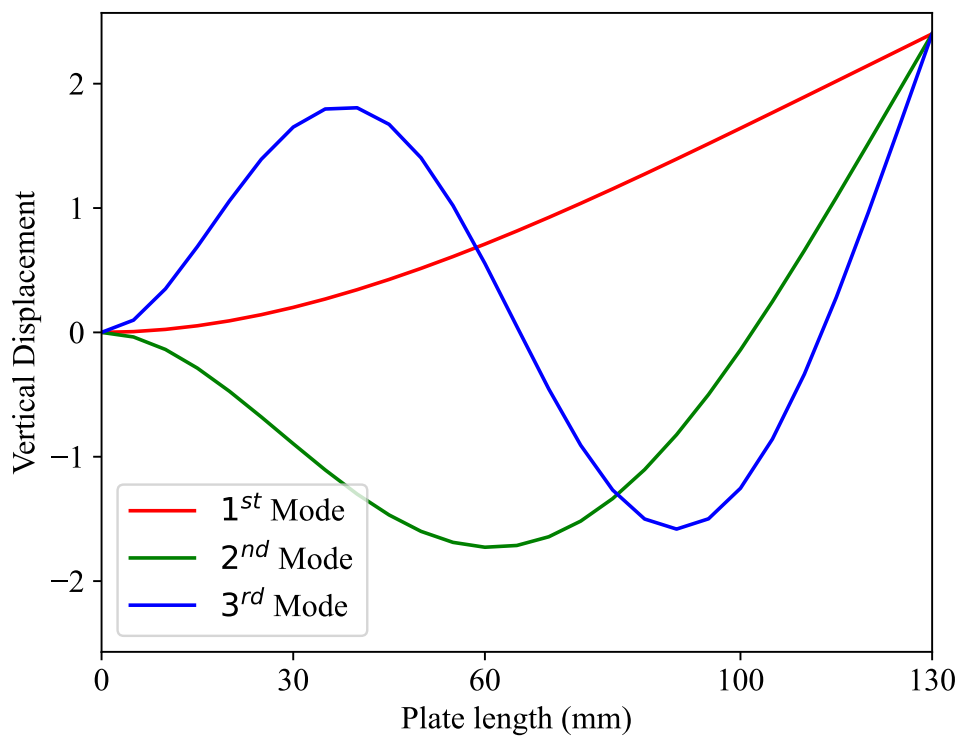


Figure 4.8: $1^{st}$, $2^{nd}$, and $3^{rd}$ Mode of Vibration

The first five modal frequencies are tabulated in Table 4.1.

31

Table 4.1: Modal Analysis (LFM)

| Mode | Frequency (Hz.) |
|------|-----------------|
| 1 | 85.0 |
| 2 | 532.9 |
| 3 | 1492.6 |
| 4 | 2925.7 |
| 5 | 4838.1 |

The Rayleigh damping coefficients, $\alpha$ and $\beta$, calculated using the first two modes were 3.5018 and $1.9572 * 10^{-6}$ respectively.

### 4.2.3 Comparison of Second and Third Order Piston Theory

A comparison was made between the third-order and the second-order piston theory in terms of peak pressure ratio with respect to the local deflection angle of the peak pressure location as can be seen in Figure 4.9. No significant difference was observed between the two, and thus any mention of piston theory in subsequent discussion refers to second-order piston theory.
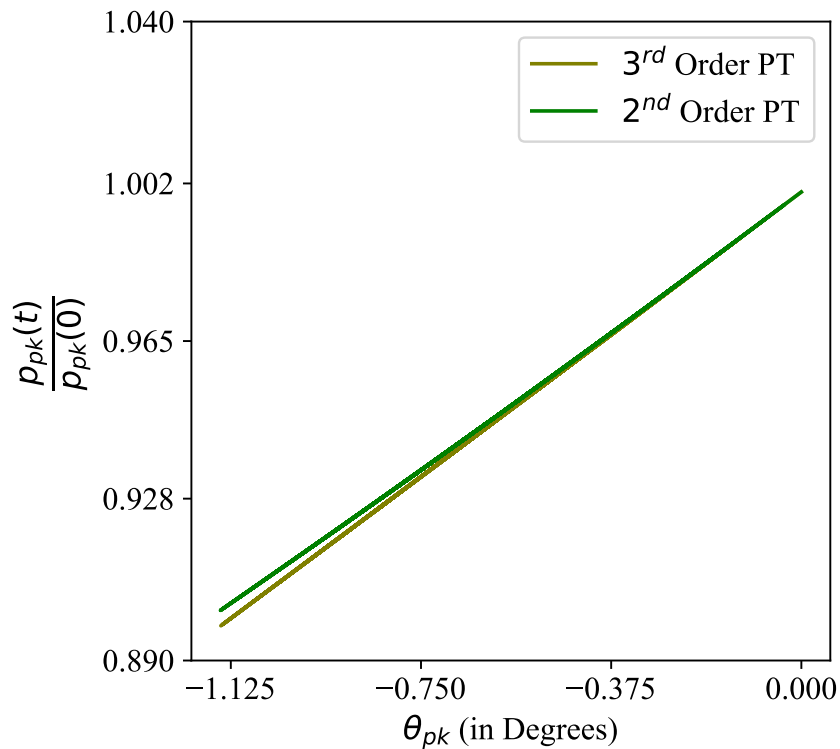


Figure 4.9: Peak Pressure Ratio against Local Deflection Angle

### 4.2.4   Validation of LFM

The LFM method used in this study was validated with the experimental results from the HyFoil experiment. Although the freestream pressure in the experiment is fluctuating, the average pressure was used in this model.

The LFM results show about 6% error in terms of trailing edge displacement, and a very small error of 0.7% in terms of oscillation frequency. Thus, the low-fidelity modeling method used in this study is validated.

### 4.2.5   Grid Convergence Study

Table 4.2: Grid Convergence Study of LFM

| No of Elements | TE Displacement CFD Enriched (mm) | TE Displacement SE based (mm) | Percent Change CFD Enriched | Percent Change SE Based |
|---|---|---|---|---|
| 26 | -3.45 | -3.41 | NA | NA |
| 32 | -3.54 | -3.53 | 2.63 | 3.52 |
| 40 | -3.62 | -3.47 | 2.22 | -1.71 |
| 50 | -3.69 | -3.44 | 1.78 | -0.98 |
| 63 | -3.74 | -3.51 | 1.42 | 2.16 |

The result of the grid convergence study is shown in Table 4.2. It can be observed that the CFD Enriched PT appears to be converging while the analytical PT appears to be oscillating around the same values.

Table 4.3: Computation Time of CFD-Enriched PT

| No of Elements | 26 | 32 | 40 | 50 | 63 |
|---|---|---|---|---|---|
| Time (s) (for 10 ms of flow duration) | 37.57 | 74.7 | 199.47 | 662.36 | 1682.47 |

Table 4.3 shows the computation time for 10 ms of flow duration for CFD Enriched PT.

Considering both, the accuracy (in terms of convergence), and the computation time, 26 elements were used for SE-based PT, and 50 elements were used for CFD Enriched PT.

## 4.3    High Fidelity Modeling

### 4.3.1    Solver Selection

Open-source platforms were prioritized over commercial platforms as they are free to use and offer high flexibility with customizable options. The publicly available source code also makes it easier to understand how the software works.

#### 4.3.1.1    Fluid Solver

rhoCentralFoam, a density-based solver in Open-source Field Operation and Manipulation (OpenFOAM), was selected as the fluid solver in our study.

OpenFOAM is an open-source software for CFD developed by the OpenFOAM Foundation. OpenFOAM is known for its flexibility and versatility, with a wide range of applications including the simulation of incompressible and compressible flows, multiphase flows, and heat transfer.

Both pressure-based and density-based solvers are available in OpenFOAM for compressible flow simulations. Pressure-based compressible solvers have been widely used for subsonic and transonic simulations while density-based solvers were developed for simulating high-speed flows with large density variations, such as those found in supersonic or hypersonic flows. In [59], a comparison is made between the pressure-based compressible solver, sonicFoam, and density-based solver, rhoCentralFoam, for high-speed cases: the supersonic wedge or ramp, the supersonic diamond airfoil, the two dimensional and the axially symmetric blunt bodies. The study found that rhoCentralFoam performs better in handling the supersonic flow simulation, as the sonicFoam would require as much as three times more cells to produce results of comparable quality.

### 4.3.1.2 Structure Solver

OpenFOAM has its own structural solver based on Finite Volume Method (FVM). However, FEM is considered to be more accurate than FVM for structural simulations. It is a common practice to use FVM for fluid and FEM for structure simulation in partitioned FSI approach[60, 41, 61]. Thus, FEM based solver in CalculiX was used.

CalculiX is an open-source Finite Element Analysis (FEA) software for structural mechanics simulations that can be used for fluid-structure interaction (FSI) simulations by coupling the structural solver with a fluid dynamics solver. It is a three-dimensional code that can be used for both linear and nonlinear analyses. This solver can be easily coupled with solvers in OpenFoam for partitioned FSI simulations. Thus, Calculix was selected as the structural solver for this study

### 4.3.1.3 Coupling Library

Precise Code Interaction Coupling Environment (PreCICE) was used to couple rhoCentralFoam and CalculiX solver in this study.

PreCICE is an open-source library for the coupling of simulation codes in a parallel computing environment. It provides an interface for coupling codes written in different programming languages, enabling the exchange of data between simulations in real-time. PreCICE supports both static and dynamic mesh coupling and provides various strategies for data transfer, such as linear interpolation or nearest-neighbor search. PreCICE is highly customizable supporting both serial ad parallel as well as explicit and implicit coupling. PreCICE has been validated with benchmark FSI cases of the flow around a cylinder with an attached flexible beam[5]. Since then, PreCICE has been used for partitioned FSI simulations[62, 63].

### 4.3.2 FSI System Overview

The fluid-structure-interaction case was then set up with rhoCentralFoam as the fluid solver, CalculiX as the structural solver, and PreCICE as the coupling library. Explicit coupling was done as it was computationally less expensive and takes less time.

Figure 4.10: Simple schematic of FSI

### 4.3.3 Modal Analysis

Completely 2D simulation cannot be done in OpenFOAM, i.e. the fluid domain must have some thickness along the third direction. Hence, in the fluid domain, a thickness of 2mm was specified in the z-direction with only 1 cell in that direction. Similarly, for the structural part, a 3D plate with a 2mm thickness was modeled. Two dimensionality was achieved by fixing the plate in the third (z) direction.

The first five modal frequencies of the two-dimensional plate are listed in Table 4.4.

Table 4.4: Modal Analysis (HFM)

| Mode | Frequency (Hz.) |
|------|-----------------|
| 1 | 90.0 |
| 2 | 563.5 |
| 3 | 1574.6 |
| 4 | 3077.1 |
| 5 | 5068.4 |

The Rayleigh damping coefficients, $\alpha$ and $\beta$, calculated using the first two modes were 3.7065 and $1.851 * 10^{-6}$ respectively.

### 4.3.4  Fluid Case Setup

#### 4.3.4.1  Computation Domain
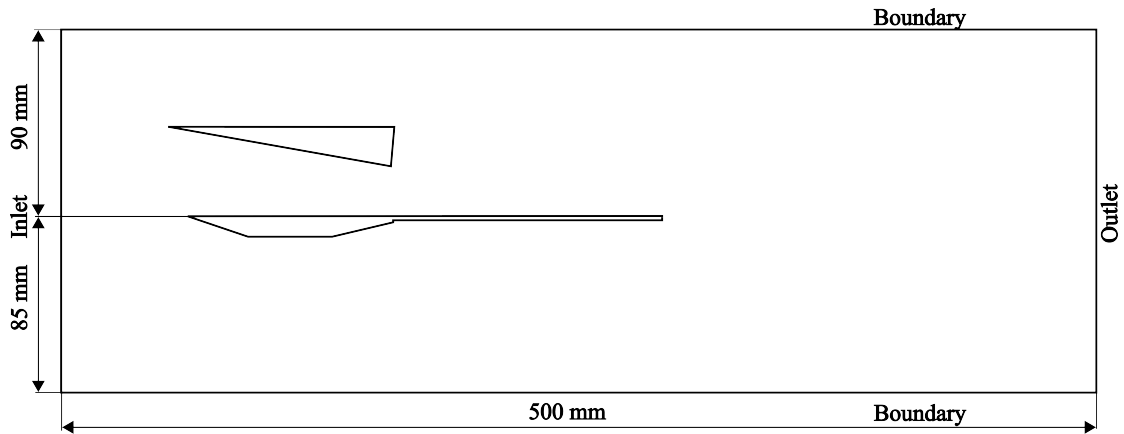


Figure 4.11: Computational Domain

The domain used for CFD simulations is shown in Figure 4.11. The domain consists of three external patches (inlet, outlet, and boundary), and three internal patches (shock-generator, plate, and hammerhead) (shown in Figure 4.3).

As information does not flow upstream in hypersonic flows (also in supersonic flows), and the boundary conditions applied have no room for shock reflection, rigorous domain size calculations, and domain size independent tests have not been done.

#### 4.3.4.2  Initial and Boundary Conditions

The initial conditions were taken as per the HyMAX experiment. The initial and boundary conditions are tabulated in Table 4.5, 4.6, and 4.7.

Table 4.5: Initial Flow Condition

| Flow Variable | Value |
| --- | --- |
| U | 1007.24 m/s |
| p | 755 Pa |
| T | 75 K |
| $T_w$ | 300 K |

37

Table 4.6: Boundary Conditions for Viscous Simulation

| Patch | U | p | T |
|---|---|---|---|
| Inlet | fixedValue | zeroGradient | fixedValue |
| Plate | noSlip (movingWallVelocity for FSI) | zeroGradient | fixedValue |
| Hammerhead | noSlip | zeroGradient | fixedValue |
| Wedge | noSlip | zeroGradient | fixedValue |
| Boundary | supersonicFreestream | zeroGradient | inletOutlet |
| Outlet | inletOutlet | waveTransmissive | inletOutlet |

Table 4.7: Boundary Conditions for Inviscid Simulation

| Patch | U | p | T |
|---|---|---|---|
| Inlet | fixedValue | zeroGradient | fixedValue |
| Plate | Slip (movingWallVelocity for FSI) | zeroGradient | fixedValue |
| Hammerhead | Slip | zeroGradient | fixedValue |
| Wedge | Slip | zeroGradient | fixedValue |
| Boundary | supersonicFreestream | zeroGradient | inletOutlet |
| Outlet | inletOutlet | waveTransmissive | inletOutlet |

### 4.3.4.3 Discretization

The model was discretized in time using the Euler scheme. This scheme is implicit and first-order accurate in time.

$$\frac{\partial \phi}{\partial t} = \frac{\phi - \phi^o}{\Delta t} \tag{4.1}$$

rhoCentralFoam is based on the central upwind scheme of Kurganov and Tadmor. Kurganov was used as the flux scheme [64]. This scheme is second-order accurate. Likewise, the gradient terms were discretized using the cellLimited Gauss linear scheme to ensure that the face values obtained by extrapolating the cell value to the cell faces using the gradient are bounded by the neighboring cell's minimum and maximum limit. This scheme is first-order accurate.

Laplacian terms in the governing equations were discretized using Gauss linear limited scheme. Here, the limited is used for explicit non-orthogonal correction of a surface normal gradient that is required to evaluate the laplacian term. This scheme is first-order accurate.

Gauss linear was used for divergence term discretization. Likewise, the linear scheme

was used as the default for the interpolation of variables. This scheme is first-order accurate. TVD schemes must be used for interpolation of reconstructed variables in rhoCentralFoam to reduce numerical oscillations [65, 66]. Of various TVD schemes, MinMod and VanAlbada schemes were found to work well in inviscid and viscous simulation respectively. TVD schemes are second-order accurate in space.

Table 4.8: Discretization schemes used and order of accuracy.

| Discretization | Scheme | Order of Accuracy |
| --- | --- | --- |
| Temporal | Euler Implicit | First |
| Flux | Kurganov | Second |
| Gradient | cellLimited Gauss linear | First |
| Laplacian | Gauss linear limited | First |
| Interpolation | MinMod (Inviscid) vanAlbada (Viscous) | Second |

#### 4.3.4.4 Solution Methods and Controls

The flux variables of the governing equations ($rho|rhoU|rhoE$) were first computed explicitly using the diagonal solver. Then the velocity vectors and energy variables were computed using the smoothSolver. The absolute and relative convergence tolerances for smoothSolver were set to 1e-10 and 0 respectively. Adjustable time stepping was used with a maximum courant number of 0.5 for fluid-only simulation, 0.2 for inviscid FSI simulation, and 0.5 for viscous FSI simulation.

Cell displacement of the fluid mesh also needs to be solved for FSI simulation. This was done using a GAMG solver with absolute and relative tolerance measures of 1e-6 and 1e-4 respectively.

#### 4.3.4.5 Mesh

blockMesh utility in OpenFOAM was used to generate structured mesh for the fluid domain. Meshing was done for both inviscid and viscous cases and also tested for grid independence.

The initial sizing of mesh has been done taking [17] as reference. For the laminar simulation of a similar experiment HyFoil_HH, the first cell is in the order of micrometres along the vertical direction, hence, the viscous meshing is done around this requirement.

The region of the mesh just above the plate has the highest refinement in both horizontal and vertical directions. This is done so as to capture the gradients, due to the phenomenon of SWBLI, shock-shock interaction, and shock-expansion interaction occurring in this region, accurately.

The region above the hammerhead also has high refinement requirements as the shock-waves and SWBLI, which will be relevant later (as FSI of the plate is studied), originate here.

The region of the geometry where expansion waves occur must be meshed carefully as these regions are highly susceptible to errors if not meshed carefully. The temperature oscillation (during CFD simulation) around the low-temperature values (due to the expansion waves) may cause the temperature to drop below 0 Kelvin. This may then cause solver crashes.

The mesh in the bottom and the side part of the plate cannot be very fine as compression in these regions of mesh when the plate deflects downwards may cause negative cell volume. The mesh in the upper part of the plate does not have such a requirement as the plate does not deflect upwards.

The meshing of all the other regions except the regions mentioned above is a compromise between the growth rate and the computational cost.

The inviscid mesh and the viscous mesh have similar requirements except that there are no boundary layers and SWBLI to capture in inviscid simulation. Hence, the meshing requirement of inviscid cases is not as demanding as that of the viscous case.

**Inviscid Grid Convergence Study**

Three sets of mesh (coarse, medium, and fine), each differing from the other by a factor of 2 (more or less), were used for the purpose of the Grid Convergence Study. Peak pressure over the plate was selected as the convergence test parameter.

Richardson extrapolation method was used to calculate the value convergence parameter would reach when $\Delta x \rightarrow 0$ and $\Delta y \rightarrow 0$. Subsequent calculation of order of convergence and Grid Convergence Index (GCI) was done taking [56] as reference. GCI was calculated by taking the safety factor as 1.25.

The exact value of Peak Pressure obtained from Richardson Extrapolation was 7797.64 Pa. Also, the order of convergence obtained was 2.7037.

Table 4.9: Grid Convergence Study Inviscid

| Mesh | Number of Cells | Peak Pressure (Pa) | Percentage Error From Exact Value |
|---|---|---|---|
| Coarse | 17749 | 8133.2 | 4.30% |
| Medium | 36381 | 7845.4 | 0.61% |
| Fine | 72904 | 7804.5 | 0.09% |
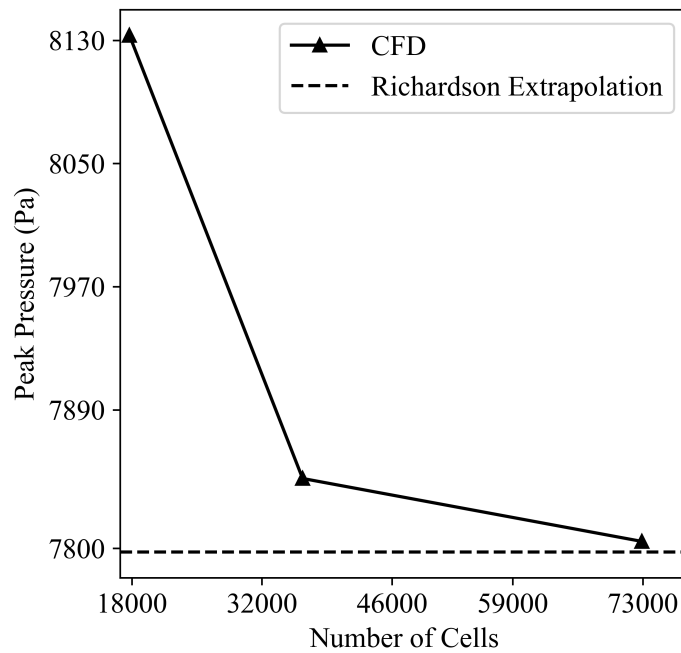


Figure 4.12: Grid Convergence Test Inviscid

Table 4.10: G.C.I. Inviscid Mesh

| Mesh | G.C.I. |
|---|---|
| Coarse-Medium | 0.77 |
| Medium-Fine | 0.12 |

The convergence criteria was set as: G.C.I. < 0.2. The medium mesh was within the asymptotic range of convergence with a value of 0.9947. Hence, the medium mesh with 36381 cells was considered converged. The converged mesh's parameters are tabulated in table 4.11.

Table 4.11: Converged Inviscid Mesh's Parameters

| Number of Cells | min $\Delta x$ (mm) | max $\Delta x$ (mm) | min $\Delta y$ (mm) | max $\Delta y$ (mm) |
|---|---|---|---|---|
| 36381 | 0.70 | 1.12 | 0.5 | 9.90 |

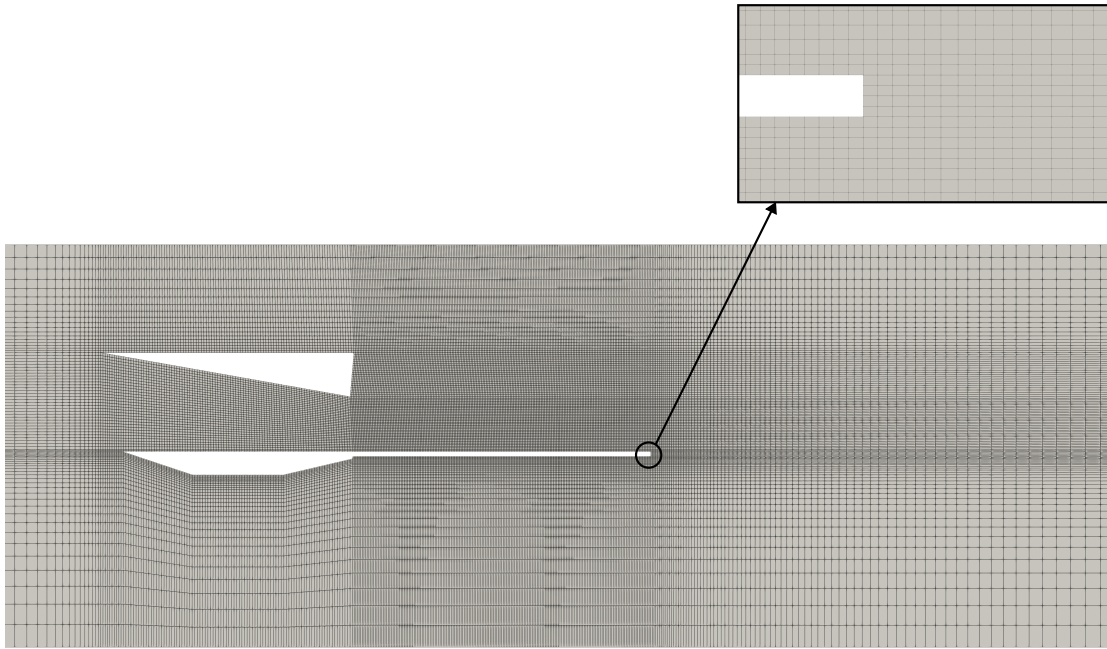Figure 4.13 shows the converged mesh for the inviscid case.



Figure 4.13: Converged Mesh for Inviscid Case

**Viscous Grid Convergence Study**

Mesh Convergence Test was done with five different levels of mesh, each mesh differing from the other by a factor of 2. The reattachment point was selected as the convergence test parameter.

Table 4.12: Grid Convergence Study Viscous

| Mesh | Number of Cells | Reattachment Point (mm) | Percent Error from Exact Value |
|---|---|---|---|
| - | 9830 | 118.68 | 5.21% |
| - | 19808 | 122.36 | 3.26% |
| Coarse | 39810 | 126.27 | 1.19% |
| Medium | 80410 | 127.88 | 0.33% |
| Fine | 160567 | 128.34 | 0.09% |

The exact value of the reattachment point obtained from Richardson Extrapolation was 128.5 mm from the hammerhead's leading edge. Also, the order of convergence obtained was 1.7701.
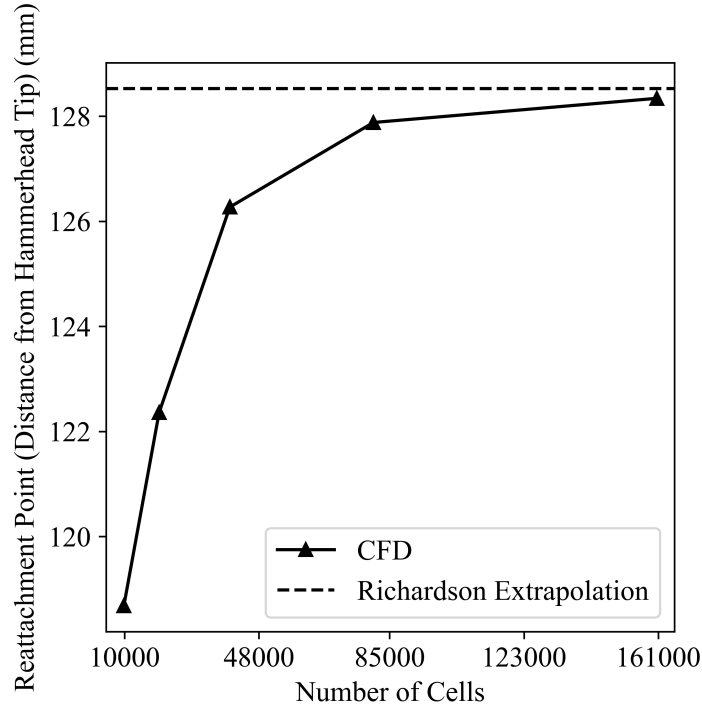


Figure 4.14: Grid Convergence Study Viscous

Table 4.13: G.C.I. Viscous Mesh

| Mesh | G.C.I. |
|---|---|
| Coarse-Medium | 0.434 |
| Medium-Fine | 0.127 |

The medium mesh with G.C.I. < 0.2 was considered converged. It was within the asymptotic range of convergence with a value of 1.0024.

The converged mesh's parameters are tabulated in table 4.14.

Table 4.14: Viscous Converged Mesh's Parameters

| Number of Cells | BL Grid (m) | $y_f$ (m) | $y_l$ (m) | $\Delta x_{min}$ (m) | $\Delta x_{max}$ (m) | $\Delta y_{min}$ (m) (Outside BL) | $\Delta y_{max}$ (m) |
|---|---|---|---|---|---|---|---|
| 80410 | 1e-3 | 6.45e-6 | 1.34e-4 | 4.93e-4 | 1.60e-2 | 1.67e-4 | 1.15e-2 |

Here subscripts f and l refer to the first and the last cell of the boundary layer grid. The

boundary layer grid is a highly refined zone in the mesh meant to capture the boundary layer characteristics.

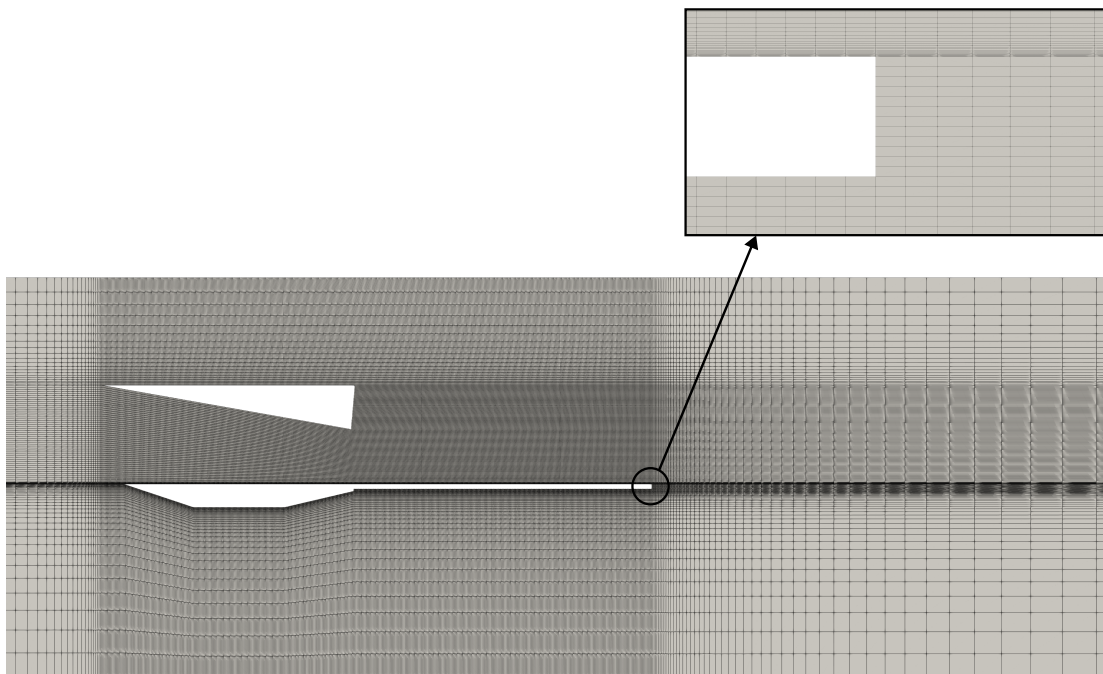Figure 4.15 shows the final grid-independent mesh for the viscous case.



Figure 4.15: Converged Mesh for Viscous Case

#### 4.3.4.6 Dynamic Mesh Morphing

One of the major challenges in FSI simulation is dynamic mesh control. During the simulation, the interface mesh should deform without distortion which might affect the solver's performance and eventually cause the solver to crash. Dynamic mesh configuration can be configured in the dynamicMeshdict file inside the fluid case where we define the motion solver to use and the mesh diffusivity. A mesh motion solver is required to solve the equation of cell motion with a given boundary motion while the diffusivity will determine e how the points should be moved when solving the cell motion equation for each time step.

OpenFOAM has various mesh motion solvers available for use. However, only displacement-based mesh motion solvers were compatible with preCICE coupling during this study. Thus, the displacementLaplacian solver was selected as the mesh motion solver. DisplacementLaplacian is based on solving the cell-center Laplacian for the motion dis-

placement.

$$\nabla.(\lambda d_m.\nabla) = 0$$
$$\lambda \propto \frac{1}{l^2} \tag{4.2}$$

The diffusivity coefficient was defined as the quadratic inverse distance from the plate. This implies that the diffusivity decreases quadratically on the points away from the plate. Simply put, cells deformed or stretched more on the outer cells while the inner cells remained almost the same. This ensures that the fine mesh in the boundary layer region moves together with the plate rigidly preventing mesh distortion and negative cell volume.

### 4.3.5  Structure Case Setup

#### 4.3.5.1  Mesh

A tetrahedral mesh of size 0.8 mm was generated using PrePoMax software.



Figure 4.16: Solid-Mesh

#### 4.3.5.2  Boundary Conditions and Input

All the boundary conditions and input values were assigned in the inp file in CalculiX. For the boundary condition, fixed support was applied at the cantilevered end of the plate by restraining motion in all degrees of freedom at the nodes. All other nodes were allowed to move freely except the z-direction as this is a 2D case.

Table 4.15: Material Properties of Structure

| Material Properties | Value |
|---------------------|-------|
| Density | 2670 kg/m3 |
| Young's Modulus | 527 MPa |
| Poisson's Ratio | 0.33 |
| Rayleigh Damping Coefficients | $\alpha = 3.7065$ , $\beta = 1.851 * 10^{-6}$ |

### 4.3.5.3  Discretization and Solution Method

Spatial discretization in CalculiX linear solver was done by Finite Element Method(FEM) while an explicit time integration method was used to discretize the time domain into a number of small time steps. After discretization, the equations were solved by using the Spooles solver.

### 4.3.6  FSI Coupling

The coupling numerics were specified in the precice-config.xml file.

A serial explicit coupling scheme was used with fluid as the first participant and solid as the second participant. For both the inviscid and viscous FSI cases, the coupling time was set to 0.01 ms. With smaller coupling time of 0.01 ms, the deformation of plate at each coupling time-step was smaller. The problem of mesh distortion and negative cell volume was encountered when using higher coupling time, especially in the viscous case.

Before starting the FSI simulation, a steady-state solution for fluid flow was obtained through fluid-only simulation. This solution would be the initial fluid condition for FSI simulation. During the FSI simulation, the fluid solver runs until the coupling time and then maps the forces data to the nodes of the structure mesh using the nearest-neighbor mapping algorithm. Now the CalculiX linear solver calculates the displacement of nodes and then maps the displacements back to the fluid mesh using the same mapping algorithm. This continues until all the coupling steps are completed. The schematic of coupling configuration and data mapping is shown in Figure 4.17.
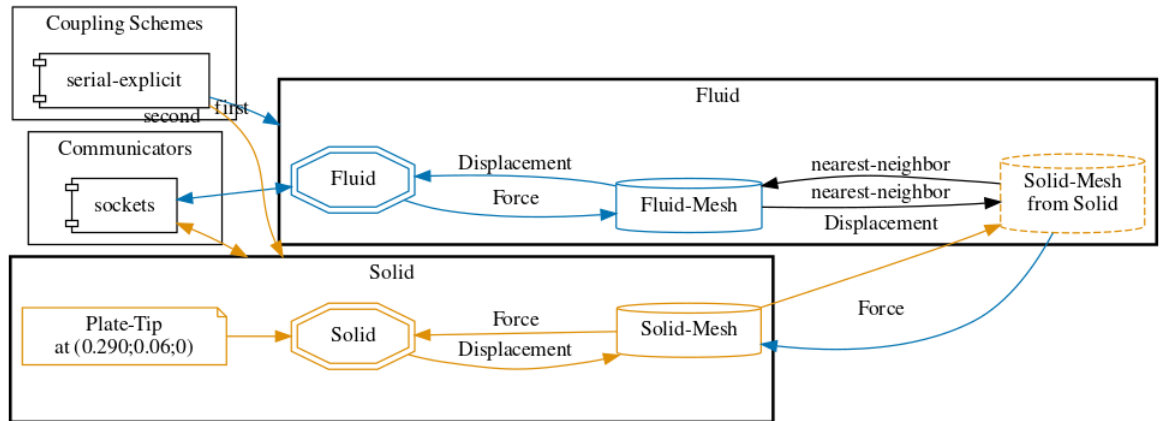
Figure 4.17: FSI Coupling Schematic

Serial implicit coupling was also done for inviscid FSI to compare the results against explicit coupling. A comparison between the implicitly and the explicitly coupled FSI simulations on the basis of trailing edge displacement history is shown in Figure 4.18. The average trailing edge displacement between the two differs just by 0.077%.
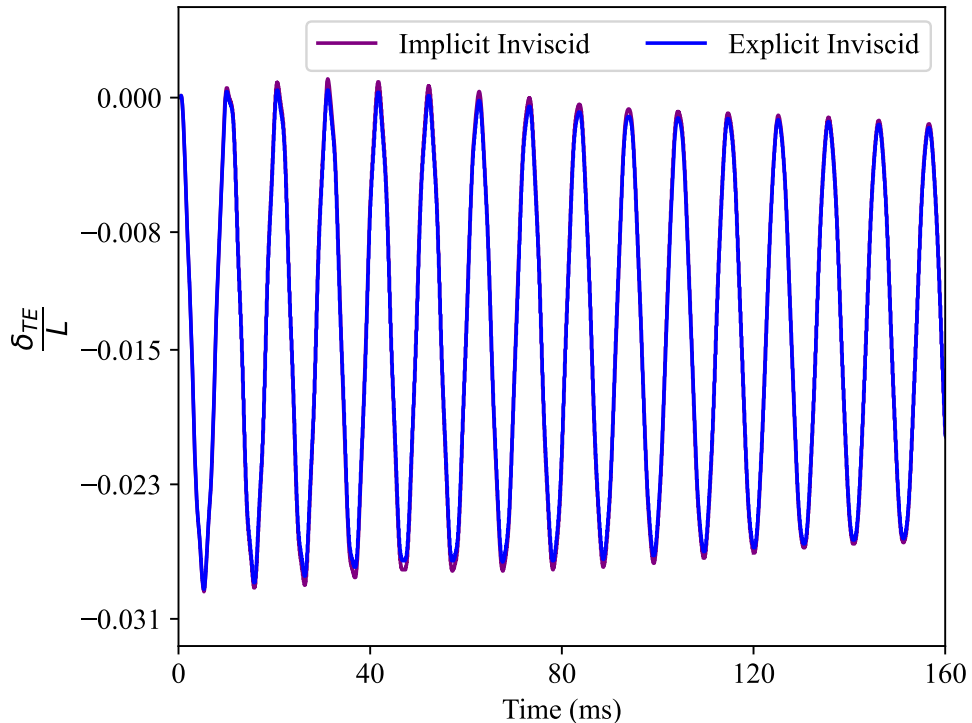


Figure 4.18: Trailing Edge Displacement History for Explicit and Implicit Coupling in Inviscid FSI

A comparison between the two types of simulation was also made on the basis of computation time (for 200 ms) as can be seen in Table 4.16.

Table 4.16: Computation time required for explicit and implicit coupling

| Coupling Scheme | Computation Time |
|---|---|
| Explicit coupling | 24 hours |
| Implicit Coupling | 130 hours |

It is evident that explicit coupling is able to produce very similar results with about three times less computation time. Hence, in viscous FSI simulation, only explicit coupling was done, and the mention of FSI simulation in further discussion refers to explicitly coupled simulations.

# CHAPTER FIVE: RESULTS AND DISCUSSION

## 5.1 Results

### 5.1.1 High Fidelity Modeling (HFM)

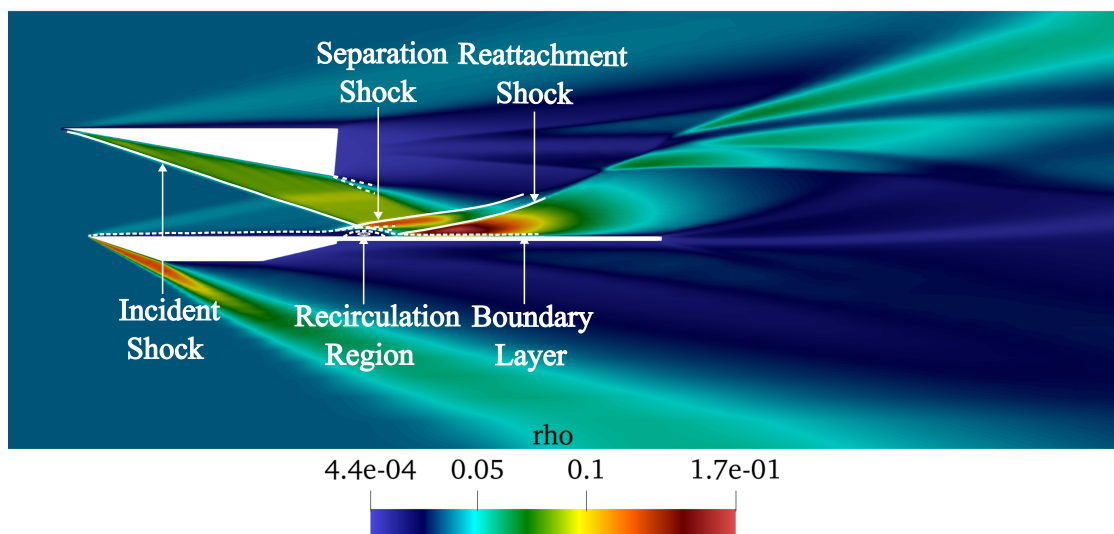#### 5.1.1.1 Shock-Wave Boundary Layer Interaction (SWBLI)



Figure 5.1: Density Contour (time = 0.5ms)

The phenomenon of SWBLI can be clearly seen in Figure 5.1. Although the down-stream information does not reach upstream in supersonic flows, as the boundary layer is not completely supersonic, the existence of adverse pressure gradient due to shock-wave impingement is detected by the upstream subsonic boundary layer flow through the downstream subsonic boundary layer flow. This causes the upstream flow to sep-arate, resulting in the formation of an Induced Separation Shockwave. The flow reat-taches after passing through shockwaves (incident, separation, and reattachment) and expansion waves as it gains a favorable pressure gradient as shown in figure 5.1.
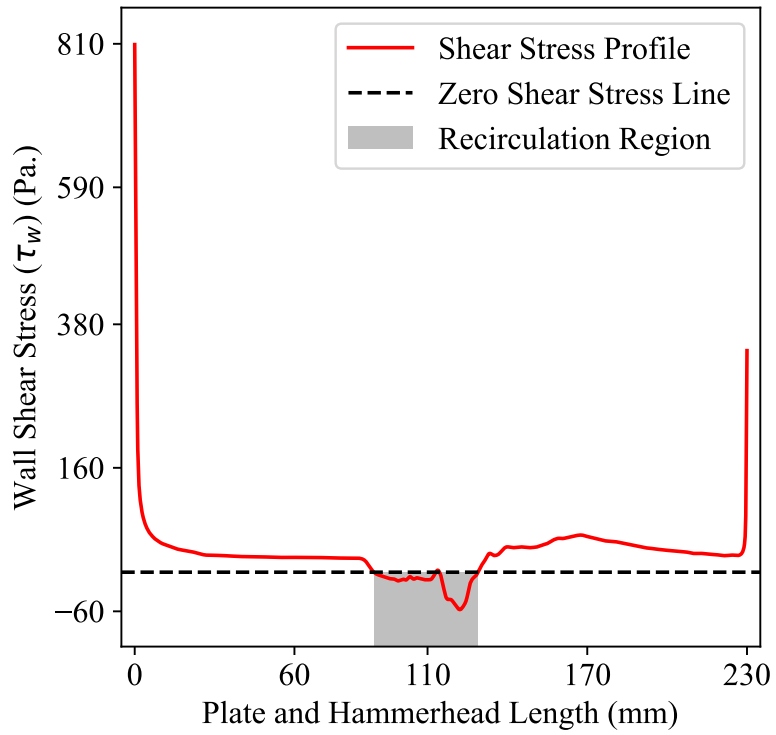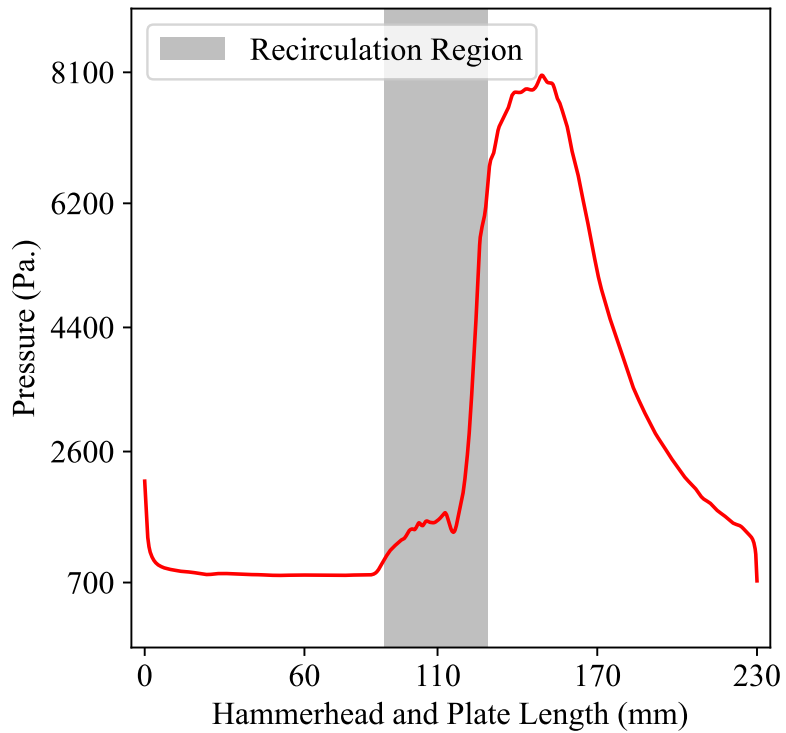
Figure 5.2: Shear Stress Profile (time = 1 ms)



Figure 5.3: Pressure Distribution Over Hammerhead and Plate (time = 1 ms)

Shear stress distribution over the hammerhead and plate gives the location of the separation point, recirculation region, and reattachment point as shown in Figure 5.2. The pressure distribution plot shown in Figure 5.3 also captures the effect of SWBLI. The pressure increases first around the separation region due to the separation shock, then a pressure plateau is formed in the recirculation region and a slight dip in pressure is observed due to the expansion fan when the flow reattaches. Finally, the pressure rises again at the reattachment point due to the reattachment shock and another pressure plateau is formed. This pressure profile is in accordance with the expected pressure distribution in the case of laminar simulation.

### 5.1.1.2   Inviscid FSI

In Figure 5.4, the evolution of peak pressure with time is plotted. The peak pressure oscillation consists of two distinct frequencies of 100.0 Hz and 571.43 Hz, close to the first mode (90.02 Hz) and the second mode (563.47 Hz) of the plate deflection respectively, as seen in the Figure 5.5.

From Figures 5.6 and 5.7, it can be seen that the plate oscillates with a maximum displacement of 3.8 mm and an oscillation frequency of 90.02 Hz, dominated by the first mode of the natural frequency of the plate deformation.
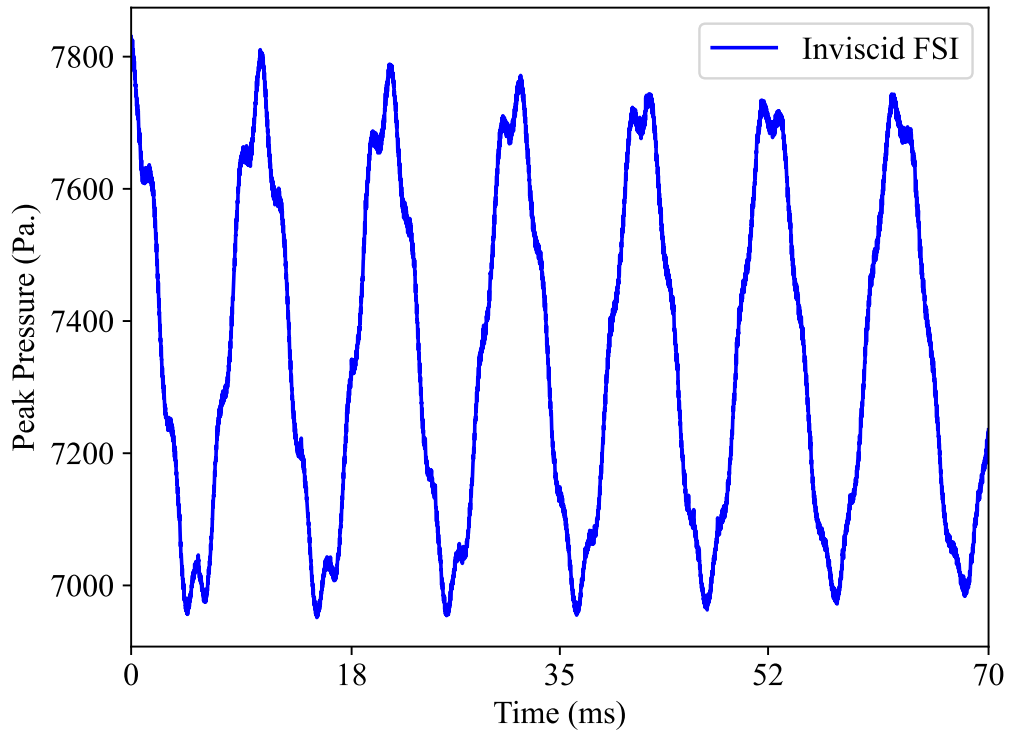
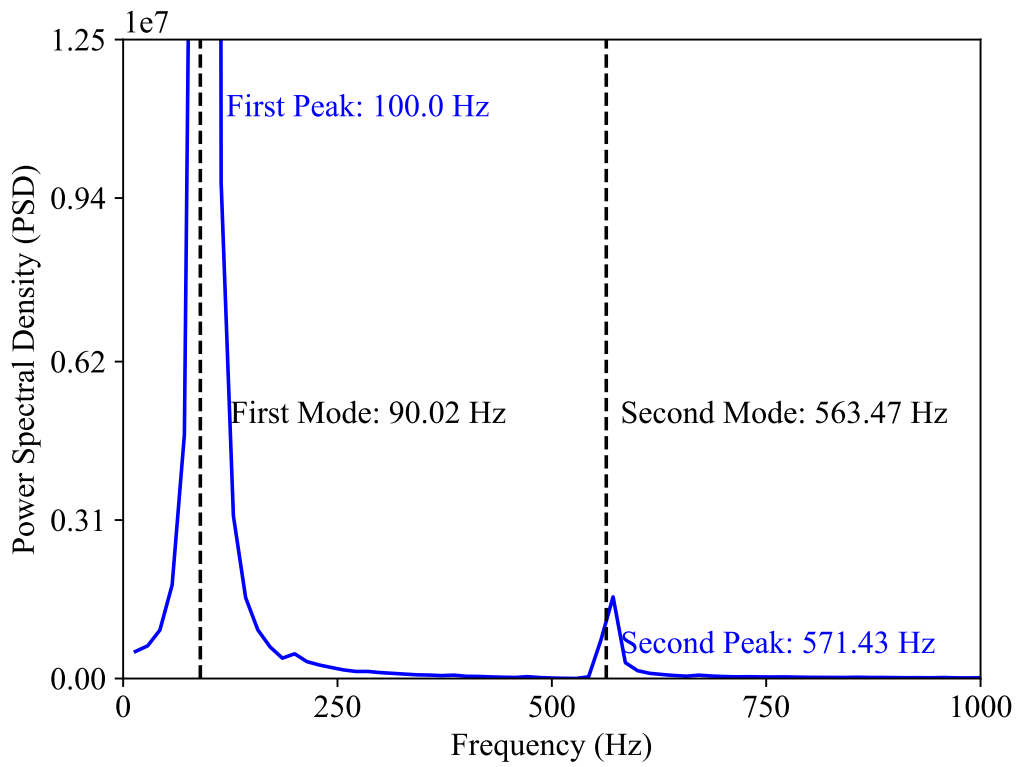Figure 5.4: Peak Pressure Evolution with Time (Inviscid)



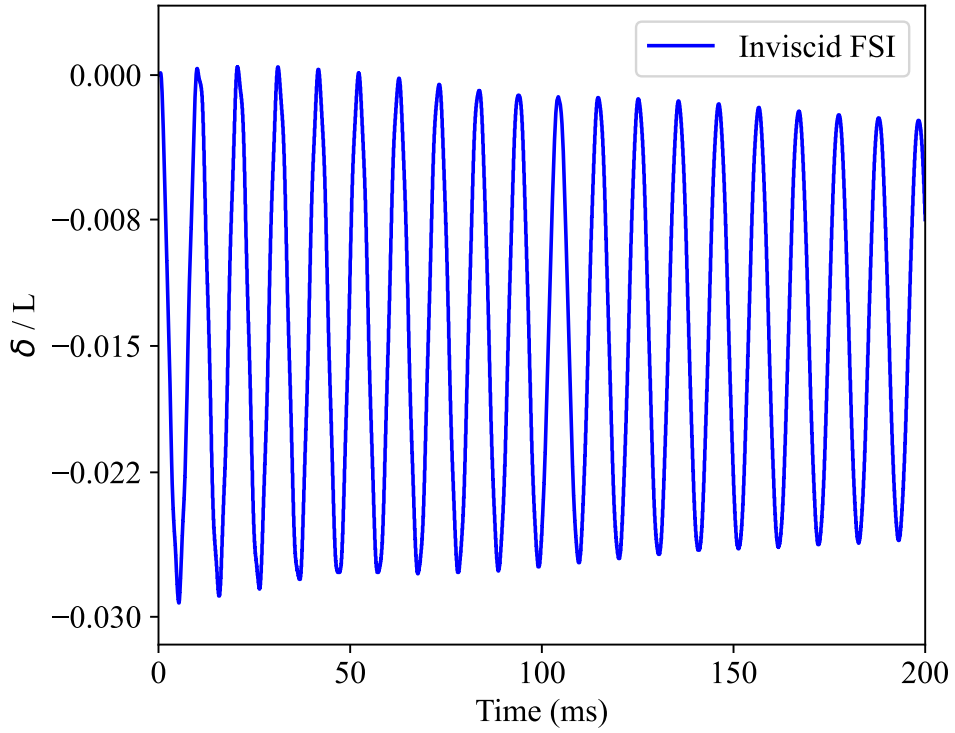Figure 5.5: FFT of Peak Pressure Evolution (Inviscid)
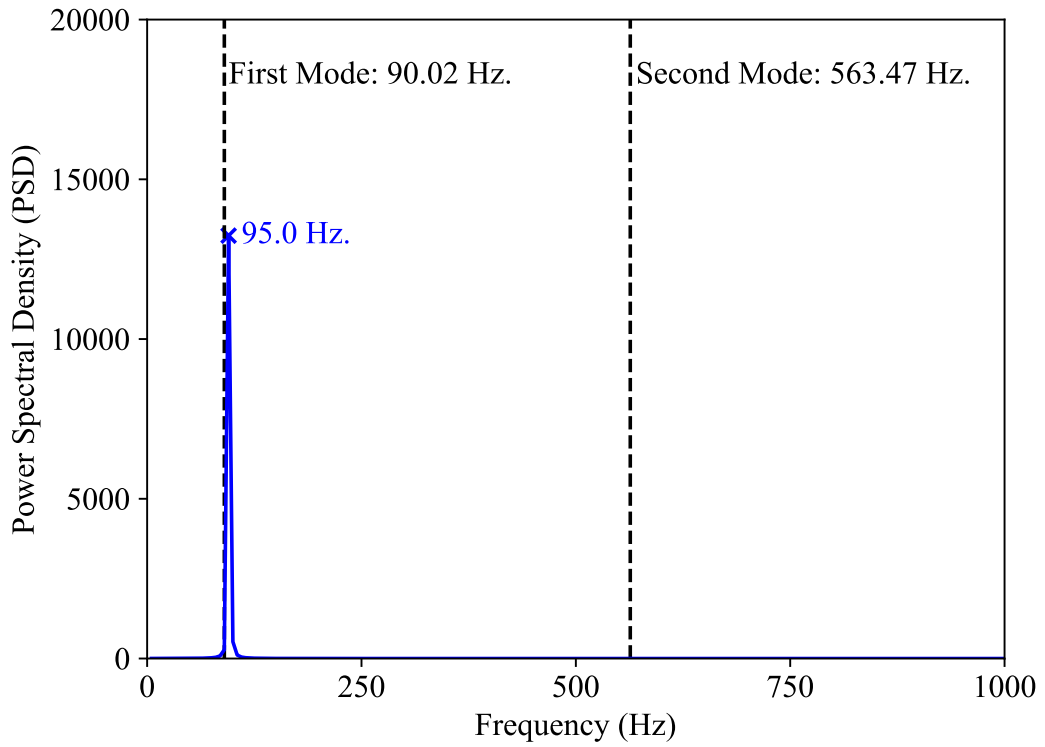
Figure 5.6: Trailing Edge Displacement (Inviscid; 200ms)



Figure 5.7: FFT of Trailing Edge Deflection with Time (Inviscid)

### 5.1.1.3 Viscous FSI

Figure 5.8 shows the time history of peak pressure result given by the two-way viscous FSI simulation. Two distinct modes can be clearly seen in the oscillation of peak pressure with time. Fast Fourier Transform (FFT) of peak pressure history shown in Figure 5.9 indicates that the first peak occurs around the plate's first mode, 11.08 % higher, and the second peak around the plate's second mode of deformation, 1.40 % higher.

The maximum displacement of the trailing edge of the plate is 3.96 mm with an oscillation frequency of 95.00 Hz. The oscillation frequency is 5.53 % higher than the natural frequency of the plate deformation. Thus the oscillation is dominated mainly by the natural frequency of the plate deformation.

Hence, the nature of the deformation of the plate must be similar to the first mode shape. This can evidently be seen in Figure 5.12 which plots the state of the plate in the first half cycle of the viscous simulation.
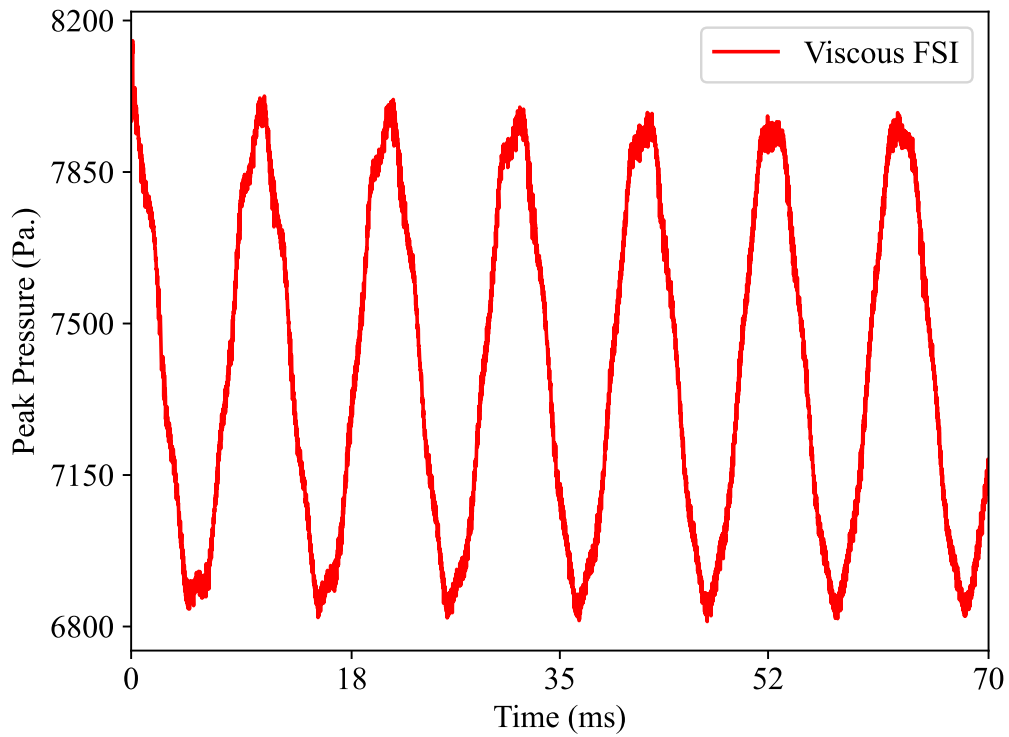
Figure 5.8: Peak Pressure Evolution with Time (Viscous)
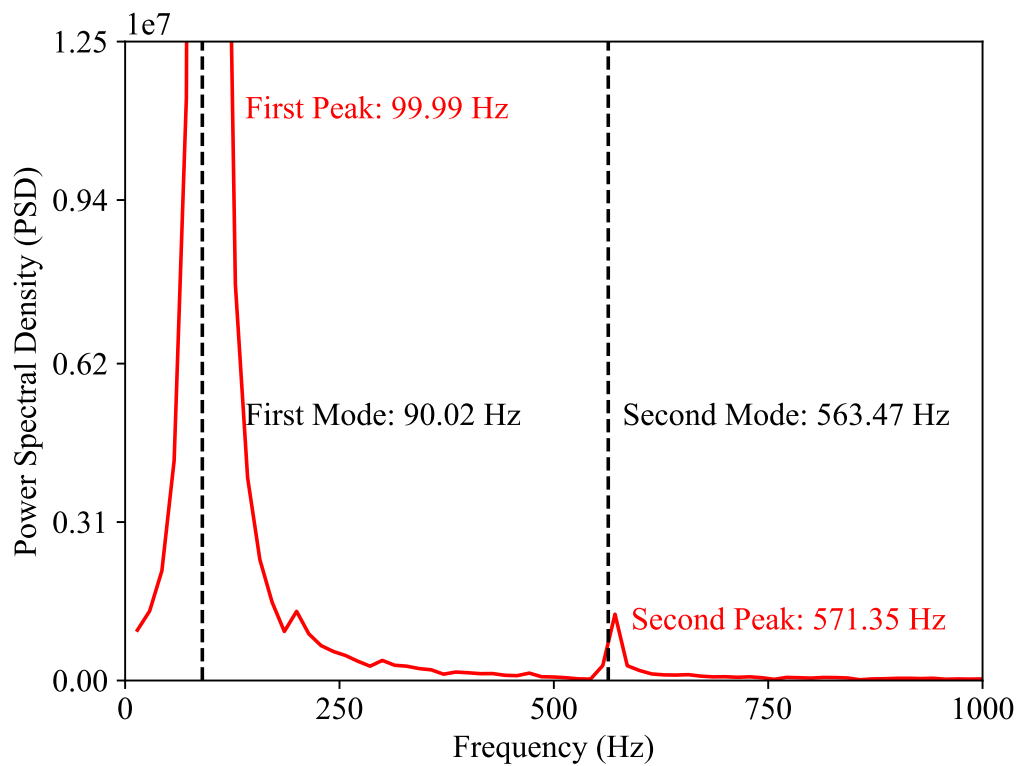


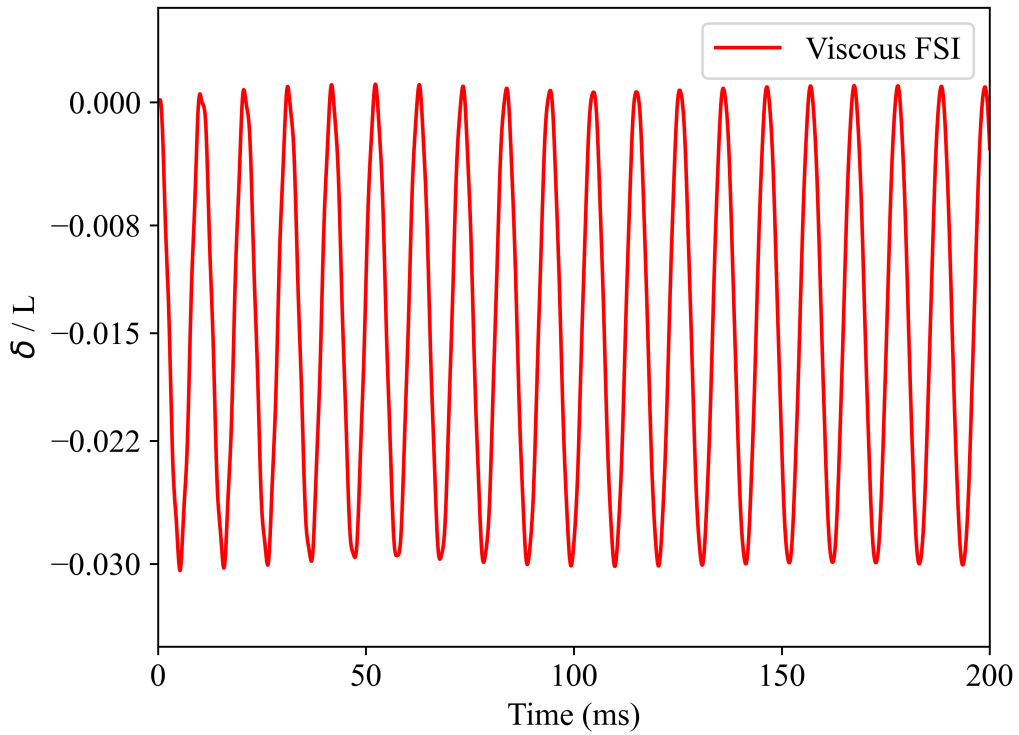Figure 5.9: FFT of Peak Pressure Evolution with Time (Viscous)

Figure 5.10: Trailing Edge Displacement (Viscous; 200ms)
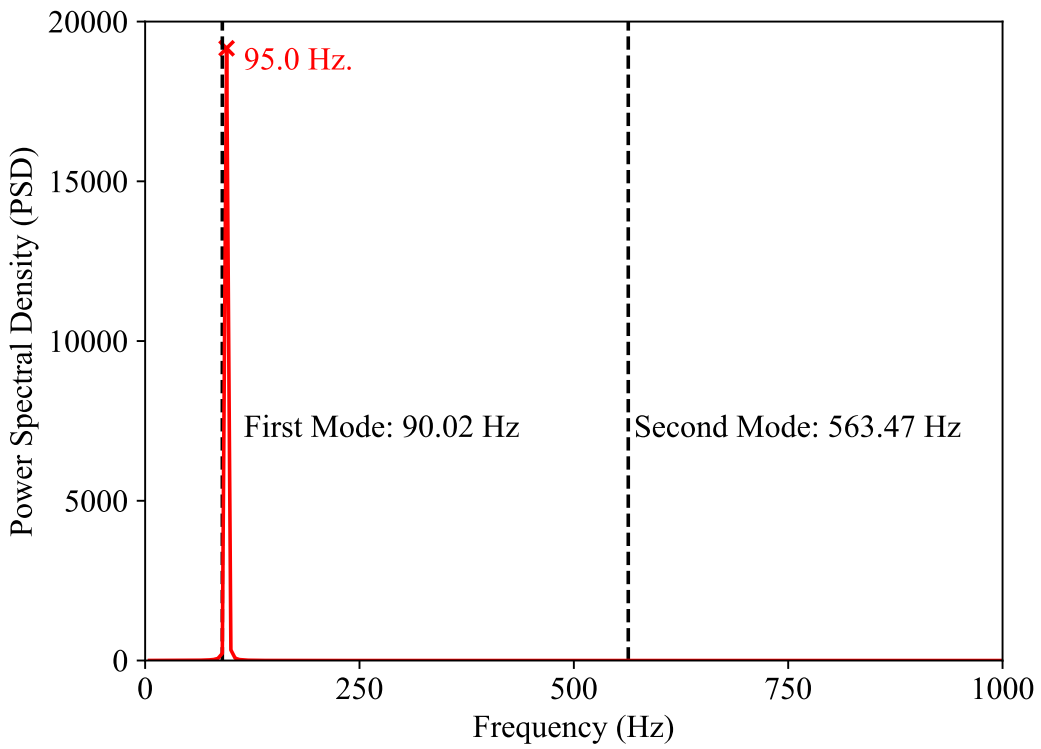


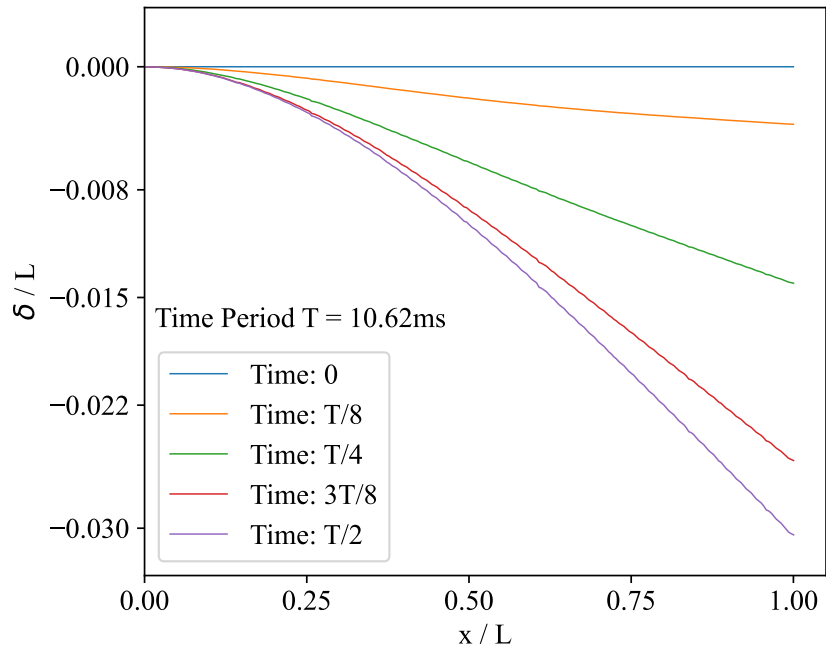Figure 5.11: FFT of Trailing Edge Deflection with Time (Viscous)

Figure 5.12: Plate State during First Half Cycle

**Transient Nature of Separation Bubble**
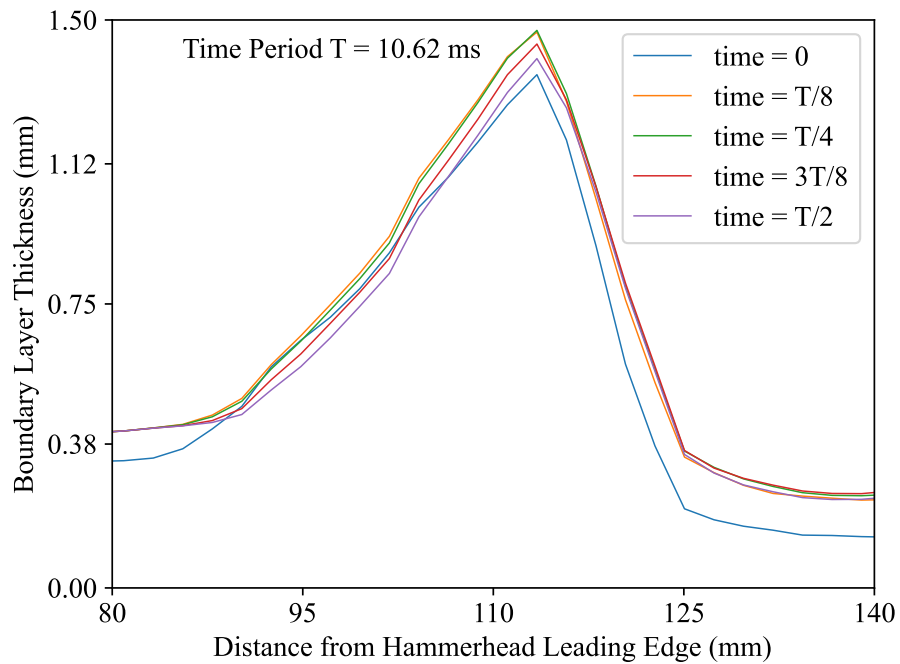


Figure 5.13: Change of Boundary Layer Thickness of Recirculation Region over Time

Further investigation into the SWBLI region in the viscous FSI result shows that the size of the separation bubble also changes with time during the oscillation of the plate. Figure 5.13 shows the time variation of the size of the recirculation region. This unsteady nature of the SWBLI region may also contribute to the changes in pressure over the plate and hence affect the plate's deflection.

#### 5.1.1.4 Comparison of Inviscid and Viscous FSI

The peak pressure predictions made by the inviscid and the viscous FSI are shown in Figure 5.14.



Figure 5.14: Peak Pressure Ratio against Local Deflection Angle (Inviscid and Viscous)

**SWBLI and Viscous Effects**

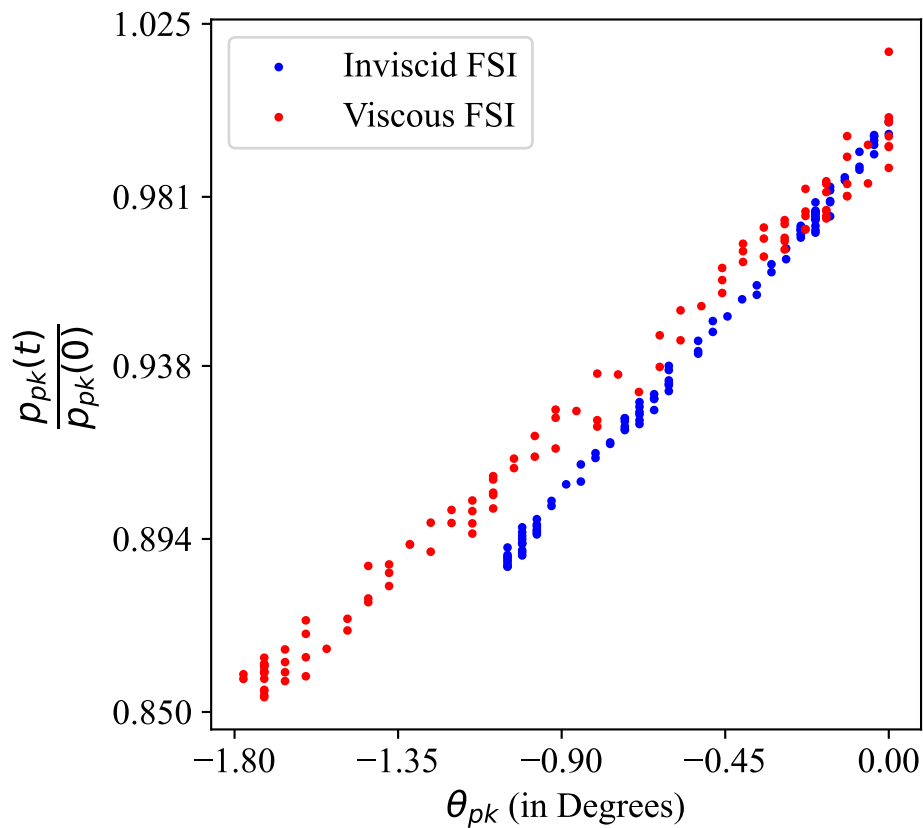The initial pressure distribution over the plate for both the inviscid and viscous cases is shown in Figure 5.15. The maximum peak pressure value increases by 4.13 % in the viscous CFD case when compared to the inviscid case. This difference can be attributed to the SWBLI phenomenon that occurs in viscous flows, leading edge shock and viscous boundary layer effects. As a result, the maximum trailing edge deflection predicted by viscous FSI is about 3.94 % higher than the value predicted by inviscid FSI, as shown in Table 5.1.
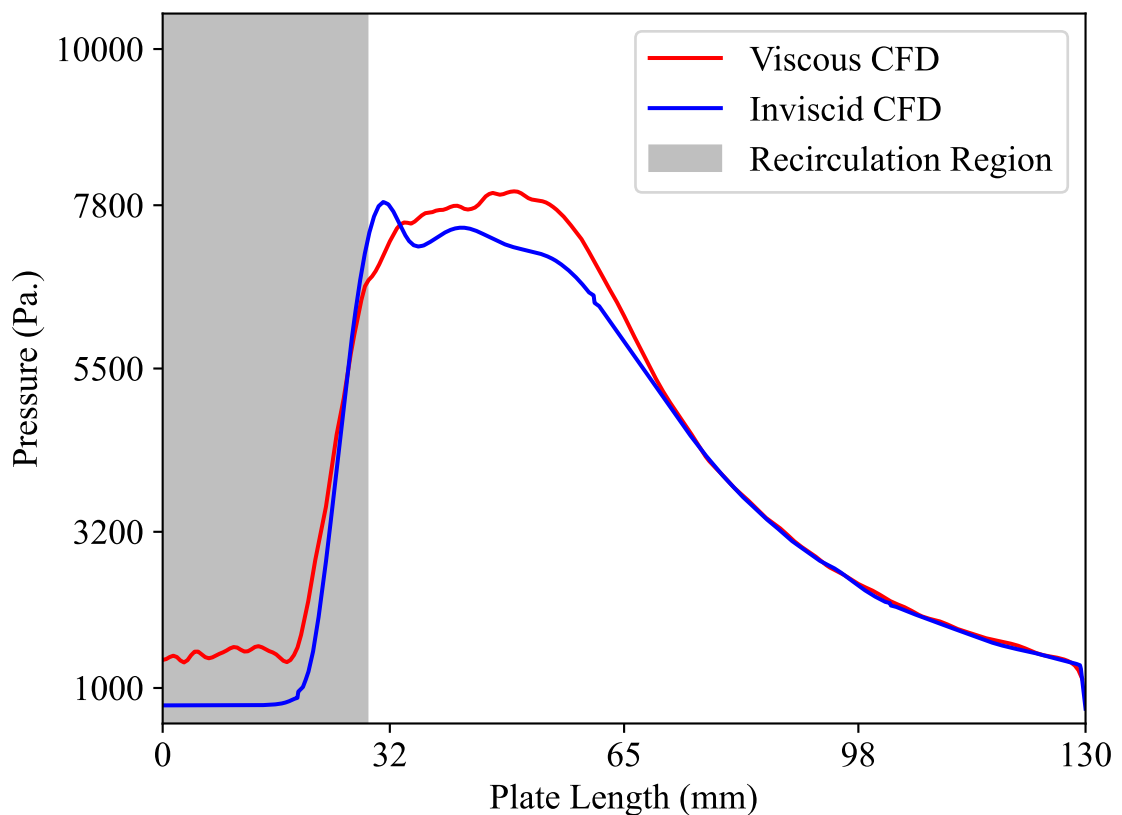


Figure 5.15: Initial Pressure Distribution (Inviscid and Viscous)

Table 5.1: Comparison of Invisid and Viscous FSI

| Model | Max. Peak Pressure (Pa.) | Min. Peak Pressure (Pa.) | Maximum Trailing Edge Deflection (mm) |
|---|---|---|---|
| Viscous FSI | 8,153.4 | 6,811.4 | -3.96 |
| Inviscid FSI | 7,830.2 | 6,951.4 | -3.8 |

### 5.1.2 Low Fidelity Modeling (LFM)

#### 5.1.2.1 Piston Theory

Figure 5.16 shows the evolution of peak pressure over the plate as predicted by the piston theory. As seen in Figure 5.17, the peak pressure value oscillates dominantly with the frequency of 96.0 Hz, which is close to the frequency of the first mode of the oscillation of the plate. However, another mode is also present with a frequency of 564.99 Hz, which is close to the second mode of oscillation of the plate.

The trailing edge displacement, non-dimensionalized with the length of the plate is plotted in Figure 5.18. The plate oscillation frequency is 95.0 Hz as seen in Figure 5.19, which is 11.76 % higher than the natural frequency (85.0 Hz). Thus the plate oscillates mainly following the first mode of deformation. The maximum deflection of the trailing edge is 3.41 mm.
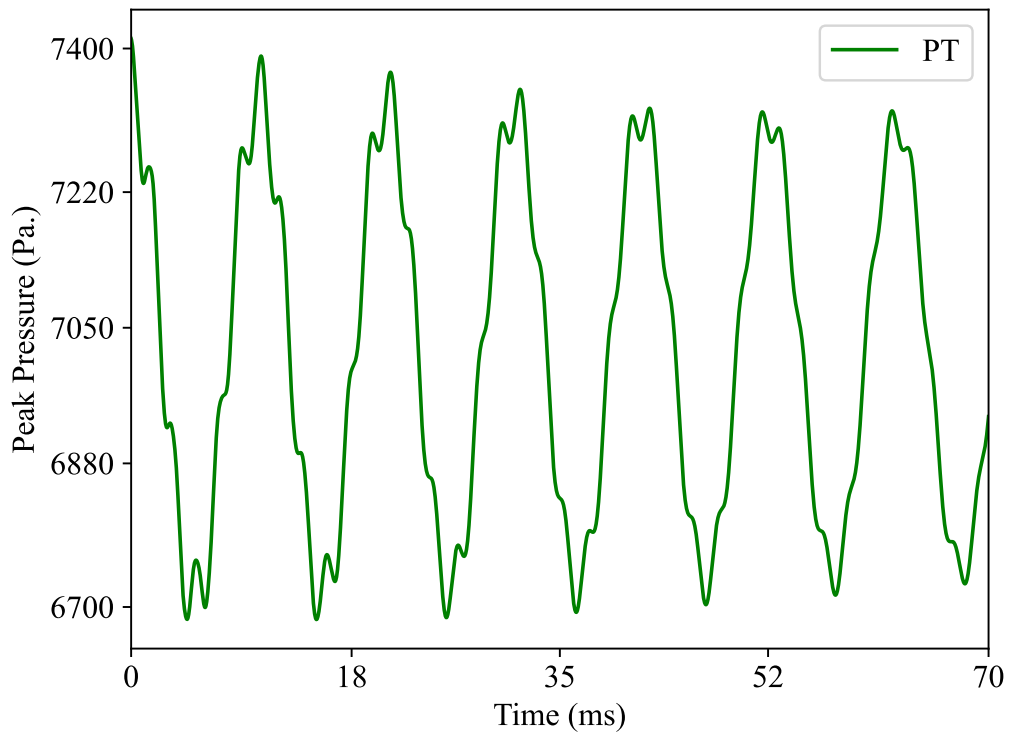
Figure 5.16: Peak Pressure Evolution with Time (PT)
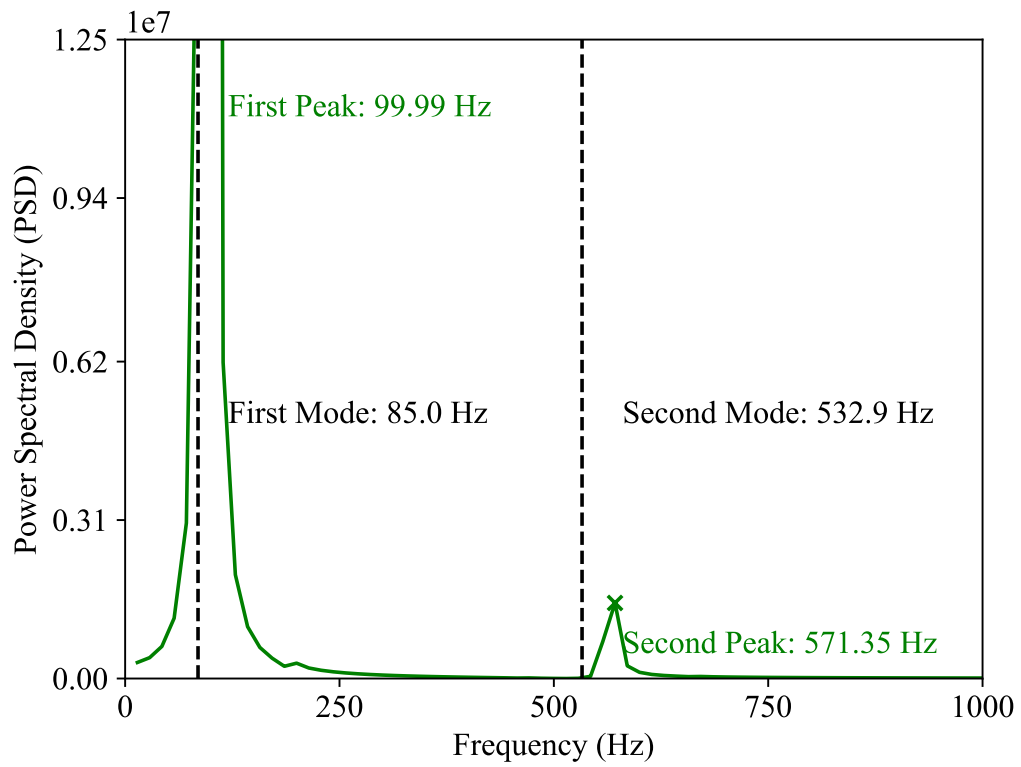


Figure 5.17: FFT of Peak Pressure Evolution (PT)
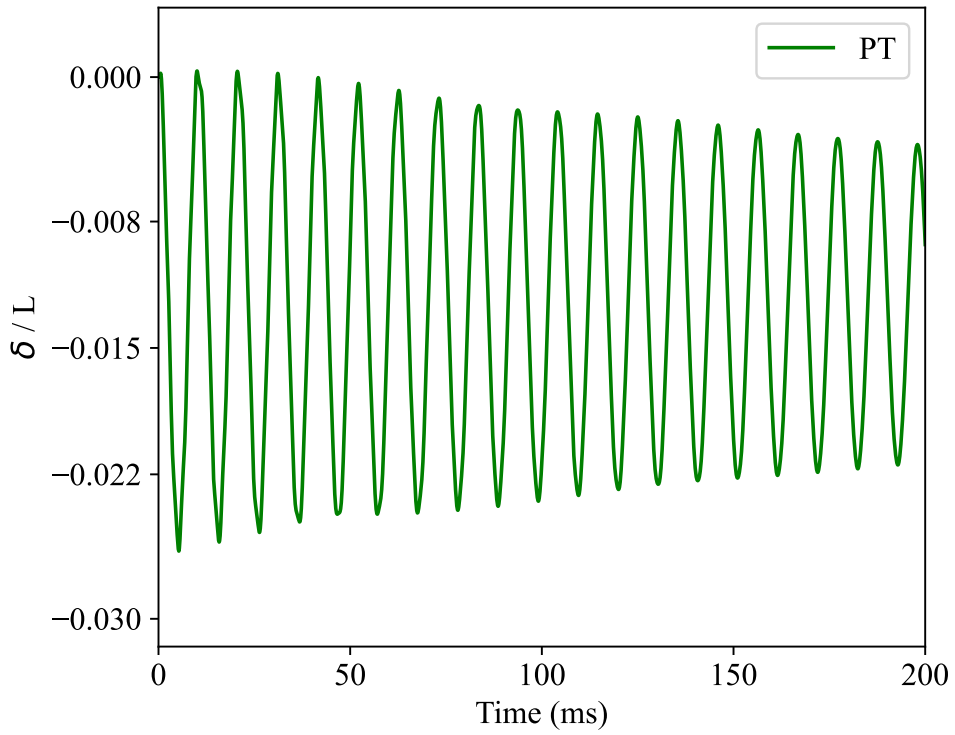
Figure 5.18: Trailing Edge Displacement (PT; 200 ms)
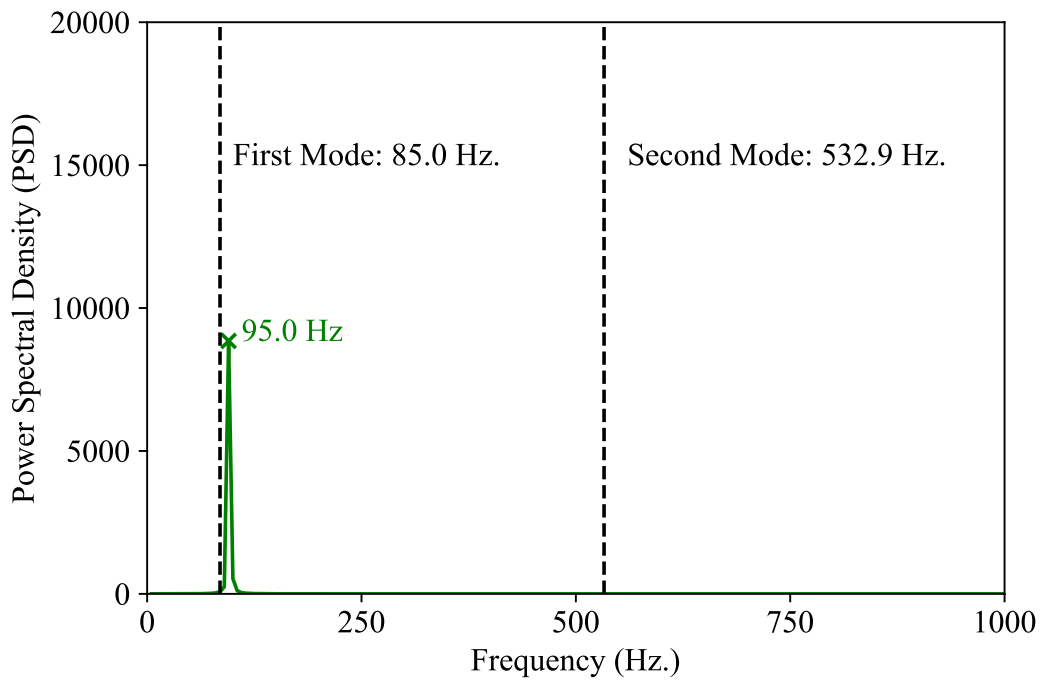


Figure 5.19: FFT of Trailing Edge Deflection (PT)

### 5.1.2.2 CFD-Enriched Piston Theory

Figure 5.20 shows the time history of peak pressure given by CFD Enriched Piston theory. Two distinct modes can be clearly seen in the oscillation of peak pressure with time. FFT of peak pressure history shown in Figure 5.21 indicates that the first peak occurs around the plate's first mode, 17.65 % higher and the second peak around the plate's second mode of deformation, 7.15 % higher.

The maximum displacement of the trailing edge of the plate is 3.69 mm with an oscillation frequency of 95.0 Hz. The oscillation frequency is 11.76 % higher than the natural frequency of the plate deformation. Thus the oscillation is dominated mainly by the natural frequency of the plate deformation.
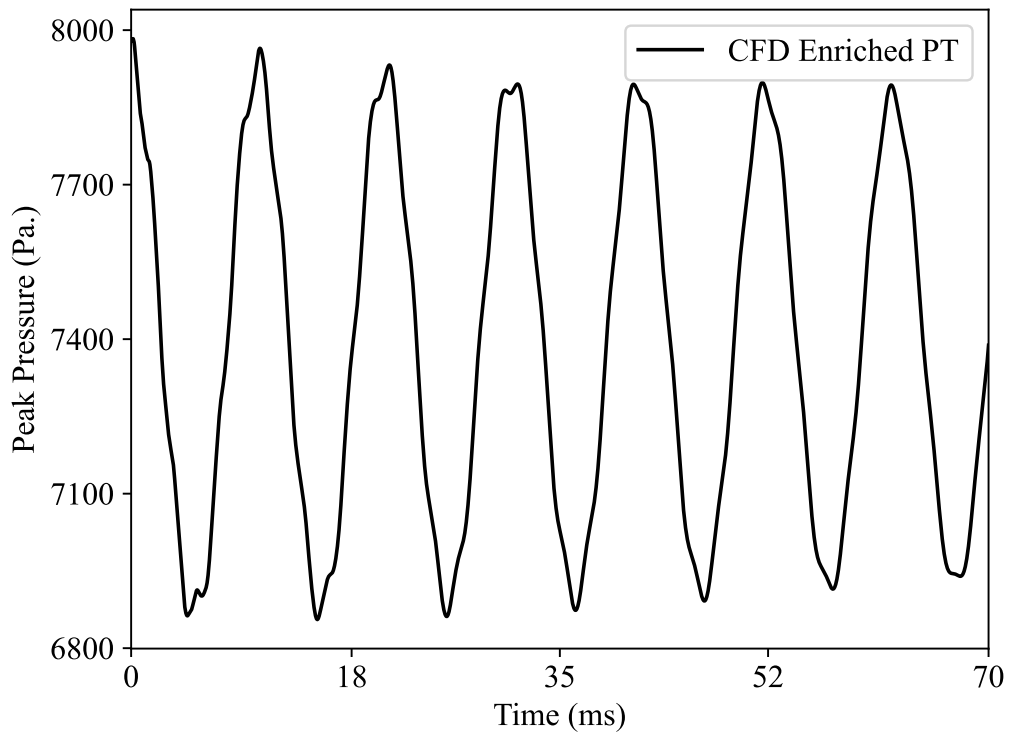
Figure 5.20: Peak Pressure Evolution with Time (CFD Enriched PT)
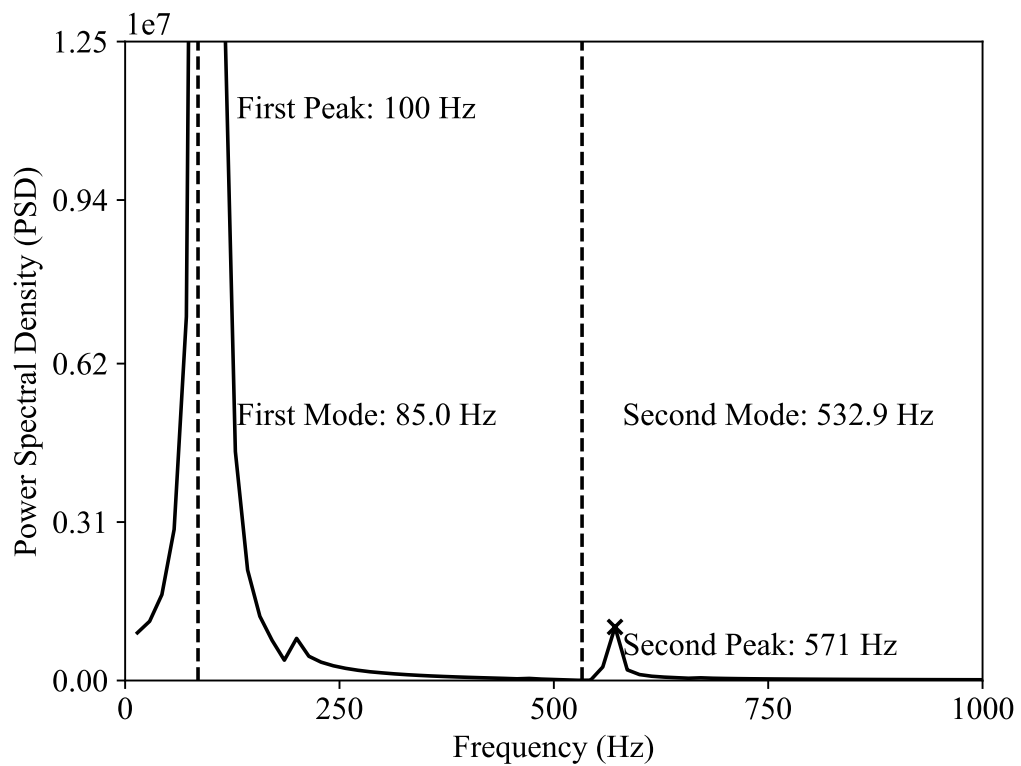


Figure 5.21: FFT of Peak Pressure Evolution (CFD Enriched PT)
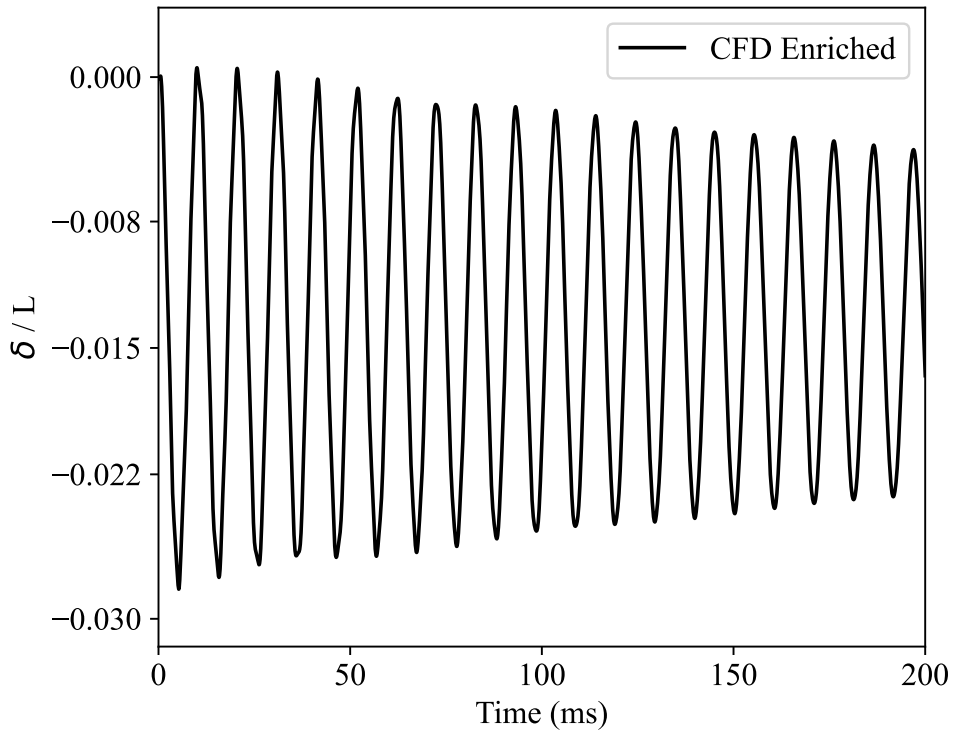
Figure 5.22: Trailing Edge Displacement (CFD Enriched PT; 200 ms)
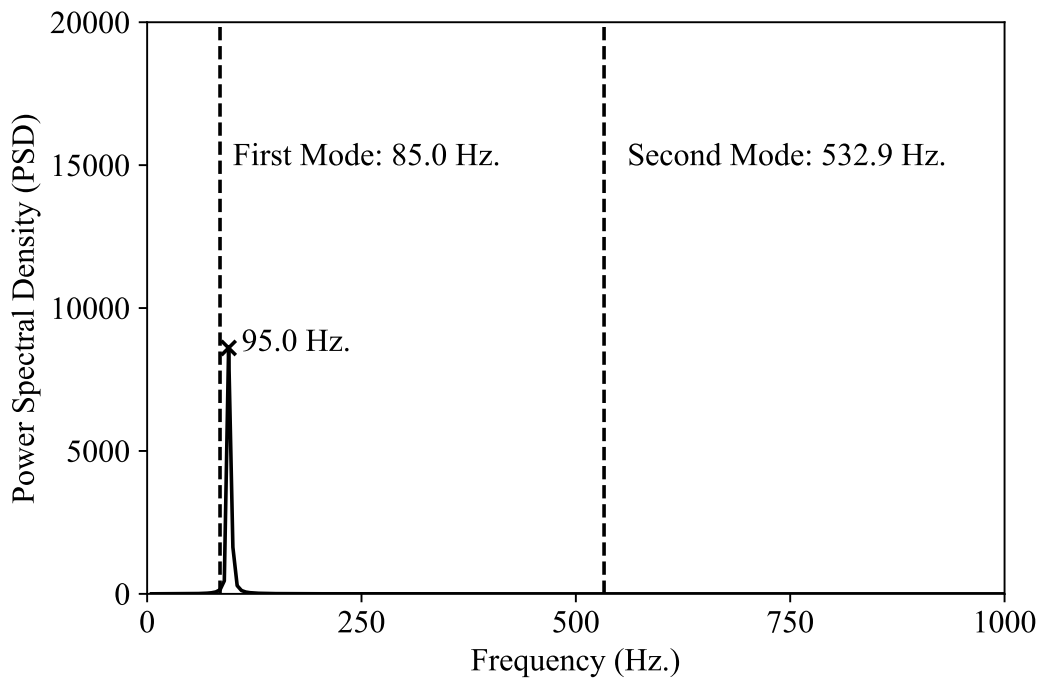


Figure 5.23: FFT of Trailing Edge Deflection (CFD Enriched PT)

### 5.1.2.3 Comparison of PT and CFD-Enriched PT

Figure 5.24 shows the predictions of the peak pressure against the local deflection angle made by both the PT and CFD Enriched PT.
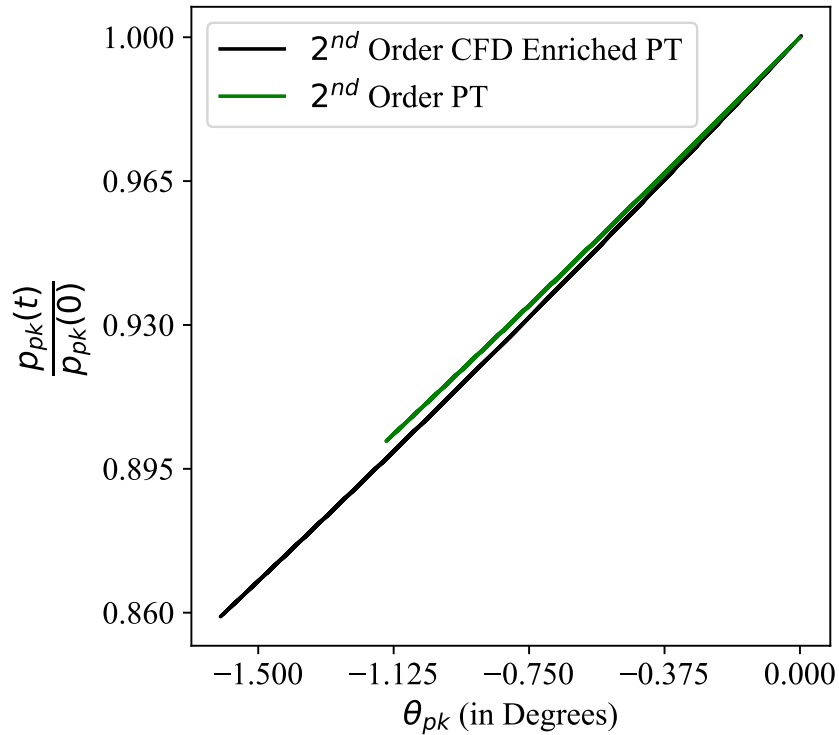


Figure 5.24: Peak Pressure Ratio against Local Deflection Angle (PT and CFD Enriched PT)

**Effect of SWBLI**

In Figure 5.25, the initial pressure distributions used for the low-fidelity modeling of the plate are plotted, and compared against Viscous CFD (which is also the input to the CFD Enriched PT Model). The pressure variation due to the phenomenon of SWBLI is also incorporated in the CFD Enriched PT as seen in the figure.

Tables 5.2 and 5.3 show that the maximum initial peak pressure value used in CFD Enriched PT is about 7.33% more than the analytical PT resulting in a 7.33% difference in the maximum trailing edge displacement as well.
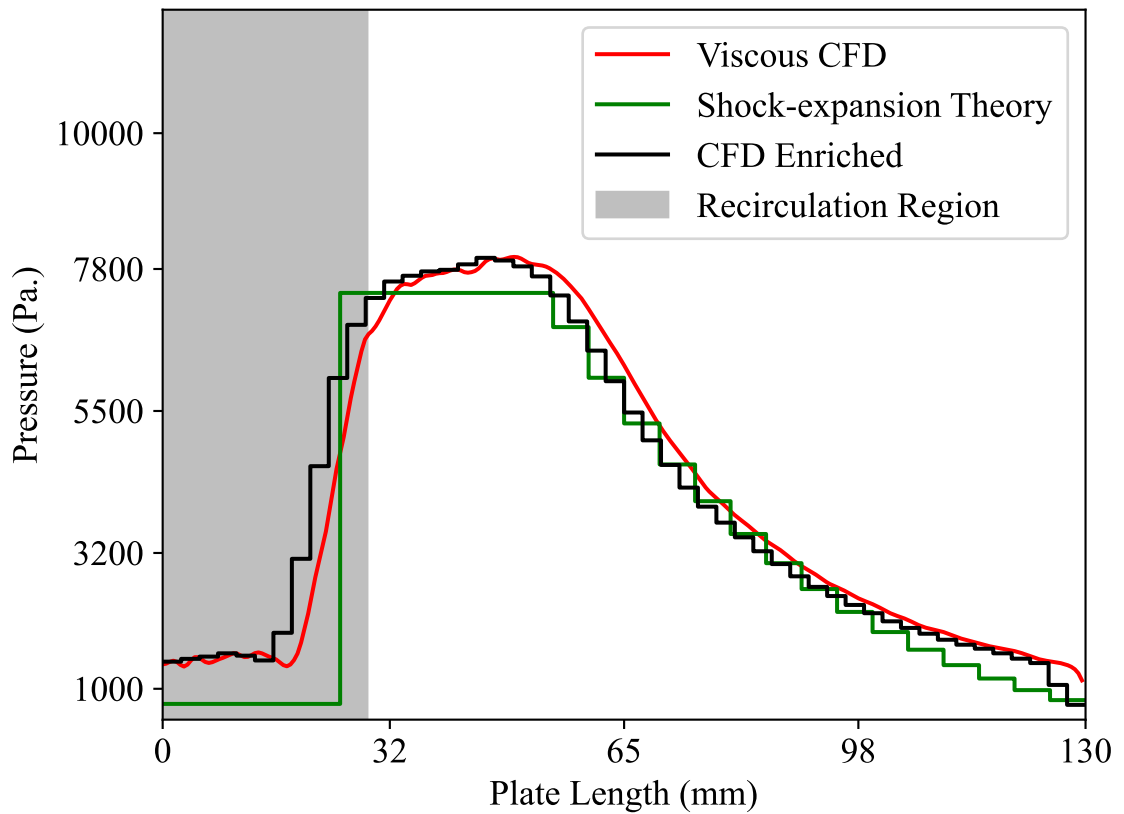
Figure 5.25: Initial Pressure Distribution (SE and CFD Enriched)

Table 5.2: Comparison of Pressure in PT and CFD-Enriched PT

| Model | Max. Peak Pressure (Pa.) | Min. Peak Pressure (Pa.) |
|---|---|---|
| PT | 7,412.32 | 6,684.27 |
| CFD Encirched PT | 7,983.41 | 6,855.59 |

Table 5.3: Comparison of Displacement in PT and CFD-Enriched PT

| Model | Maximum TE Deflection (mm) | Percent Difference from Viscous FSI |
|---|---|---|
| PT | -3.41 | -13.89% |
| CFD Encirched PT | -3.69 | -6.82% |

Also, from Table 5.3, it can be seen that the maximum trailing edge deflection predicted by CFD Enriched PT is only 6.82% less than that of viscous FSI. In comparison, the

deflection predicted by PT is about 13.89 % less than that of viscous FSI. This also shows that the SWBLI phenomenon has aeroelastic effects.

### 5.1.3  Comparison of HFM and LFM

#### 5.1.3.1  Quasi-steady Nature

The peak pressure approximation at different local plate deflection angles $\theta$ using low-fidelity CFD Enriched PT is evaluated against the high-fidelity viscous FSI.
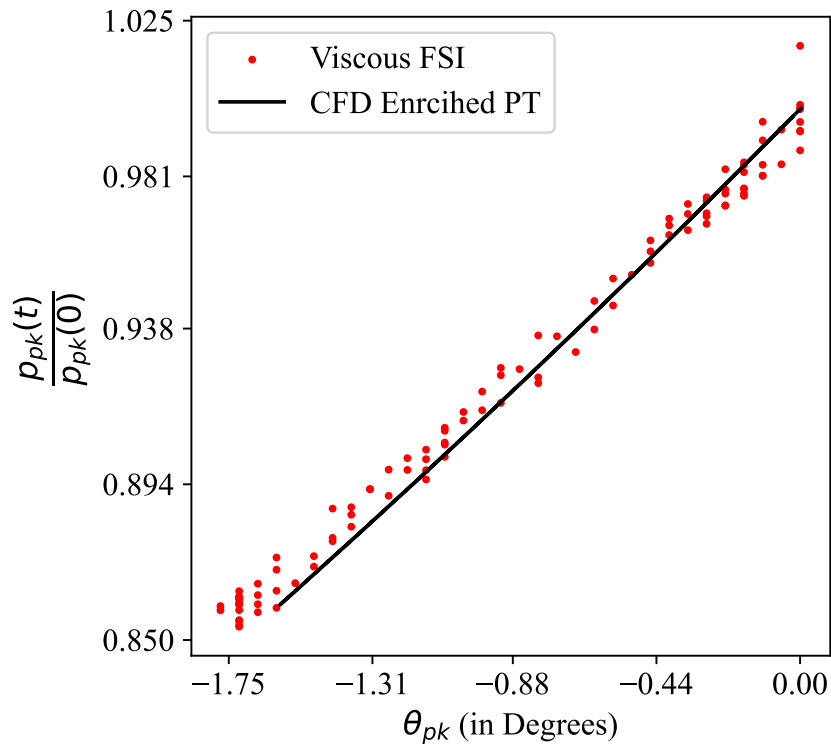


Figure 5.26:  Peak Pressure Ratio against Local Deflection Angle (Viscous Models/Initial Conditions)

In Figure 5.26, the quasi-steady nature of the problem is visualized, i.e. the pressure distribution over the plate is somewhat independent of the plate's deformation history, and is only a function of the current state of the plate.

The unsteady nature of the problem can also be quantified using reduced frequency.

Mathematically,

$$k = \frac{\omega L}{2U} \qquad (5.1)$$

The highest reduced frequency (k) in our domain (with $\omega = 628.32 rad/s$, $L = 130mm$, $U = U_{min} = 922.71m/s$) is 0.044. As k < 0.05, the problem can be considered quasi-steady [14], and hence the pressure distribution over the plate at any state can also be calculated with a steady simulation.

### 5.1.3.2 Effect of Transient Nature of SWBLI
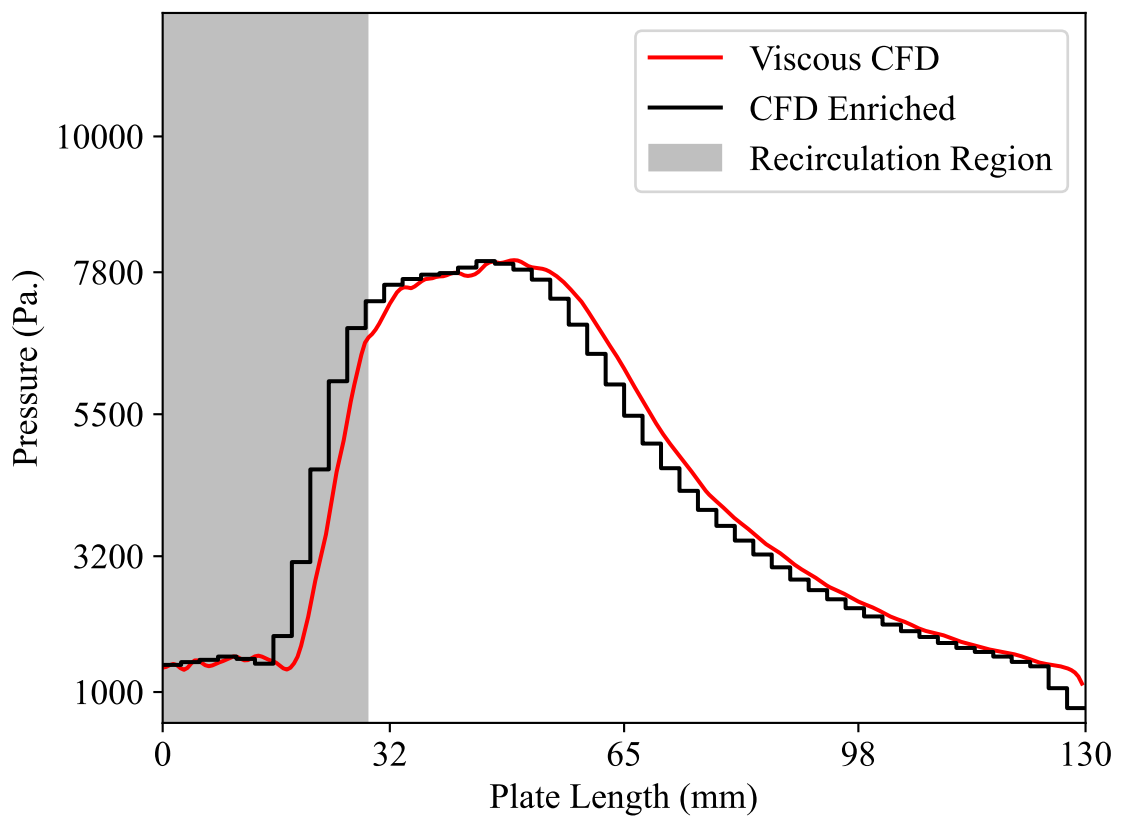


Figure 5.27: Initial Pressure Distribution (CFD Enriched PT and Viscous FSI)

Although CFD Enriched PT incorporates pressure distribution due to SWBLI in the initial condition, the unsteady nature of the SWBLI region is not accounted for during oscillations. From Table 5.3, it is evident that the CFD Enriched PT still has a significant difference with the result of the Viscous FSI.

This indicates that the unsteady nature of SWBLI also affects aeroelasticity. And hence further enhancements in the CFD Enriched PT method should be carried out to capture the transient nature of SWBLI too.

### 5.1.3.3    Damping Analysis
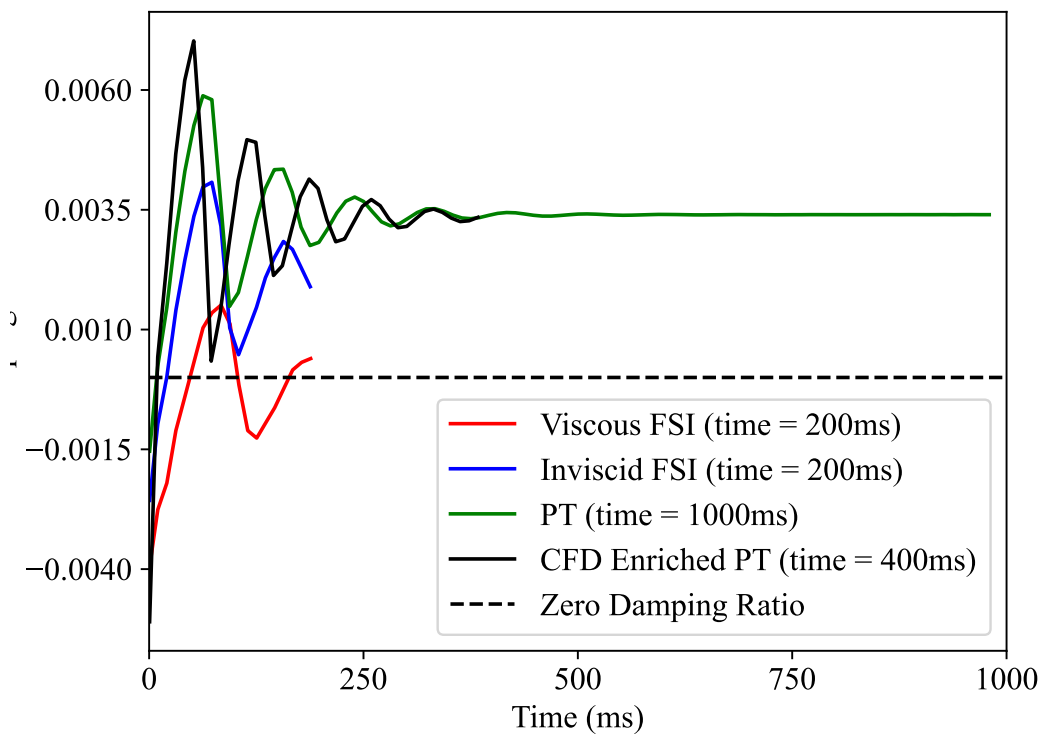


Figure 5.28: Comparision of Damping Ratio

The evolution of the damping ratio with each peak is compared for various models in Figure 5.28. As the value of trailing edge deflection increases in the first few oscillations in the PT, Inviscid FSI and Viscous FSI as shown in Figure 5.30, the damping ratios are negative for the first few peaks.

In the 1000ms data of the PT in Figure 5.28, the damping ratio, after a few oscillations, reaches a steady non-zero value of 0.0034, which suggests that oscillation does not reach the limit cycle. But, without further high-fidelity simulations, no inference can be drawn.

#### 5.1.3.4  Evaluation of CFD Enriched PT

Although the maximum trailing edge deflection predicted by the CFD Enriched PT differs by 7% from that predicted by the two-way viscous FSI simulation, CFD Enriched PT can be used as an effective tool for preliminary aeroelastic analysis because of its high computational efficiency as shown in Table 5.4.

Further enhancements in the CFD Enriched PT method should be carried out to capture the transient nature of SWBLI.

Table 5.4: Comparison of CFD Enriched PT with HFM

| Model | Maximum TE Deflection (mm) | Computation Time (200 ms of flow duration) |
|---|---|---|
| CFD Enriched PT | -3.69 | 4 hours |
| Inviscid FSI | -3.8 | 24 hours |
| Viscous FSI | -3.96 | 480 hours |

### 5.1.4  Summary

#### 5.1.4.1  Pressure-Based Analysis

Figure 5.29 shows the time history of peak pressure results given by all low and high-fidelity models used in this study. All the results of peak pressure history show almost the same frequency and time period of oscillation. Two distinct modes can be clearly seen in the oscillations of peak pressure with time. Higher mode effects are also found in the Inviscid and the Viscous FSI simulation results.
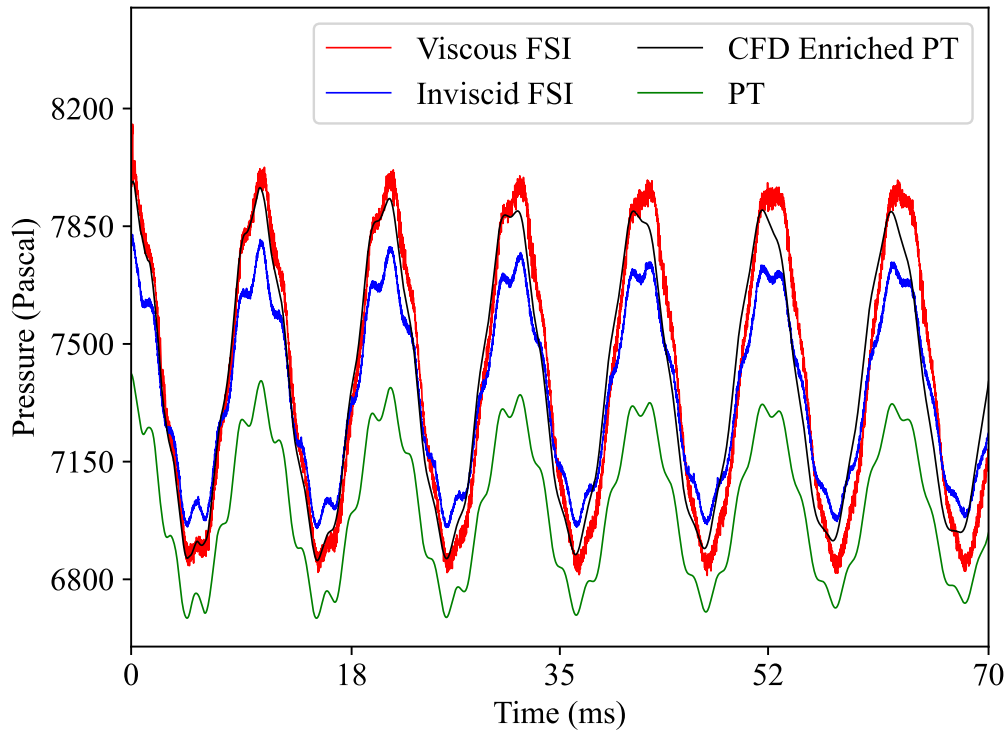
Figure 5.29: Peak Pressure Over Time (70 ms)

### 5.1.4.2 Displacement Analysis

In the experiment, the plate oscillation is affected by three factors: freestream pressure changes, the initial impulse of the flow, and the local pressure changes due to fluid-structure coupling and SWBLI [41]. However, no freestream pressure changes have been modeled in this simulation.

Figure 5.30 shows the trailing edge displacement history predicted by different low and high-fidelity methods used. This result is consistent with the peak pressure distribution shown in Figure 5.29 which shows that the plate oscillation is dominated by local pressure changes over the plate due to shock impingement, shock reflection, shock-expansion interaction, and SWBLI. Also, the frequency of oscillation remains the same in all methods while there is a variance in amplitude.
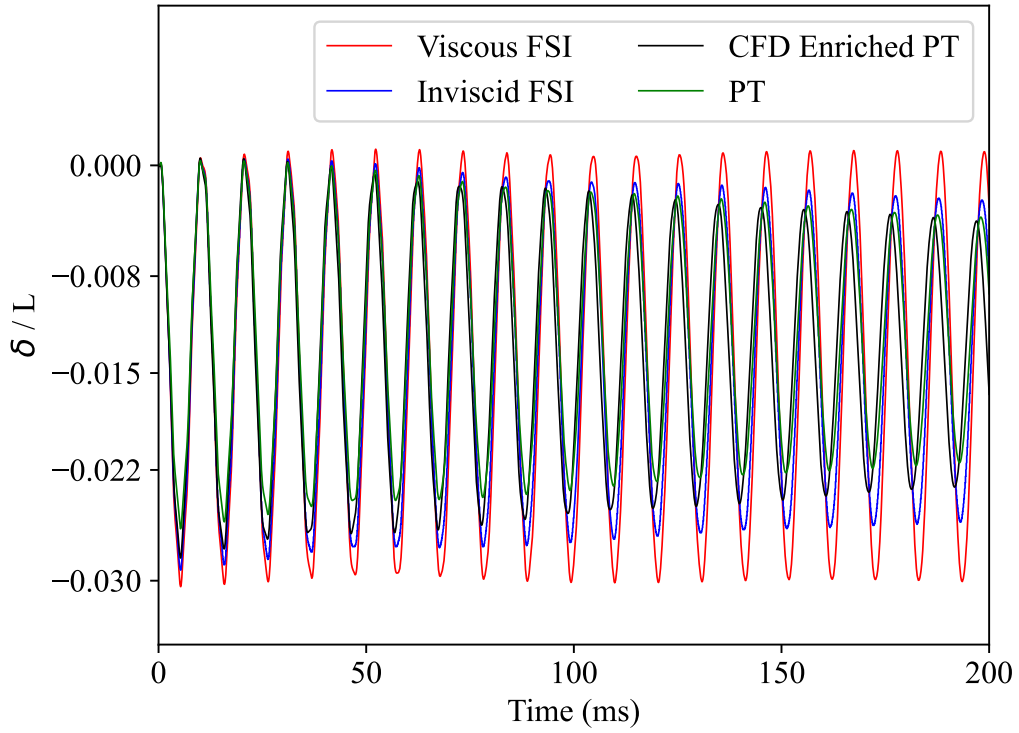
Figure 5.30: Trailing Edge Displacement History (time = 200 ms)

Table 5.5: Comparison of TE Displacement of Different Aeroelastic Prediction Models Used

| Model | Maximum TE Deflection | Percent Difference from Viscous FSI Results | Computation Time for 200ms |
|---|---|---|---|
| PT | -3.41 mm | -13.89% | 10 min |
| CFD Enriched PT | -3.69 mm | -6.82% | 4 hours |
| Inviscid FSI | -3.8 mm | -4.04% | 24 hours |
| Viscous FSI | -3.96 mm | 0% | 480 hours |

## 5.2 Limitations

- Thermal interactions are not considered in this study.

- The three-dimensional effects could not be captured as only the two-dimensional model is simulated.

- The flow transition from laminar to turbulent is not studied.

## 5.3 Problems Faced

- Initially, frequent solver crashes were encountered in fluid simulation in the form of negative initial temperature in rhoCentralFoam. This error was caused due to numerical oscillations of energy variables around very low values. This problem was solved by using high-quality mesh and fine-tuning the finite volume schemes.

- Experimental data of the HyMAX experiment has not yet been released. Hence, validation of the results could not be done.

## 5.4 Budget Analysis

The computational cost is calculated using the Amazon Web Services charge for 16 cores of CPU, 32 GB RAM, and 950 GB of storage, which comes to around 0.6114 USD (Rs. 80.24 as of the writing of this report) per hour. The computational time to run the final simulation, after all testing is completed, is taken into account. The total computational cost is shown in Table 5.6. Also, the total estimated budget for the project including the documentation cost is shown in Table 5.7.

Table 5.6: Computation Cost of Different Simulations

| Simulation Type | Time (hours) | Approximate Cost (Rs.) |
| --- | --- | --- |
| Explicit Inviscid | 24 | 2,000.00 |
| Implicit Inviscid | 130 | 12,000.00 |
| Explicit Viscous | 480 | 40,000.00 |

Table 5.7: Budget Estimation

| S.N. | Name of Particulars | Cost (Rs.) |
|------|---------------------|------------|
| 1. | Documentation | 6,000.00 |
| 2. | Computational Cost | 54,000.00 |
| | Total | 60,000.00 |

.

# CHAPTER SIX: CONCLUSION AND FUTURE ENHANCE-MENT

## 6.1   Conclusion

This study aimed to make aeroelastic predictions of a cantilevered plate with hypersonic shock impingement. Low-fidelity modeling using piston theory and high-fidelity modeling using a two-way partitioned FSI approach were used for predictions and results were compared. The major conclusion from this study are summarized below;

- SWBLI phenomenon, leading edge shock wave, and other viscous effects affect the pressure distribution over the plate as the peak pressure value increases by around 4% (300 Pa) in viscous CFD result when compared to inviscid CFD result. As a result, the maximum trailing edge deflection predicted by viscous FSI is about 4% higher than the value predicted by inviscid FSI.

- SE-based PT was validated against the HyFoil experimental data with about 6% error in terms of trailing edge displacement and 0.7% in terms of oscillation frequency. Thus, SE-based piston theory can be used to make aeroelastic predictions for problems without shock impingement and SWBLI.

- In the case of shock impingement (HyMAX), the initial peak pressure value predicted by PT is around 9% (700 Pa) less than that of steady viscous CFD. As a result, trailing edge deflection predicted by PT is about 14% less compared to that predicted by two-way viscous FSI simulation.

- CFD Enriched PT was found to make a better prediction than PT as the TE displacement predicted is only about 7% less than that predicted by viscous FSI.

- The computation time of CFD Enriched PT (4 hours) is much less compared to that of Inviscid FSI (24 hours) and Viscous FSI (480 hours). And hence can be used for preliminary aeroelastic analysis.

## 6.2   Scope for Future Enhancement

This study presented a numerical study of hypersonic FSI on a cantilevered plate with shock impingement using both low and high-fidelity modeling approaches. There is still a lot of scope for future studies.

- With a limited amount of data currently available (both experimental and numerical), similar numerical and experimental studies with different plate configurations and oscillating shock-generator could generate valuable data for future aeroelastic predictions.

- Transient two-way FSI simulation was done for both inviscid and viscous laminar flow. However, the hypersonic flow is bound to undergo transition at any stage in cases of shock impingement and SWBLI. Thus, future study is recommended on turbulent FSI simulation and comparison of its result with laminar as well as the experimental data.

- Similar configuration in this study with higher wall temperature will exhibit high thermal interactions. Experimental and numerical studies with both low-fidelity approximations and coupled FTSI simulation could be adopted by future researchers.

- A detailed study can be done to numerically reinforce PT to account for the pressure fluctuation due to viscous effects.

# REFERENCES

[1] Y. Bazilevs, K. Takizawa, and T. E. Tezduyar, *Computational fluid-structure interaction: methods and applications.* John Wiley & Sons, 2013.

[2] D. de Rosa, G. Pezzella, R. S. Donelli, and A. Viviani, "Flap effectiveness appraisal for winged re-entry vehicles," *Acta Astronautica*, vol. 122, pp. 175–184, 2016.

[3] E. H. Hirschel and C. Weiland, *Selected aerothermodynamic design problems of hypersonic flight vehicles.* Springer Science & Business Media, 2009, vol. 229.

[4] S. Bhattrai, "Experimental and numerical study of hypersonic aeroelastic intakes," Ph.D. dissertation, UNSW Sydney, 2021.

[5] Y. Krishna, S. O'Byrne, S. Wittig, and J. J. Kurtz, "Numerically determining mach number and orientation in hypersonic inlets using absorption spectroscopy," *Journal of Propulsion and Power*, vol. 31, no. 1, pp. 123–132, 2015.

[6] R. Ohayon and H. Morand, "Mechanical and numerical modelling of fluid-structure vibration instabilities of liquid propelled launch vehicle," *Chaos, Solitons & Fractals*, vol. 5, no. 9, pp. 1705–1724, 1995.

[7] B. Thuruthimattam, P. Friedmann, K. Powell, and J. McNamara, "Aeroelasticity of a generic hypersonic vehicle," in *43rd AIAA/ASME/ASCE/AHS/ASC Structures, Structural Dynamics, and Materials Conference*, 2002, p. 1209.

[8] G. Hou, J. Wang, and A. Layton, "Numerical methods for fluid-structure interaction—a review," *Communications in Computational Physics*, vol. 12, no. 2, pp. 337–377, 2012.

[9] J. D. Anderson, *Hypersonic and high temperature gas dynamics.* Aiaa, 2000.

[10] R. Neumann, "Special topics in hypersonic flow, aerodynamic problems of hypersonic vehicle, ls-42-vol. 1, agard, july 1972, pp. 7-1-7-64."

[11] "X-51A Waverider — af.mil," https://www.af.mil/About-Us/Fact-Sheets/Display/Article/104467/x-51a-waverider/, [Accessed 23-Feb-2023].

[12] H. Babinsky and J. K. Harvey, *Shock wave-boundary-layer interactions.* Cambridge University Press, 2011, vol. 32.

[13] M. S. Holden, "Shock wave-turbulent boundary layer interaction in hypersonic flow," in *10th Aerospace Sciences Meeting*, 1977, p. 74.

[14] G. Currao, "Experimental study of hypersonic fluid structure interaction with shock impingement on a cantilevered plate," Ph.D. dissertation, UNSW Sydney, 2018.

[15] J. J. McNamara and P. P. Friedmann, "Aeroelastic and aerothermoelastic analysis in hypersonic flow: past, present, and future," *AIAA journal*, vol. 49, no. 6, pp. 1089–1122, 2011.

[16] J. J. McNamara, A. R. Crowell, P. P. Friedmann, B. Glaz, and A. Gogulapati, "Approximate modeling of unsteady aerodynamics for hypersonic aeroelasticity," *Journal of Aircraft*, vol. 47, no. 6, pp. 1932–1945, 2010.

[17] G. M. Currao, A. J. Neely, C. M. Kennell, S. L. Gai, and D. R. Buttsworth, "Hypersonic fluid–structure interaction on a cantilevered plate with shock impingement," *AIAA journal*, 2019.

[18] J. Donea, S. Giuliani, and J.-P. Halleux, "An arbitrary lagrangian-eulerian finite element method for transient dynamic fluid-structure interactions," *Computer methods in applied mechanics and engineering*, vol. 33, no. 1-3, pp. 689–723, 1982.

[19] C. Farhat and T. Lin, "Transient aeroelastic computations using multiple moving frames of reference," in *Flight Simulation Technologies Conference and Exhibit*, 1990, p. 3053.

[20] T. E. Tezduyar, M. Behr, S. Mittal, and J. Liou, "A new strategy for finite element computations involving moving boundaries and interfaces—the deforming-spatial-domain/space-time procedure: Ii. computation of free-surface flows, two-liquid flows, and flows with drifting cylinders," *Computer methods in applied mechanics and engineering*, vol. 94, no. 3, pp. 353–371, 1992.

[21] C. Michler, S. Hulshoff, E. Van Brummelen, and R. De Borst, "A monolithic approach to fluid–structure interaction," *Computers & fluids*, vol. 33, no. 5-6, pp. 839–848, 2004.

[22] W. A. Wall, S. Genkinger, and E. Ramm, "A strong coupling partitioned approach for fluid–structure interaction with free surfaces," *Computers & Fluids*, vol. 36, no. 1, pp. 169–183, 2007.

[23] R. Lohner, J. Cebral, C. Yang, J. D. Baum, E. Mestreau, C. Charman, and D. Pelessone, "Large-scale fluid-structure interaction simulations," *Computing in Science & Engineering*, vol. 6, no. 3, pp. 27–37, 2004.

[24] C. S. Peskin, "The immersed boundary method," *Acta numerica*, vol. 11, pp. 479–517, 2002.

[25] W.-X. Huang and F.-B. Tian, "Recent trends and progress in the immersed boundary method," *Proceedings of the Institution of Mechanical Engineers, Part C: Journal of Mechanical Engineering Science*, vol. 233, no. 23-24, pp. 7617–7636, 2019.

[26] R. Bisplinghoff and J. Dugundji, "Influence of aerodynamic heating on aeroelastic phenomena," *High Temperature Effects in Aircraft Structures, Agardograph No. 28, Edited by NJ Hoff*, pp. 288–312, 1958.

[27] P. P. Friedmann, "Renaissance of aeroelasticity and its future," *Journal of aircraft*, vol. 36, no. 1, pp. 105–121, 1999.

[28] C. SPAIN, T. ZEILER, M. GIBBONS, D. SOISTMANN, P. Pozefsky, R. DEJESUS, and C. BRANNON, "Aeroelastic character of a national aerospace plane demostrator concept," in *34th Structures, Structural Dynamics and Materials Conference*, 1993, p. 1314.

[29] C. McClinton, "X-43-scramjet power breaks the hypersonic barrier: Dryden lectureship in research for 2006," in *44th AIAA aerospace sciences meeting and exhibit*, 2006, p. 1.

[30] T. Neuenhahn, H. Olivier, and A. Paull, "Development of the hyshot stabiltiy demonstrator," in *25th AIAA Aerodynamic Measurement Technology and Ground Testing Conference*, 2006, p. 2960.

[31] N. Mansour, J. Pittman, and L. Olson, "Fundamental aeronautics hypersonics project: Overview," in *39th AIAA Thermophysics Conference*, 2007, p. 4263.

[32] S. Walker and F. Rodgers, "Falcon hypersonic technology overview," in *AIAA/CIRA 13th International Space Planes and Hypersonics Systems and Technologies Conference*, 2005, p. 3253.

[33] J. Hank, J. Murphy, and R. Mutzman, "The x-51a scramjet engine flight demonstration program," in *15th AIAA international space planes and hypersonic systems and technologies conference*, 2008, p. 2540.

[34] D. Dolvin, "Hypersonic international flight research and experimentation (hifire) fundamental science and technology development strategy," in *15th AIAA international space planes and hypersonic systems and technologies conference*, 2008, p. 2581.

[35] K. Gupta, L. Voelker, C. Bach, T. Doyle, and E. Hahn, "Cfd-based aeroelastic analysis of the x-43 hypersonic flight vehicle," in *39th Aerospace Sciences Meeting and Exhibit*, 2001, p. 712.

[36] K. Gupta and L. Voelker, "Aeroelastic simulation of hypersonic flight vehicles," *AIAA journal*, vol. 50, no. 3, pp. 717–723, 2012.

[37] L. P. McQuellin, A. Neely, and G. Currao, "Considerations for a hypersonic flight test investigating fluid-thermal-structural interactions," in *23rd AIAA International Space Planes and Hypersonic Systems and Technologies Conference*, 2020.

[38] S. Bhattrai, L. McQuellin, G. M. Currao, A. Neely, and D. Buttsworth, "Influence of hypersonic fluid-structure interaction on the control authority of a trailing-edge flap," in *22nd AIAA International Space Planes and Hypersonics Systems and Technologies Conference*, 2018, p. 5265.

[39] G. M. Currao, A. J. Neely, D. R. Buttsworth, and S. L. Gai, "Hypersonic fluid-structure interaction on a cantilevered plate," in *7th European Conference for Aeronautics and Space Sciences*, vol. 12, 2017, p. 13.

[40] P. B. Vasconcelos, L. P. McQuellin, T. Krishna, and A. Neely, "Experimental study of hypersonic fluid-structure interactions on an inclined clamped-free-clamped-free compliant panel," in *ASCEND 2021*, 2021, p. 4232.

[41] P. B. Vasconcelos, L. McQuellin, K. Talluru, and A. Neely, "Hypersonic fluid-structure interactions on a compliant clamped-free-clamped-free panel under the influence of static shock impingement," in *AIAA SCITECH 2022 Forum*, 2022, p. 0241.

[42] K. Talluru, L. McQuellin, and A. Neely, "Data package for hymax."

[43] J. Anderson, *Fundamentals of Aerodynamics (SI units)*. McGraw Hill, 2011.

[44] H. Ashley and G. Zartarian, "Piston theory-a new aerodynamic tool for the aeroelastician," *Journal of the aeronautical sciences*, vol. 23, no. 12, pp. 1109–1118, 1956.

[45] M. Oppenheimer and D. Doman, "A hypersonic vehicle model developed with piston theory," in *AIAA atmospheric flight mechanics conference and exhibit*, 2006, p. 6637.

[46] W.-W. Zhang, Z.-Y. Ye, C.-A. Zhang, and F. Liu, "Supersonic flutter analysis based on a local piston theory," *AIAA Journal*, vol. 47, no. 10, pp. 2321–2328, 2009.

[47] Q. Zhang, K. Ye, Z.-y. Ye, and W.-w. Zhang, "Aerodynamic optimization for hypersonic wing design based on local piston theory," *Journal of Aircraft*, vol. 53, no. 4, pp. 1065–1072, 2016.

[48] M. J. Lighthill, "Oscillating airfoils at high mach number," *Journal of the Aeronautical Sciences*, vol. 20, no. 6, pp. 402–406, 1953.

[49] E. H. Dowell and D. B. Bliss, "New look at unsteady supersonic potential flow aerodynamics and piston theory," *AIAA journal*, vol. 51, no. 9, pp. 2278–2281, 2013.

[50] W. Liu, C.-A. Zhang, H.-Q. Han, and F.-M. Wang, "Local piston theory with viscous correction and its application," *AIAA Journal*, vol. 55, no. 3, pp. 942–954, 2017.

[51] K. R. Brouwer and J. J. McNamara, "Enriched piston theory for expedient aeroelastic loads prediction in the presence of shock impingements," *AIAA Journal*, vol. 57, no. 3, pp. 1288–1302, 2019.

[52] A. P. Boresi and R. J. Schmidt, *Advanced mechanics of materials*. John Wiley & Sons, 2002.

[53] H.-J. Bungartz, F. Lindner, B. Gatzhammer, M. Mehl, K. Scheufele, A. Shukaev, and B. Uekermann, "precice–a fully parallel library for multi-physics surface coupling," *Computers & Fluids*, vol. 141, pp. 250–258, 2016.

[54] F. G. Blottner, "Accurate navier-stokes results for the hypersonic flow over a spherical nosetip," *Journal of spacecraft and Rockets*, vol. 27, no. 2, pp. 113–122, 1990.

[55] B. W. Boehm, "Software engineering economics," *Software pioneers: Contributions to software engineering*, pp. 641–686, 2002.

[56] P. J. Roache, "Quantification of uncertainty in computational fluid dynamics," *Annual review of fluid Mechanics*, vol. 29, no. 1, pp. 123–160, 1997.

[57] B. H. Thacker, S. W. Doebling, F. M. Hemez, M. C. Anderson, J. E. Pepin, and E. A. Rodriguez, "Concepts of model verification and validation," 2004.

[58] R. D. Blevins and R. Plunkett, "Formulas for natural frequency and mode shape," *Journal of Applied Mechanics*, vol. 47, no. 2, p. 461, 1980.

[59] L. Mangani, W. Sanz, and M. Darwish, "Comparing the performance and accuracy of a pressure-based and a density-based coupled solver," in *16th International Symposium on Transport Phenomena and Dynamics of Rotating Machinery*, 2016.

[60] E. Ter Hofstede, S. Kottapalli, and A. Shams, "Numerical prediction of flow induced vibrations in nuclear reactor applications," *Nuclear Engineering and Design*, vol. 319, pp. 81–90, 2017.

[61] Y. Fan and J. Xia, "Simulation of 3d parachute fluid–structure interaction based on nonlinear finite element method and preconditioning finite volume method," *chinese Journal of Aeronautics*, vol. 27, no. 6, pp. 1373–1383, 2014.

[62] M. Wright, Y. Luo, Q. Xiao, M. Post, W. Gorma, A. Durrant, and H. Yue, "Cfd-fsi analysis on motion control of bio-inspired underwater auv system utilizing pid control," in *2020 IEEE/OES Autonomous Underwater Vehicles Symposium (AUV)*. IEEE, 2020, pp. 1–6.

[63] Y. Wei and T. Tezdogan, "A fluid-structure interaction model on the hydroelastic analysis of a container ship using precice," in *International Conference on Offshore Mechanics and Arctic Engineering*, vol. 85925.   American Society of Mechanical Engineers, 2022, p. V007T08A035.

[64] A. Kurganov and E. Tadmor, "New high-resolution semi-discrete central schemes for hamilton–jacobi equations," *Journal of Computational Physics*, vol. 160, no. 2, pp. 720–742, 2000.

[65] V. Przulj and B. Basara, "Bounded convection schemes for unstructured grids," in *15th AIAA Computational Fluid Dynamics Conference*, 2001, p. 2593.

[66] H. K. Versteeg and W. Malalasekera, *An introduction to computational fluid dynamics: the finite volume method*.   Pearson education, 2007.

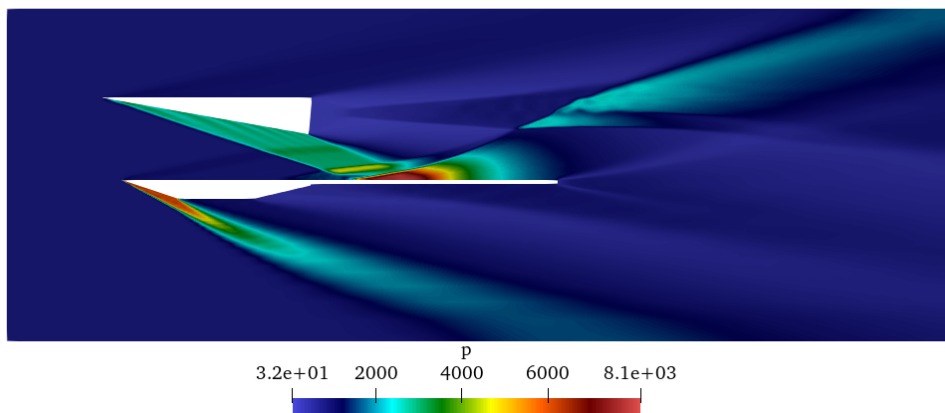# APPENDIX A: PRESSURE AND DENSITY CONTOURS
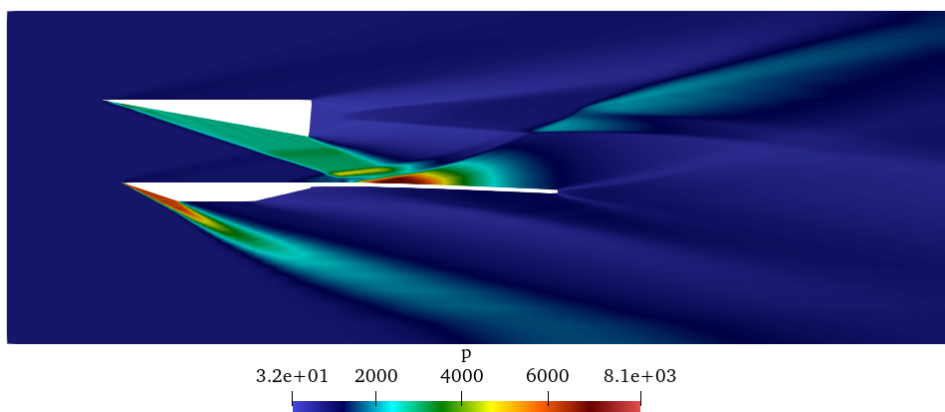


Figure A.1: Pressure Contour (t = 0)
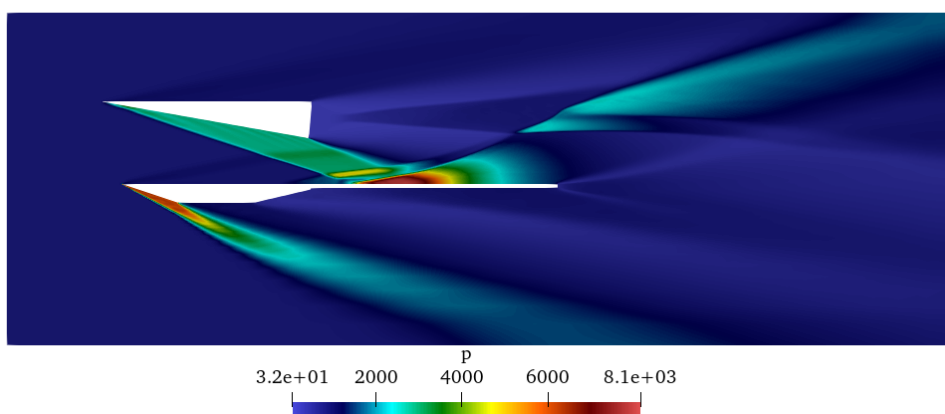


Figure A.2: Pressure Contour (t = T/2)

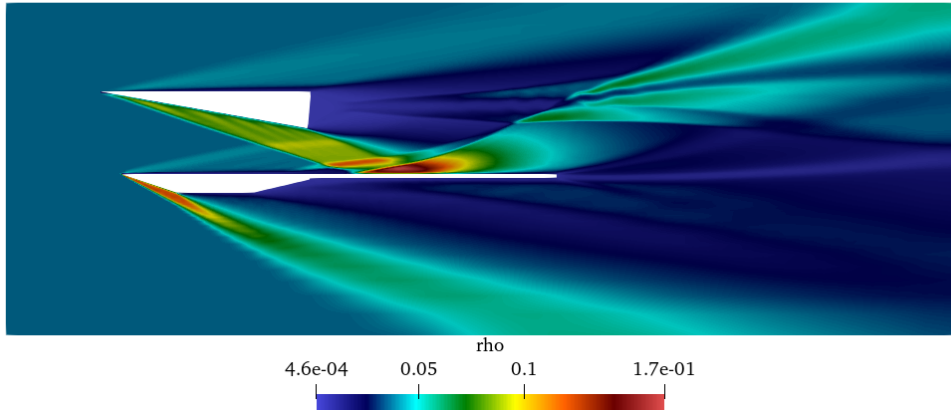

Figure A.3: Pressure Contour (t = T)
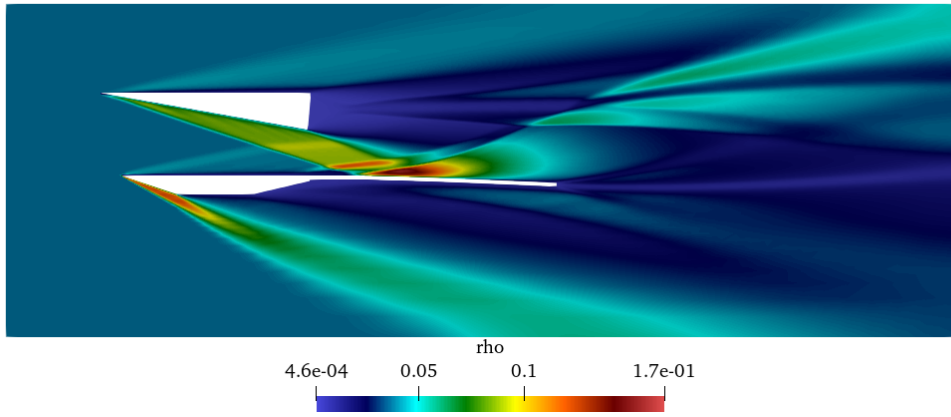
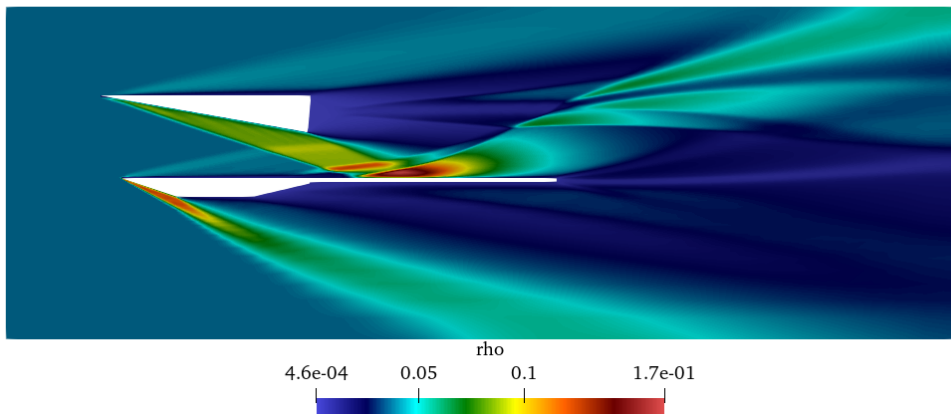Figure A.4: Density Contour (t = 0)



Figure A.5: Density Contour (t = T/2)



Figure A.6: Density Contour (t = T)